Precise Modification of 2D Materials by Gas Ion Beams

A thesis submitted in fulfilment of the requirements for the degree of Doctor of Philosophy in the

School of Physics

Trinity College Dublin

September 2017

Author
Pierce Maguire

Supervisor
Prof. Hongzhou Zhang

Declaration

I declare that this thesis has not been submitted as an exercise for a degree at this or any other university and it is entirely my own work.

I agree to deposit this thesis in the university's open access institutional repository or allow the library to do so on my behalf, subject to Irish copyright legislation and *Trinity College Library* conditions of use and acknowledgement.

Elements of this work that have been carried out jointly with others or by collaborators have been duly acknowledged.

I have read and I understand the plagiarism provisions in the G*eneral Regulations of the University Calendar* for the current year, found at: http://www.tcd.ie/calendar.

I have also completed the online tutorial on avoiding plagiarism *"Ready, Steady, Write"*, located at http://tcd-ie.libguides.com/plagiarism/ready-steady-write.

Pierce Maguire

Abstract

Precise Modification of 2D Materials by Gas Ion Beams

Pierce Maguire

Precise modification of the geometry, stoichiometry and crystal structure of two dimensional (2D) materials will be instrumental in future nanodevice fabrication. Here, ion beams focused to a sub-nanometre scale have been demonstrated to modify the electrical and optical properties of graphene and molybdenum disulphide (MoS_2). Nanopores with sub-5 nm diameters were fabricated in graphene using a nitrogen gas-etching process moderated by an electron beam. A diffusion-based model was developed to quantify and illuminate the process. Defect-engineering was performed in graphene with a high level of precision by irradiation with He^+ and Ne^+. Separately the defect-engineering process was expanded for monolayer MoS_2. Irradiation was also used to fabricate nanostructures with nanometre scale widths, to tune stoichiometry and to alter resistivity. Imaging using high resolution transmission electron microscopy demonstrated high quality He^+ ion fabricated nanoribbons of ~7 nm and amorphous nanoribbons of ~1 nm. Finally, the effect of defects and heating parameters on the oxidation of MoS_2 in air were explored, and the reaction was found to be substantially moderated through ion-induced defects.

Research Output

Publications

The following is a list of the author's scientific output at time of publication. Numbers 3, 10 and 15 and the papers in preparation (17 and 18) are highlighted as contributing a great deal to this thesis.

1. R. O'Connell, Yanhui Chen, **Hongzhou Zhang**, Yangbo Zhou, Daniel S. Fox, **Pierce Maguire**, Jing Jing Wang, Cornelia Rodenburg.
   "Comparative study of image contrast in scanning electron microscope and helium ion microscope," *Journal of Microscopy*, 268 (3), December 2017

2. Yanhui Chen, Fei Xue, Shengcheng Mao, Haibo Long, Bin Zhang, Qingsong Deng, Bin Chen, Yinong Liu, **Pierce Maguire**, **Hongzhou Zhang**, Xiaodong Han, and Qiang Feng.
   "Elemental preference and atomic scale site recognition in a Co-Al-W-base superalloy," *Scientific Reports*, 7 (1), December 2017

3. **Pierce Maguire**, Daniel S. Fox, Yangbo Zhou, Qianjin Wang, Maria O'Brien, Jakub Jadwiszczak, John McManus, Niall McEvoy, Georg S. Duesberg, **Hongzhou Zhang**.
   "Defect sizing, distance and substrate effects in ion-irradiated monolayer 2D materials," *arXiv.org*, 1707.08893, July 2017

4. Jakub Jadwiszczak, Colin O'Callaghan, Yangbo Zhou, Daniel S. Fox, Eamonn Weitz, Darragh Keane, Conor P. Cullen, Ian O'Reilly, Clive Downing, Aleksey Shmeliov, **Pierce Maguire**, John J. Gough, Cormac McGuinness, Mauro S.

Ferreira, A. Louise Bradley, John J. Boland, Georg S. Duesberg, Valeria Nicolosi, **Hongzhou Zhang**.
"Oxide-mediated recovery of field effect mobility in plasma-treated MoS_2," *Science Advances*, Accepted for publication, January 2018.
arXiv.org, 1706.08573, June 2017

5. Yanhui Chen, Junfeng Zhou, Felim Vajda, **Pierce Maguire**, Robert O'Connell, Wolfgang Schmitt, Yonghe Li, Zheng-Guang Yan, Yue-Fei Zhang, **Hongzhou Zhang**.
"Multi-metallic hydrate hollow structures in cobalt hydrate based systems," *Crystal Growth & Design*, 17 (4), March 2017

6. Wei Lu, Alan Kelly, **Pierce Maguire**, **Hongzhou Zhang**, Catherine Stanton, Song Miao.
"Correlation of emulsion structure with cellular uptake behaviour of encapsulated bioactive nutrients: influence of droplet size and interfacial structure," *Journal of Agricultural and Food Chemistry*, 64 (45), October 2016

7. Junfeng (Jim) Zhang, Ki-Bum Lee. Linchen He, Joanna Seiffert, Prasad Subramaniam, Letao Yang, Shu Chen, **Pierce Maguire**, Gediminas Mainelis, Stephan Schwander, Teresa Tetley, Alexandra Porter, Mary Ryan, Milo Shaffer, Sheng Hu, Jicheng Gong, Kian Fan Chung.
"Effects of a nanoceria fuel additive on the physicochemical properties of diesel exhaust particles," *Environmental Science Processes & Impacts*, 18 (10), September 2016

8. Yangbo Zhou, **Pierce Maguire**, Jakub Jadwiszczak, Manoharan Muruganathan, Hiroshi Mizuta, **Hongzhou Zhang**,
"Precise milling of nano-gap chains in graphene with a focused helium ion beam," *Nanotechnology*, 27 (32), June 2016

9. Junfu Ji, Kevin Cronin, John Fitzpatrick, **Pierce Maguire**, **Hongzhou Zhang**, Song Miao,
"The structural modification and rehydration behaviours of milk protein isolate

powders: The effect of granule growth in the high shear granulation process" *Journal of Food Engineering*, 189, May 2016

10. Daniel S. Fox, **Pierce Maguire**, Yangbo Zhou, Cornelia Rodenburg, Arlene O' Neill, Jonathan N. Coleman, **Hongzhou Zhang**,
"Sub-5 nm graphene nanopore fabrication by nitrogen ion etching induced by a low-energy electron beam" *Nanotechnology*, 27 (19), May 2016

11. Junfu Ji, John Fitzpatrick, Kevin Cronin, **Pierce Maguire**, **Hongzhou Zhang**, Song Miao,
"Rehydration behaviours of high protein dairy powders: The influence of agglomeration on wettability, dispersibility and solubility" *Food Hydrocolloids*, 58, March 2016

12. Yangbo Zhou, Daniel S. Fox, **Pierce Maguire**, Robert O'Connell, Robert Masters, Cornelia Rodenburg, Hanchun Wu, Maurizio Dapor, Ying Chen, **Hongzhou Zhang**,
"Quantitative secondary electron imaging for work function extraction at atomic level and layer identification of graphene," *Scientific Reports*, 6, February 2016

13. Yanhui Chen, Junfeng Zhou, **Pierce Maguire**, Robert O'Connell, Wolfgang Schmitt, Yonghe Li, Zhengguang Yan, Yuefei Zhang, **Hongzhou Zhang**,
"Enhancing capacitance behaviour of CoOOH nanostructures using transition metal dopants by ambient oxidation," *Scientific Reports*, 7, February 2016

14. Askar Syrlybekov, Han-Chun Wu, Ozhet Mauit, Ye-Cun Wu, **Pierce Maguire**, Abbas Khalid, Cormac Ó Coileáin, Leo Farrel, Chenglin Heng, Mohamed Abid, Huajun Liu, Li Yang, **Hongzhou Zhang**, Igor V. Shvets,
"Electrical-field-driven metal-insulator transition tuned with self-aligned atomic defects," *Nanoscale*, 7 (33), July 2015

15. Daniel S. Fox, Yangbo Zhou, **Pierce Maguire**, Arlene O'Neill, Cormac Ó Coileáin, Riley Gatensby, Alexey M. Glushenkov, Tao Tao, Georg S. Duesberg, Igor V. Shvets, Mohamed Abid, Mourad Abid, Han Chun Wu, Ying Chen,

Jonathan N. Coleman, John F. Donegan, **Hongzhou Zhang**, “Nanopatterning and electrical tuning of MoS_2 layers with a sub-nanometre helium ion beam," *Nano Letters*, 15 (8), July 2015

16. Yangbo Zhou, Robbie O’Connell, **Pierce Maguire**, **Hongzhou Zhang**, “High throughput secondary electron imaging of organic residues on a graphene surface," *Scientific Reports*, 7032 (4), November 2014

In Preparation

17. **Pierce Maguire**, Maria O’Brien, Niall McEvoy, Georg S. Duesberg, **Hongzhou Zhang**, “Defect density dependence of low frequency Raman spectroscopy modes in ion irradiated bilayer MoS_2," *In Preparation*, 2017

18. **Pierce Maguire**, Maria O’Brien, Jakub Jadwiszczak, Darragh Keane, Daniel S. Fox, Niall McEvoy, John Boland, Georg S. Duesberg, **Hongzhou Zhang**, “Ion moderated oxidative etching of MoS_2," *In Preparation*, 2017

Presentations

- “Ne^+, He^+ and Ga^+ Irradiation for Nanometre Tuning of 2D Materials,” Presented at MMC 2015, Manchester, UK and MSI 2015, University of Limerick.
- “Evolution of the Raman spectra of graphene and MoS_2 with scanning He^+ and Ne^+ irradiation.” Presented at MSI Comerford Memorial poster session, 2017, NUIG.

Acknowledgements

First and foremost, my sincere thanks to past and present members of the *Photonics and Nanofabrication Group* for their training, expertise and very significant contribution to my training and research. I am grateful to my mentor Dr. Daniel S. Fox for his assistance and guidance. Special thanks are also due to Prof. Yangbo Zhou, Prof. Yanhui Chen, Abbas Khalid, Dr. Robert O'Connell, Junfeng Zhou, Darragh Keane, Fei Gao, Jakub Jadwiszczak, Gen Li and other students who joined us briefly. Above all, sincere thanks to my supervisor, Prof. Hongzhou Zhang for his patience and support.

I wish to thank the staff and students of the *School of Physics*, particularly Dr. Niamh McGoldrick, Prof. Cormac McGuinness and the *Photonics Group*. Many of the staff of *CRANN/AMBER* have provided essential assistance, especially at the *Advanced Microscopy Laboratory*: Dermot Daly; Clive Downing; Dr. Alan Bell; Cathal McAuley; Keith Boland; Dr. Allen Bellew, Dr. Eoin McCarthy and Dr. Clodagh Dooley. Several collaborators deserve special mention for their enormous help and support including members of the *ASIN* group in the *School of Chemistry* including Dr. Maria O'Brien and Dr. Niall McEvoy, and Qianjin Wang at the *Collaborative Innovation Center of Advanced Microstructures* at *Nanjing University.* Of my friends, colleagues and extended family I thank Mary Matthews and members of Prof. Nicolosi's group with particular mentions to Dr. Anuj Pokle, Megan Canavan and Dr. Edmund Long.

In my personal and family life I am also very grateful to the following people: Aideen Fennell, my parents, my grandmother and my brother, without whom making it this far would not have even been remotely possible.

Contents

Declaration iii

Abstract v

Research Output vii

Acknowledgements xi

Contents xii

List of Figures xvii

List of Tables xxi

Glossary xxiii

1 Introduction **1**
1.1 Outline of the Thesis 4

2 Materials **7**
2.1 Graphene 7
2.2 Molybdenum Disulphide 15

3 Modification Methodology **23**
3.1 Nanomaterial Engineering 23
3.2 Ion Beams 25
3.3 Ion Beam Sample Interaction 27

3.4 Simulating Ion Interactions 28
3.5 Dose and Substrate Effects 29
3.6 Displacement Threshold in MoS_2 31
3.7 Ion Beams and 2D Materials 32
3.8 Electron Beams and Defects 33
3.9 Oxidation of FLM-MoS_2 in the Literature 33

4 Analysis Methodology 43
4.1 Raman Spectroscopy 43
4.2 Low Frequency Raman Spectroscopy of MoS_2 48
4.3 Photoluminescence Spectroscopy 49
4.4 Microscopy and Resolution 50
4.5 Scanning Electron Microscope 50
4.6 Transmission and Scanning Transmission Electron Microscopy 53
4.7 Energy Dispersive X-ray Spectroscopy 55

5 Modifying Graphene by Charged Particle Beams 57
5.1 Electron Beam-Induced Nitrogen Etching 58
5.1.1 Summary 67
5.2 Defect-Engineering by He^{+} and Ne^{+} Irradiation 68
5.2.1 Summary 80

6 Irradiation and Patterning of MoS_2 81
6.1 Structural Modification and Defect-Engineering 82
6.2 Stoichiometry Tuning 90
6.3 Nanostructure Fabrication 92
6.4 Electrical Characterisation 95
6.5 Summary 100

7 Ion Moderated Oxidation of MoS_2 101
7.1 Ion Dose Dependency 101
7.2 Expanding the Oxidation Model 104
7.3 Defining Temperature Stages in the MoS_2 Oxidation Model 111

7.4 Etching Range and Edge Definition 115
7.5 Summary 116

8 Conclusion 119
8.1 Future Work 120

Appendices 121

A Identifying Suitable Samples in TMSEM 123

B Supplementary Information for Etching of Graphene by Nitrogen 125

C Ion Beam Stability and Dose Uncertainty 131

D Fitting the *LA(M)* Mode in Raman 133

E Probe Size Measurement in the GIM 135

F Oxidative Etching Attempts with Mechanically Exfoliated MoS_2 137

G Producing Meshes with Oxidation 139

References 141

List of Figures

2.1 Graphene lattice and $2D$ band generation from transition sliding. . . 8
2.2 The calculated phonon dispersion relation of graphene 10
2.3 Double and triple resonance in Raman spectra of graphene 11
2.4 D band generation from regions adjacent to defect sites 14
2.5 Evolution of the $2D$ peak as a function of number of layers 16
2.6 The Brillouin zone and band structure of MoS_2 18
2.7 The crystal structure of monolayer MoS_2 18
2.8 Vibrational modes and Raman spectroscopy for the differentiation of the number of MoS_2 layers 20

3.1 The gas field ion source in the gas ion microscope 26
3.2 A Stopping and Range of Ions in Matter software simulation of ion trajectories. 29
3.3 Displacement cross sections of atoms in MoS_2 with 30 keV He^+ 31
3.4 Thermal thinning and etching of 2L MoS_2 nanosheets 37
3.5 Modelling the etching of triangular pits in MoS_2 39

4.1 Jablonski diagram illustrating Stokes and anti-Stokes shifts 44
4.2 Data treatment in Raman spectroscopy 47
4.3 Low frequency Raman spectrum and peak intensity map of the layer breathing mode of 2L MoS_2 49
4.4 Outline of a scanning electron microscope 51
4.5 Outline of a transmission electron microscope and a scanning transmission electron microscope. 54

5.1 SEM images of electron-irradiated graphene with and without nitrogen gas . . . 59
5.2 TEM images of electron beam-assisted nitrogen etched graphene . . . 61
5.3 Etching and deposition rates as a function of beam current. 62
5.4 The area of graphene etched as a function of electron beam dwell time. 65
5.5 Nitrogen etching rate as a function of beam current 66
5.6 MoS_2 flake after an etching attempt with nitrogen gas. 67
5.7 Representative selection of irradiated CVD graphene Raman spectra . 69
5.8 Evolution of the full width at half maximum of the G peak and intensity ratio in graphene . . . 70
5.9 The $2D$ peak in graphene Raman spectra . . . 71
5.10 The evolution of the I_D/I_G ratio of freestanding and supported graphene with L_D . . . 72
5.11 Graph of defect size against the maximum of the I_D/I_G peak 75

6.1 Modification of few layer mechanically exfoliated MoS_2 crystal structure with He^+ imaged in TEM . . . 82
6.2 Low frequency Raman modes in bilayer MoS_2 . . . 84
6.3 Ion dose dependent photoluminescence spectroscopy of bilayer MoS_2 . 87
6.4 Representative selection of Raman spectra of irradiated monolayer MoS_2 88
6.5 Evolution of the FWHM and peak position with $L_{D(Mig)}$ for monolayer MoS_2 . . . 88
6.6 Evolution of the Ratios of the intensity of the $LA(M)$ peak to the intensity of the E' and A'_1 modes for both He^+ and Ne^+ irradiated monolayer MoS_2. . . . 89
6.7 Stoichiometry alteration of a few layer MoS_2 flake by He^+ irradiation. 91
6.8 HRTEM images of the edges of three regions in the same freestanding MoS_2 flake milled with three different probe sizes. . . . 92
6.9 Graph of simulated ion distribution at nanostructure edges with ratio of FFTs . . . 94
6.10 TEM images of He^+ fabricated few layer freestanding nanoribbons in MoS_2 . . . 95

6.11 Simulation of the distribution of ion dose produced by a Gaussian array. 96
6.12 Electrical characterization of He^+ modified devices. 97
6.13 Electrical characterization of He^+ manufactured 20 nm nanoribbon. . 99

7.1 Outline of a typical oxidative etching experiment 102
7.2 Ion dose dependency of oxidative etching in bilayer MoS_2 104
7.3 Scanning electron microscopy analysis of etching bilayer MoS_2 in a cumulative heating experiment. 105
7.4 Searching for MoO_x in heated CVD MoS_2 using Raman spectroscopy 107
7.5 Expanding the etching model for monolayer CVD MoS_2 with Raman spectroscopy. 109
7.6 Heat maps of SEM brightness and A_1' peak position and width for bilayer MoS_2 112
7.7 Edge roughness and etching range 114

A.1 Identifying suitable MoS_2 flakes for experiments in TMSEM. 124

B.1 Mono and ten layer graphene etch 126
B.2 Optical image of single and ten layer MoS_2 on a 300 nm SiO_2 layer on Si. 126
B.3 Temperature effect of e-beam etching. 128
B.4 Measuring nanopore sizes from TEM images with Imagej 129

D.1 Raman spectra with fitting of the $LA(M)$ mode 134

E.1 Measuring probe size from a GIM image 136

F.1 Attempted etching of mechanically exfoliated MoS_2 138

G.1 Meshes of CVD-grown MoS_2 produced by oxidation 140

List of Tables

3.1 Key figures from the literature concerning the oxidation of MoS_2 . . . 40

5.1 Sputtering yields and defect per incident ion values of carbon atoms in graphene . . . 73
5.2 Initial fitting parameters for use with the modified version of the model developed by Lucchese et al. . . . 74
5.3 Key figures calculated from fitting the model developed by Lucchese et al. . . . 74
5.4 Comparison of three ion species at 30 keV. . . . 78

7.1 Temperature dependent oxidation stages . . . 111

Glossary

A number of abbreviations, important terms and chemical formulae are listed. Please note that for the purposes of the glossary, the words microscope and microscopy can be considered interchangeable and dependent on context.

2D two dimensional ii, 1–4, 6, 14, 20–22, 28, 40, 47, 49, 50, 53, 76, 77, 97, 113–115

AC armchair-terminated edge 36

AFM atomic force microscopy 33, 34, 54, 78

Amorphous Carbon carbon without crystal structure 43

BID beam-induced deposition 43

BIV best imaging voltage 24

BSE backscattered electrons 48, 49

CLS cathodoluminescence spectroscopy 48, 52

CVD chemical vapour deposition 8, 16, 22, 64, 69, 79, 82, 97, 98, 100, 110, 129

Defect-Engineering controlled alteration of the defect density or type of defects in a material ii, 2–5, 14, 22, 25, 30, 32, 77, 97, 114, 115

DFT density functional theory 2, 17, 18, 22, 27, 33, 34, 36

Displacement Threshold minimum kinetic energy that an atom in a solid needs to be permanently displaced from its lattice site 29

Double-Resonance a fourth-order perturbative Raman model used in carbon materials 10, 11

EBL electron beam lithography 92

EDX energy dispersive x-ray spectroscopy 4, 40, 48, 52, 79, 86, 94

EELS electron energy loss spectroscopy 52

EFTEM energy-filtered transmission electron microscopy 122

ET Everhart-Thornley 49, 50

$FeSi_2$ iron disilicide 94

FET field effect transistor 32

FFT fast Fourier transform 50, 51, 57, 89

FIB focused ion beam 3, 23, 25, 121

FLG few layer graphene 56, 58

FLM few layer or monolayer 32, 33, 112

Fullerene hollow molecules of carbon 42

FWHM full width at half maximum 43, 66, 67, 89

GFIS gas field ion source 3, 24, 25

GIM gas ion microscope 24, 25, 47–49, 51, 97, 100, 114, 117

Graphene 2D honeycomb lattice of sp2 carbon atoms ii, 2, 4, 6, 8, 9, 11–14, 16, 18, 23, 29, 30, 32, 40, 42, 43, 53, 54, 56, 58, 62, 64, 67, 69, 71, 73, 74, 76, 77

HAADF high angle annular dark field 6, 51, 86

HOPG highly oriented pyrolitic graphite 8

ImageJ image processing program with many available plugins 56, 127

Inter-defect distance average distance between defects 4, 13, 54, 76–78, 85

IR infrared 18

ITO indium tin oxide 8

KHD Kramers-Heisenberg-Dirac 11

LBM layer breathing mode 42, 45, 79, 81

LMIS liquid metal ion source 23

Matlab a programming language and computing environment developed by *Mathworks* 73, 131

MFM magnetic force microscopy 33, 34

MgO magnesium oxide 26

Molecular Dynamics computer simulation method for atom/ion interactions 21, 27

MoO_2 molybdenum dioxide 102–104

MoO_3 molybdenum trioxide 32–34, 38, 79, 102–104, 109, 111

MoO_x molybdenum oxide 38, 39, 97

MoS_2 molybdenum disulphide ii, xii, xiii, 1–6, 14, 16, 18, 19, 21–23, 26, 28–36, 38–40, 42, 43, 45, 47, 52–54, 62, 63, 77–79, 81, 82, 84–86, 88, 89, 91, 92, 94–100, 102–115, 119, 129, 131

$MoSe_2$ molybdenum diselenide 45

$MoTe_2$ molybdenum telluride 94

Nanoribbon strips of material of thickness <100 nm 23, 27, 77, 95

NMP N-methyl-pyrrolidone 54

O_2 molecular oxygen 32, 34

OM optical microscopy 34, 47, 48, 79, 97, 99, 129

PL photoluminescence spectroscopy 16, 34, 40, 47, 81

RPM rotations per minute 54

RT room temperature 99, 104, 106, 107, 109

SCCM standard cubic centimetres per minute (unit of flow rate) 79

SE secondary electron 48–50

- **SE_1** type 1 48–50
- **SE_2** type 2 49
- **SE_3** type 3 49

SEM scanning electron microscopy 4, 21, 25, 31, 40, 47–51, 56, 92, 97, 98, 100–103,

107–111, 113, 117, 119, 121, 122, 131

SES secondary electron spectroscopy 48

SFIM scanning field ion microscopy 24

SiO_2 silicon dioxide 34, 54, 91, 119, 129

SM shear mode 42, 45, 79, 81

SO_2 sulphur dioxide 32

SRIM Stopping and Range of Ions in Matter software 21, 26–28, 69, 71, 73

STEM scanning transmission electron microscope 6, 50, 51, 79, 86, 117

TEM transmission electron microscope ii, 3, 4, 23, 40, 50, 51, 54, 56–58, 78, 79, 88, 89, 117, 121, 122, 127

TMD transition metal dichalcogenide 1, 14, 18, 32, 45, 115

TMSEM transmission mode scanning electron microscopy 50, 56, 86, 117

TR triple resonance 10

TTL through the lens 48–50, 100

WS_2 tungsten disulphide 30, 47

WSe_2 tungsten diselenide 45

XeF_2 xenon difluouride 62

XPS X-ray photoelectron spectroscopy 34

ZZ zig-zag terminated edge 36

- **ZZ-Mo** Mo terminated zig-zag edge 36, 38
- **ZZ-S_2** S_2 terminated zig-zag edge 36, 38

Chapter 1

Introduction

Two dimensional materials were brought to global attention by Geim and Novoselov in 2004, who would later share the 2010 Nobel Prize in Physics for their work on graphene [1]. The structure of graphene was first discussed by Wallace as early as 1947 and its name was coined by Boehm et al. in 1994 [2–4]. Geim and Novoselov succeeded in isolating, visualising and characterising this material of single atom thickness from graphite.

The extraordinary properties of graphene are now well-documented and are in large part responsible for stimulating the discovery of a wide variety of 2D materials and related research methodologies under investigation today [5, 6]. The extraordinary properties and tunability of 2D materials have been repeatedly demonstrated, heralding a new era of materials science [1, 6]. The physical properties of 2D materials are highly distinguished with respect to their bulk counterparts due to the evolution of their band structure with layer number [5–9]. MoS_2 for instance, is a quintessential transition metal dichalcogenide (TMD) which has an indirect band gap in the multi-layer system and a direct band gap in the monolayer. This allows a vast enhancement in radiative recombination, essential for the use of a material in optoelectonic devices such as thin film photodetectors [10–12]. Proposed applications of 2D materials are in fields as diverse as photonics, electronics and composites [13, 14].

The challenges faced in technological progress are myriad, and 2D materials will be critical to disrupting many existing technologies. For instance, continuity of

Moore's law will shortly require the downsizing of transistors in computational devices to a scale of single digit nanometres. Bulk silicon, the incumbent material in this field for many decades, is expected to be unable to reach the smallest possible size range and still maintain performance due to severe short channel effects [15]. If Moore's law is to continue, it appears at this juncture that enabling technologies may have to incorporate the extraordinary family of 2D materials. However, given their diminutive scale a host of novel fabrication methodologies must be employed for these materials to become functional devices. Fabrication technologies must produce future-devices while also achieving acceptable throughput and cost-effectiveness. Nanometre-scale tuning of behaviour must also be accompanied by minimal structural damage. Other challenges regarding the material properties include opening and controlling band gaps (for example in zero band gap graphene) and controlling doping states (for example achieving p-type doping of MoS_2) while maintaining high mobility [6, 16].

The alteration of nanoscale geometry and the introduction of structural defects or strain to these materials are already well established for the purposes of modulating their electronic and optical properties [17–21]. Density functional theory (DFT) studies have shown that MoS_2 nanoribbons with widths of ~3 nm (within the quantum confinement regime) have extraordinary physical properties. For example, MoS_2 nano-ribbons terminated with an armchair edge are non-magnetic direct band gap semiconductors while those terminated with a zigzag edge are half-metallic [17, 22].

Both DFT simulations which incorporate defects and strain and experiments involving defect-engineering have demonstrated that defects profoundly alter the electrical and optical properties (such as conductivity) of 2D materials [18–21]. Ion irradiation has an illustrious record over many decades in the scalable, precise defect-engineering of materials [23]. Ions have been used historically to control doping by implantation and to introduce precise quantities of defects, albeit with little spatial control without expensive masking [24]. More recently, a variety of ion energies and species have been used in the doping and defect-engineering of 2D materials [25–29]. Low energy phosphorus implantation was used to create p-type devices made with few-layer (5-10 layers) MoS_2 [25]. Many studies have used Raman spectroscopy to correlate a range of ion species, doses and energies to the defect engineering of 2D

materials [26–29].

The demands of modern semiconductor technology are such that precise nanoscale control of 2D material properties is much sought after. However, scalable nanofabrication methods to produce such structures remain elusive. To date, many chemical and physical methods have been used to produce MoS_2 nanostructures with a desired geometry. These approaches have produced nanoribbons that were either polycrystalline or too wide (>10 nm) [30, 31]. Direct fabrication of MoS_2 nanoribbons down to 0.44 nm has been reported in a transmission electron microscope (TEM) [32] although the composition and phase of these structures is the subject of continued discussion [33]. This is also an impractical fabrication approach due to its requirement of a freestanding sample, its low rate of milling, lack of scalability, and its expense. A Ga^+ focused ion beam (FIB) can sputter surface atoms and introduce nanoscale modification effectively with its ~5 nm probe [34]. However, a non-metallic ion species and a sub-nanometre probe size are required for the high resolution machining of semiconducting devices.

Recently, ion microscopes using a gas field ion source (GFIS) have made these goals eminently achievable due to their sub-nanometre resolution and relatively high throughput [35–40]. Given the superlative confinement of 2D materials in their out-of-plane direction, it is possible to restrict the ion-induced interaction in this direction to their exceptionally small thickness. Ion irradiation can be used to perform a wide range of alterations beyond introducing defects and sputtering. He^+ irradiation of graphene encapsulated in hexagonal boron nitride has been used to introduce n-type doping [41]. Such methods have been used to create nanoribbons with widths of less than 10 nm [37]. However before my thesis there has been little effort to evaluate the quality of the crystal structure of the remaining material [35].

Compromises and challenges remain in balancing resolution, precision, sample contamination and throughput. Amorphisation of material around the desired irradiated region is one such issue due to the non-zero probe size of the beam. Ion beam-induced deposition is another problem, particularly in specimens which are not perfectly clean. Given the pivotal importance of defect-engineering and nanofabrication methods in the materials science of today, it is imperative that the effects of these ion beam fabrication methods on 2D materials be well understood.

This thesis will investigate the properties of the 2D materials graphene and MoS_2 as modified by the incidence of gas ion beams, utilising both broad and highly focused beams. Irradiation methods will be related to both defect number (or inter-defect distance) and size as well as position i.e. the spread of introduced defects from the point of incidence. This must be achieved while minimising undesirable secondary effects such as beam-induced deposition and unintentional amorphisation. Furthermore, the developed strategies will be used to manufacture extremely small nanostructures (with dimensions less than 10 nm) and alter the physical and chemical propertie quantifiably. This will facilitate applications of such methods and materials in optoelectronic devices.

1.1 Outline of the Thesis

Chapter 1 features the introduction to the thesis and this outline. Chapter 2 serves as a more general discussion of the 2D materials graphene and MoS_2 and their properties with a particular focus on their Raman spectra. Chapter 3 introduces the key modification methods used in this work, namely: nitrogen etching of graphene moderated by electron beam; He^+ and Ne^+ irradiation; and the chemical reaction of MoS_2 in air. Chapter 4 features the key methods by which changes in the properties of these materials are quantified, such as Raman spectroscopy, energy dispersive x-ray spectroscopy (EDX) and microscopy methods, such as TEM and scanning electron microscopy (SEM).

Chapter 5 is the first of the experimental chapters, which report the experiments and findings of this thesis. Chapter 5 is based entirely on two published articles: the complete paper reference [42] and part of the paper reference [43]. The chapter features graphene and is comprised of two distinct sections. The first section involves the nanometre scale etching of pits in graphene through nitrogen-assisted electron beam irradiation. A diffusion-based model was constructed to explain the growth of the nanopores and parameters were optimised for creating small, reproducible nanopores. The second features the defect-engineering of graphene by irradiation with energetic beams of He^+ and Ne^+ and quantification using Raman spectroscopy. With the basics of ion irradiation now established in a simple and well-studied ma-

terial system, it was then decided to expand the study to MoS_2.

Chapter 6 is an exploration of a range of irradiation methods and their effects on MoS_2 with a range of layer numbers. These changes include geometric, structural, stoichiometric and electrical alterations. Precise defect-engineering of monolayer MoS_2 using established models is presented, and the fabrication of nanoribbons on a nanometre scale is reported. Chapter 6 features the remainder of the paper reference [43] which details the defect-engineering of MoS_2 again using He^+ and Ne^+ and quantified using Raman spectroscopy. This chapter also includes essentially the entirety of the paper reference [37] showing the changing stoichiometry, Raman spectra and electrical properties of MoS_2 caused by He^+ irradiation. From that paper, the manufacturing of MoS_2 nanoribbons is also detailed. Presently unpublished work is also included on the low frequency Raman modes of bilayer MoS_2. This section is in preparation for publication as the paper listed as number 17 in the *Research Output* section [37, 43].

Chapter 7 shows how ion irradiation can be used to moderate the chemical behaviour of MoS_2. Existing knowledge of oxidation behaviour in air has been expanded and proposals for devices are made. Chapter 7 contains only work awaiting publication with the addition of further data including electrical measurements. That work is listed under the paper numbered 18 in the research output section.

Chapter 8 will provide a brief summary of the findings of this work and an outlook for future developments.

Chapter 2

Materials

In this chapter the two materials upon which this thesis is focused are discussed. Both graphene and MoS_2 are 2D materials which exhibit unusual and extraordinary properties due to their nanosized proportions. Quantum confinement leads to substantial differences in electronic band structure compared to bulk counterparts and the high surface-to-volume ratio of such materials causes further departure in behaviour. There is a particular focus in this chapter on the Raman spectra of these two materials as Raman spectroscopy will be used extensively in this thesis.

2.1 Graphene

Graphene consists of a single layer of sp^2 hybridised carbon atoms in a honeycomb lattice [1, 5]. A high resolution high angle annular dark field (HAADF) scanning transmission electron microscope (STEM) image of the hexagonal structure is shown in figure 2.1(a) [44]. Graphene exhibits supremacy in mechanical properties (Young's modulus of 1 TPa, intrinsic strength of 130 GPa), charge-carrier mobility (2.5 cm^2 V^{-1} s^{-1}), sustainable electric current density (a million times higher than copper) and thermal conductivity (above 3,000 WmK) [1, 6, 46–49].

Graphene's properties imbue it with the potential to displace or enhance existing materials in many fields. Some of the most promising applications of graphene include: as electrodes in supercapacitors for energy storage due to its surface area and mobility [50]; flexible electronics for display technology due to its optical transmit-

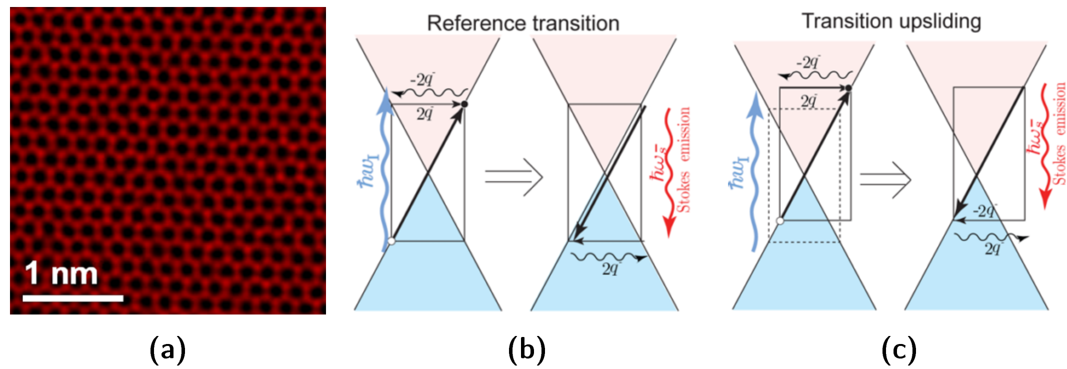

Figure 2.1: Graphene lattice and $2D$ band generation from transition sliding. (a) is a high resolution HAADF STEM image from Pan et al. [44]. (b) shows a reference transition (constructed symmetrically about the Dirac point) where absorption is followed by emission along the reverse path producing a net total of two phonons of opposite momentum. (c) shows a sliding transition (moved up in this case) which still fits absorption and emission transitions along the Dirac cone. The reference transition is shown as a dashed rectangle. Sliding the rectangle up or down leaves the phonon $2q^{-}$ unchanged and provides a continuum of transitions along the Dirac cone. This leads to the large intensity of the $2D$ band[45].

tance and low sheet resistance (displacing the rare and expensive indium tin oxide (ITO)) [6, 51, 52]; as an interconnect in integrated circuits due to its excellent electrical and thermal conductivity; and as a barrier for DNA sequencing and water desalination when perforated with appropriately sized nanopores [53, 54]. The expectation that graphene-based materials may give rise to new, as yet unknown applications, is also extensive [6]. However, this diverse range of applications will require a range of synthesis and treatment techniques, which negotiate the compromises of quality and cost efficiency. Novoselov et al. divided these proposed applications by the quality and other suitability factors of the required graphene material: (1) graphene or reduced graphene oxide flakes for composite materials, conductive paints, and so on; (2) planar graphene for lower-performance active and non-active devices; and (3) planar graphene for high-performance electronic devices [6].

Mechanical exfoliation, which uses for instance the scotch-tape method, produces graphene of exceedingly high crystal quality from highly oriented pyrolitic graphite (HOPG). However, it is not suitable for applications besides research due to scalability issues including poor control of the layer number. Liquid phase exfoliation uses a solvent and sonication to separate layers from suitable bulk materials. The graphene produced satisfies the requirements of the above-defined type 1 graphene applications only as it lacks precise layer control and solvents can only be removed at great difficulty and cost, although offering huge scalability [55, 56]. Chemical vapour deposition (CVD) growth of graphene is highly scalable [57–59] and provides graphene which satisfies the requirements for type 2 graphene applications (there is a greater number of defects in CVD produced material) [60]. Growth on SiC is the method which appears most applicable to type 3 graphene applications due to its relative scalability (compared to mechanical exfoliation at least though still limited to the size of the substrate) and crystal quality. However it remains distant from integration with existing technology because of several features including the high temperature required for growth, imprecise layer control, particularly at substrate terraces, and more [6, 61].

There are other considerations besides the quality/cost balance, for example, since copper interconnects are already standard in many semiconductor devices and graphene can be grown on copper easily by CVD it might be quite practical to

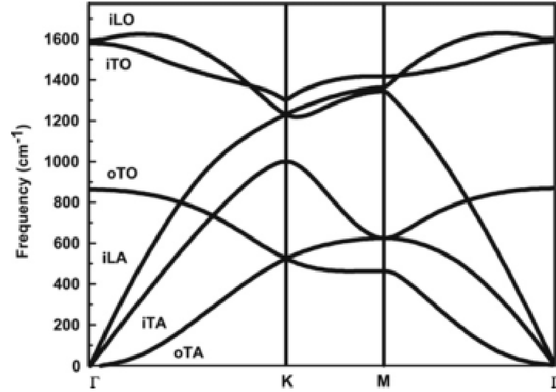

Figure 2.2: The calculated phonon dispersion relation of graphene [62, 63]. The iLO, iTO, oTO, iLA, iTA and oTA phonon branches are shown.

integrate graphene in this way, enhancing devices using relatively small changes to existing fabrication methods. However, synthesis is only a part of what is possible with huge scope left for post-synthesis modification methods as will be discussed in chapter 3 and is the main subject of this thesis.

The Raman spectra of carbon materials, including amorphous carbon, graphite, nanotubes and graphene, have been studied extensively allowing a wealth of information to be inferred including crystalite size, defect density, doping states, layer number and orientation [63–68]. The unit cell of monolayer graphene contains two carbon atoms and thus six phonon dispersion bands assigned to LO, iTO, oTO, LA, iTA, and oTA phonon modes as shown in figure 2.2. According to predictions using group theory, the LO and iTO phonon modes belong to the two-dimensional E_{2g} representation and are therefore Raman active modes [69, 70].

Experiments find the following prominent characteristic peaks in high quality monolayer graphene spectra using laser excitation at 514 nm: $2D$ at ~2700 cm^{-1} and G at ~1583 cm^{-1} [63, 64]. The G band is associated with the doubly degenerate (iTO and LO) phonon mode (E_{2g} symmetry) at the Brillouin zone center. In fact, the G band is the only band coming from a normal first order Raman scattering process in graphene (see figure 2.3). In the Raman spectra of defective graphene (particularly as the average distance between defects, L_D, decreases) or at an edge, the disruption

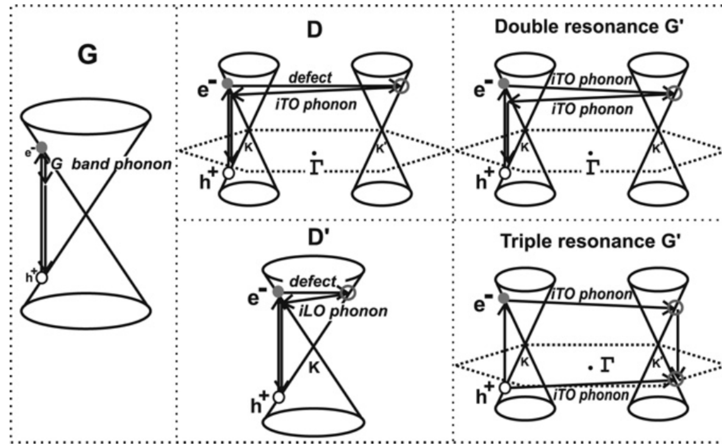

Figure 2.3: Double and triple resonance in Raman spectra of graphene. (Left) first-order G band process and (center) one-phonon second-order double-resonance process for the D band (intervalley process) (top) and for the D' band (intravalley process) (bottom). (Right) two-phonon second-order resonance Raman spectral processes (top) for the double-resonance G' process, and (bottom) for the triple resonance G' band process triple resonance (TR) for monolayer graphene [68]. For one-phonon, second-order transitions, one of the two scattering events is an elastic scattering event. Resonance points are shown as open circles near the K point (left) and the K′ point (right) [63].

to normal Raman selection rules also allows the detection of two further peaks: D at ~1350 cm^{-1}, and D' (sometimes referred to as G^S [45, 63]) at ~1600 cm^{-1}. The 2D and D bands originate from a second-order process, involving two iTO phonons near the K point for the 2D band or one iTO phonon and one defect in the case of the D band. The origin and the dispersive behaviour in the frequency of the D and 2D bands are explained using a double-resonance model (a fourth-order perturbative Raman model used in carbon materials). In this double-resonance process, the wave-vectors (q) of the phonons associated with the D and 2D bands (measured from the K point) would couple preferentially to the electronic states with wave-vectors (k) (measured from the K point), such that $q \approx 2k$ [63].

The double-resonance process shown in the center and right side of figure 2.3

begins with an electron of wave-vector **k** around K absorbing a photon of energy E_{laser}. The electron is inelastically scattered by a phonon or a defect of wave-vector **q** and energy E_{phonon} to a point belonging to a circle around the K′ point, with wave-vector **k**+**q**, where the K′ point is related to K by time reversal symmetry. The electron is then scattered back to a **k** state, and emits a photon by recombining with a hole at a **k** state. In the case of the D band, the two scattering processes consist of one elastic scattering event by defects of the crystal and one inelastic scattering event by emitting or absorbing a phonon [63].

In the case of the G' band, both processes are inelastic scattering events and two phonons are involved. This double-resonance mechanism is called an inter-valley process because it connects points in circles around inequivalent K and K′ points in the first Brillouin zone of graphene. On the other hand, the double-resonance process responsible for the D' band is an intra-valley process, since it connects two points belonging to the same circle around the K point (or the K′ point) [63].

The underlying explanation for the Raman spectrum of monolayer graphene is still a subject of debate as it has also been explained using Kramers-Heisenberg-Dirac (KHD) theory which can be derived using a first order perturbation theory approach. It describes the scattering of a photon by an electron. The KHD theory and its recent application in the case of graphene has led to the proposal of an effect labelled "transition sliding" which can occur in materials such as graphene whose electron transport properties are decribed by a Dirac cone. Transition sliding may be the process behind the very high brightness of the $2D$ overtone [45]. It is not clear if the KHD approach is applicable beyond a monolayer of graphene. This is illustrated in figures 2.1(b) and 2.1(c).

In graphene, the defect yield and the nature of defects introduced by these ion species are inferred from Raman spectra using established models [26, 27, 71, 72]. L_D in graphene has been related to the ratio of the intensity of the D peak (I_D) to the intensity of the G peak (I_G) by Lucchese et al. [26] and a version is given here by:

$$\frac{I_D}{I_G} = C_A \frac{(L_S^2 + 2r_S L_S)}{(L_S^2 + 2r_S L_S - r_S^2)} \left[e^{-\pi r_S^2/L_D^2} - e^{-\pi(L_S^2 + 2r_S L_S)/L_D^2} \right] + C_S \left[1 - e^{-\pi r_S^2/L_D^2} \right] \qquad (2.1)$$

This is the phenomenological local activation model of the Raman spectra of defective graphene. The model uses two length scales denoted by r_S and r_A which

represent the average radii of two circular areas centred at the ion impact points. The inner and structurally disordered area caused by an ion (labelled S) is described by the radius r_S. Outside of r_S the lattice structure is preserved but is activated with respect to the Raman D band (within the area labelled A). The distance from the centre of the impact site to the edge of the area A is labelled r_A. In other terms, a photoexcited electron-hole pair will be affected by the structural defect if the excitation process takes place in a region sufficiently close to the defect site i.e. a photoexcited electron–hole pair must reach the defective site during the time interval in which the Raman process occurs. Therefore, the difference, r_A - r_S should be related to the correlation length of photo-excited electrons participating in the double-resonance mechanism giving rise to the D band. $L_S = r_A - r_S$ is the Raman relaxation length for the resonant Raman scattering. These distances are illustrated clearly in figure 2.4(a).

Lucchese et al. used stochastic simulations to implement the model by simulating the structural evolution of a graphene sheet under ion bombardment. They randomly choose a sequence of impact positions and defined the following set of rules for each event: (1) pristine regions may turn into S or A regions, depending on the proximity to the impact point; (2) Similarly, A-regions may turn into S; (3) S-regions always remain S. Then, the initially pristine sheet evolves, as the number of impacts increase, to be mostly activated, leading to an increase of the D band. In sequence, the mostly structurally-disordered regions become increasingly widespread, leading to a decrease of the D band. The intensity of the D peak is proportional to the total S areas of crystalline graphene that area activated by local defects, not the areas of the defects themselves. Thus, as L_D becomes sufficiently low and the material becomes less crystalline, the D band intensity falls. This is illustrated in the overlapping defect regions in figure 2.4(b).

The dispersive effect of the excitation energy, E_l, on the ratio of excitation of the D and G bands, is included in the C_A parameter. It is a measure of the maximum possible value of the I_D/I_G ratio i.e. where K-K′ mixing is allowed everywhere but there is no structural damage to the graphene lattice. It is expected to be proportional to the fourth power of E_l, as predicted by time dependent perturbation theory

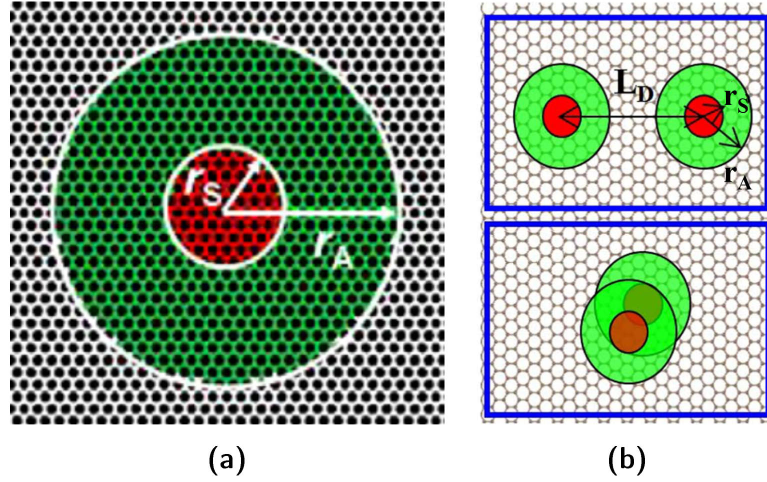

Figure 2.4: D band generation from regions adjacent to defect sites [26]. (a) shows the distances from the impact point of the ion to the edge of the A (r_A) and S (r_S) areas from Lucchese et al. [26]. (b) from Pan et al. shows the inter-defect distance (L_D) and the overlap between defect-activated regions typical in the highly disordered range [44].

[73]. Where E_l is stated in eV, C_A has been given experimentally by: [27]

$$C_A = (160 \pm 48) \times E_l^{-4} \tag{2.2}$$

The C_S parameter is the value of the I_D/I_G ratio in the highly disordered limit and it is important only in the large defect density regime, $L_D \leq r_S$ [26, 27]. Typically, three stages are discussed in the evolution of the relationship described by equation 2.1. The first stage begins with pristine graphene (having a very large L_D) and as disorder is increased, a rising D peak may be observed, increasing I_D/I_G. In addition, a broadening of all peaks occurs. It can be attributed to isolated defects initially appearing in a crystalline lattice. The second stage features a now diminishing D peak and the continued broadening and newly observed redshifting of the G peak. It is reached when L_D reaches a critical quantity such that defect coalescence is significant. The second stage can be attributed to the now dominant effect of a declining number of six-atom carbon rings present [26, 27, 29, 74]. The third stage is not described in detail here as it is in essence marked by the transition of the

specimen to amorphous carbon bearing limited or no resemblance to the original graphene.

Monolayer graphene has several clear factors distinguishing its Raman spectrum from those of bilayer and few layer graphene. Monolayer graphene has a single, sharp $2D$ peak, roughly four times more intense than the G peak (this can be less in the case of defective monolayer graphene, still distingusihed by being greater than twice as intense as the G peak) [65]. By comparison, the $2D$ band of bilayer graphene is upshifted, much broader and has four components. For more than five layers the Raman spectrum becomes hardly distinguishable from that of bulk graphite. The $2D$ peak in bulk graphite consists of two components $2D_1$ and $2D_2$, roughly a 1/4 and 1/2 the height of the G peak respectively. This evolution of the $2D$ peak as a function of graphene layer number is shown in figure 2.5. There are other effects of layer number on the G peak which are weaker indicators of layer number. The G band is shifted downward in frequency with increasing layer number but this is a very weak trend beyond bilayer graphene [64, 75].

The alteration of graphene by irradiation techniques has received much focus recently and is built upon in this work [26, 27, 29, 74]. Combining the Raman spectrum of graphene and equations 2.1 and 2.2 with a precise method for the introduction of defects allows the powerful manipulation of graphene's properties through defect-engineering. The model is so detailed that both the defect type and density can be distinguished. This will be demonstrated experimentally for supported and freestanding graphene irradiated with He^+ and Ne^+ in chapter 5.

2.2 Molybdenum Disulphide

In spite of its high carrier mobility, a key limitation of graphene is its zero band gap which restricts its ability to reach an effective 'off' state in devices. Although defect-engineering of graphene or its positioning in a heterostructure can cause the band gap to be opened, it appears inevitable that this sacrifices charge carrier mobility [76, 77]. As a result, much research is now devoted to other materials in the 2D family [6]. One promising family of 2D materials is that of the TMDs. Monolayer MoS_2 is one such TMD, which consists of alternating Mo and S_2 columns arranged in

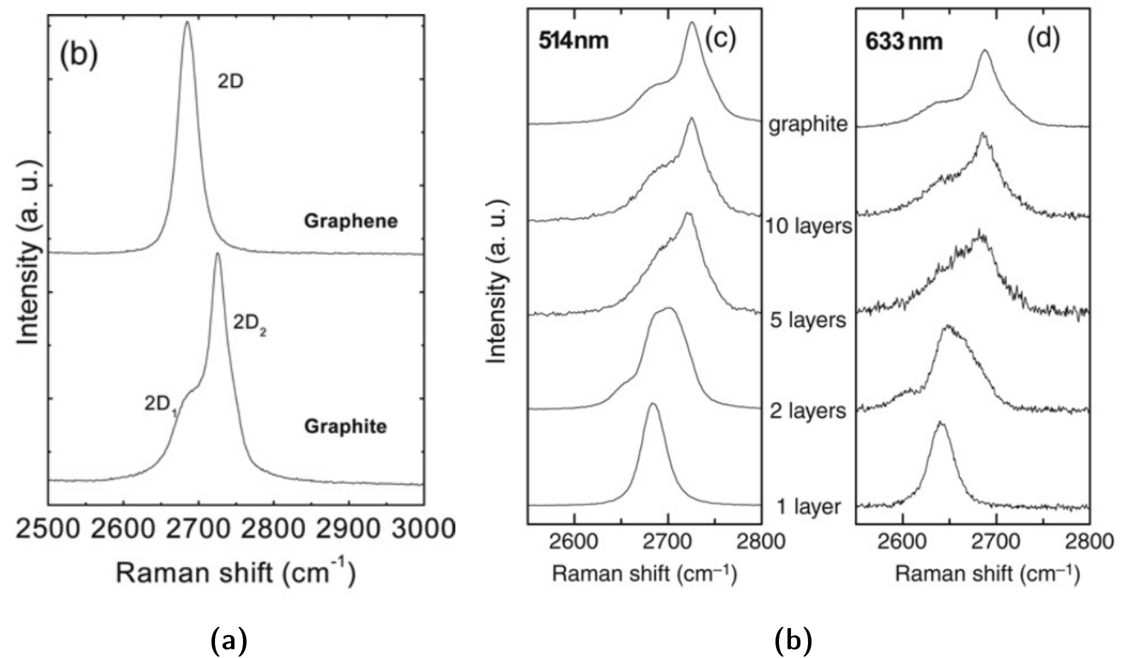

Figure 2.5: Evolution of the $2D$ peak as a function of number of layers [65]. 2.5(a) shows the $2D$ peak in the Raman spectrum of monolayer graphene and bulk graphite. 2.5(b) shows changes to the band as layer number changes for both 514 and 633 nm excitations.

hexagonal rings (see figure 2.7) and has a thickness of ~0.7 nm [20]. Unlike graphene, monolayer MoS_2 has a sizeable direct band gap of 1.8 eV. Interestingly, MoS_2 has an indirect band gap in the multi-layer system and a direct band gap in the monolayer [12, 78]. This suggests potential for application in digital electronics and numerous photonic applications such as light emitters, photodetectors and solar cells [79, 80]. Excellent mechanical flexibility also allows potential for use in flexible electronics [81].

The effects of strain and substrate [82, 83] and optical control [84] on the photoluminescence spectroscopy (PL) spectrum of MoS_2 have been reported. In the monolayer form, MoS_2 has a large direct band gap with intense emission [9, 10]. This intensity declines rapidly with increasing layer number. Figure 2.6(a) shows the calculated band structures of monolayer and bilayer MoS_2. Electronic states near the Γ point arise from orbitals with strong interlayer coupling and depend on layer number. However, conduction band states at the K point are in orbitals in the middle of the layer and because of this are independent of interlayer coupling [85, 86]. This coupling can also be reduced by folding which leads to an enhancement of the photoluminescence emission yield [86].

The method by which MoS_2 is synthesised is a major factor in its intrinsic defect density and type, its crystal size and the layer number [89]. Monolayer MoS_2 produced by mechanical exfoliation from bulk is widely regarded as the finest quality available. Monolayer MoS_2 produced by CVD instead can have reduced charge carrier mobility by around an order of magnitude in devices [90]. MoS_2 displays native n-type doping. Sulphur vacancies exist, even in high quality samples and these introduce localised donor states inside the band gap [91, 92]. Achieving p-type doping is much sought after and has been acheived by low energy phosphorus implantation [25], molybdenum oxide heterojunctions [93, 94] and partial oxidation [95, 96] amongst other techniques. However, none of these methods demonstrate the high control, spatial resolution and scalability that would be required for commerical purposes.

Raman spectroscopy has been employed extensively in the characterisation of MoS_2 in various forms such as bulk [98–101], powder [102], nanoparticles [103, 104] and few layer/monolayer [11, 105–108]. Group theory predicts four Raman-active

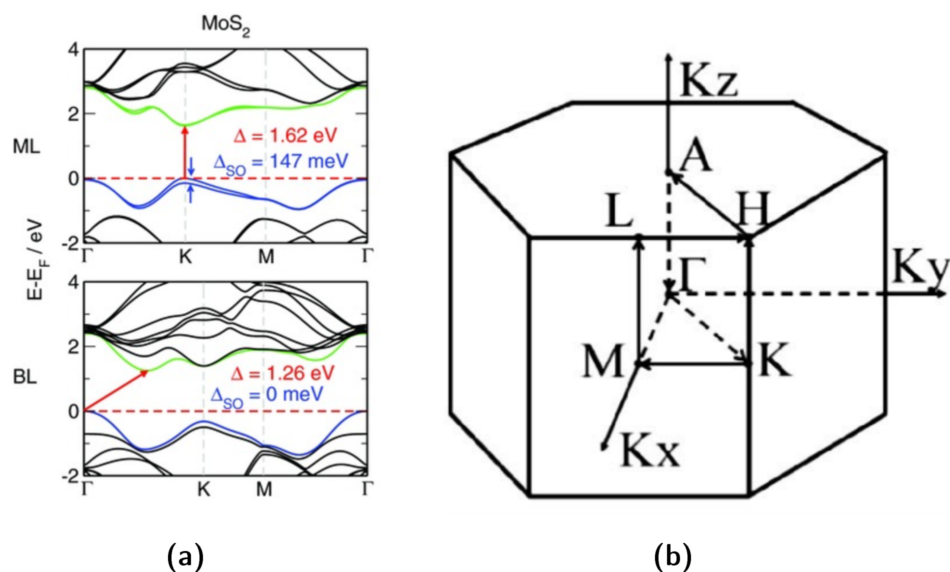

Figure 2.6: The Brillouin zone and band structure of MoS_2. (a) shows the band structure of monolayer (top) and bilayer (bottom) calculated by DFTMoS_2 [87]. (b) shows the first Brillouin zone of MoS_2 [88]

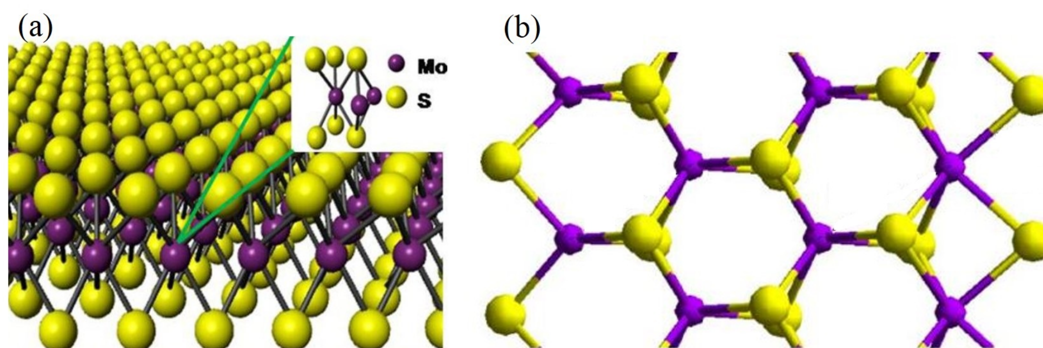

Figure 2.7: The crystal structure of monolayer MoS_2. A schematic diagram of the atomic structure of monolayer MoS_2 [97]. Mo atoms are shown in purple and S atoms are shown in yellow.

modes in bulk MoS_2 [98] (of polytype 2H, point group D_{6H}) corresponding to the following symmetries (wavenumbers for 514 nm excitation): E^2_{2g} (35 cm^{-1}), E_{1g} (286 cm^{-1}), E^1_{2g} (383 cm^{-1}) and A_{1g} (408 cm^{-1}). Other modes are expected to be infrared (IR)-active or silent [101].

In monolayer MoS_2 (of polytype 1H, point group D_{3H}), the phonon dispersion has been well described theoretically and computationally using DFT [109]. The results are in good agreement with experiment [101, 106, 109]. The bulk phonon dispersion of monolayer MoS_2 has three acoustic modes. The longitudinal acoustic (LA) and transverse acoustic (TA) modes vibrate in-plane, have a linear dispersion and a higher energy than the out-of-plane acoustic (ZA) mode which has a q^2 dependence [109]. The $LA(M)$ peak at ~227 cm^{-1} has been linked to the presence of a local maximum in the vibrational density of states, located at the energy corresponding to the longitudinal acoustic (LA) branch at the edge of the Brillouin zone. It exhibits no intensity in pristine monolayer MoS_2 but intensifies quickly with increased defect density [28, 103]. It is typically very weak and somewhat broad. It is also found in nanoparticle/few layer samples. Since it is defect-activated, it can be used somewhat analogously to the D band in graphene Raman spectra in the characterisation of defect density [28]. In resonance Raman spectroscopy, for a variety of MoS_2 arrangements the LA(M) mode is notable for its many second order interactions in spectra.

The high energy optical modes that are Raman active in monolayer MoS_2 are the following: the E' peak at ~385 cm^{-1} arises from the intralayer, **in plane** motion of Mo and S atoms with respect to each other and the A'_1 peak at ~405 cm^{-1} arises from the intralayer, **out of plane** motion of S atoms. Both the E' and the A'_1 peaks are strong in all forms of MoS_2

For few layer MoS_2, additional peaks arise and there are changes to the labelling of previously existing peaks. These extra peaks include low frequency modes which are discussed further below and the E_{1g} peak at ~286 cm^{-1}. Since there is a lack of translational symmetry along the z axis, there is a reduction in symmetry in few layer TMDs, for odd layer numbers, MoS_2 has D_{3H} point group symmetry. For even numbers, the point group is D_{3d} because of the existence of inversion symmetry. Therefore for bulk or even layer number MoS_2, the E^1_{2g} and A'_{1g} peaks replace the

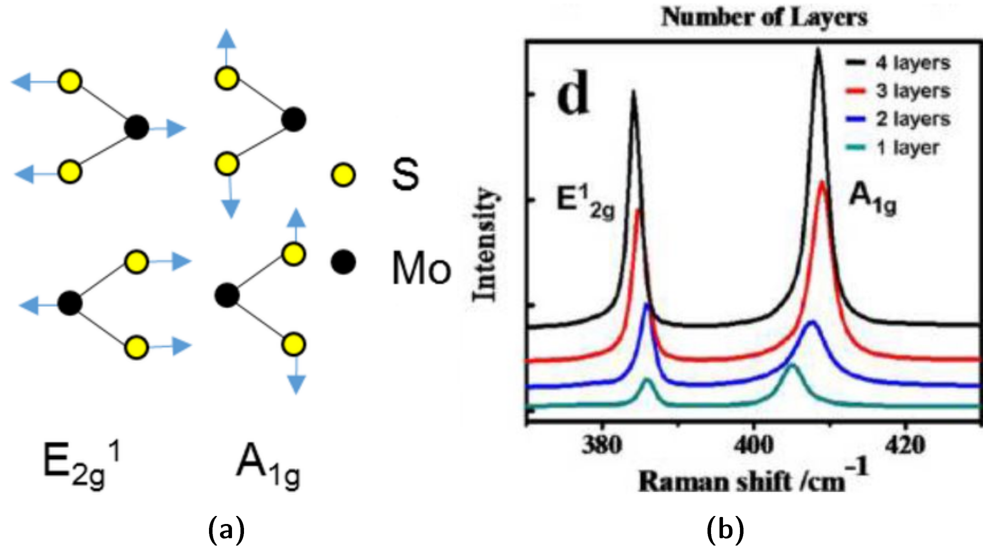

Figure 2.8: Vibrational modes and Raman spectroscopy for the differentiation of the number of MoS_2 layers thinned by plasma [12, 13]. (a) shows the vibrational modes giving rise to both peaks in the part of the Raman spectra shown in (b).

E' and A_1' peaks [110]. Peak separation is a key characteristic in distinguishing layer numbers [12, 106, 111, 112]. Figure 2.8 shows the evolution of Raman spectra extracted from 1-4L MoS_2. With increasing layer number, a characteristic red shift of the E'/E_{2g}^1 (385 cm^{-1} to 382 cm^{-1}) and blue shift of the A_1'/A_{1g} (404 cm^{-1} to 407 cm^{-1}) modes is observed. With increasing sample thickness, a classical model for coupled harmonic oscillators would suggest that both peaks would blue shift. However, this is a simplistic view for 2D materials [13]. While the A_{1g} vibration does blue shift,the E_{2g}^1 vibration in fact **red shifts**, possibly the result of surface relaxation and additional interlayer interactions for few-layer samples [11–13]. For four or more layers, the values of frequency converge to bulk values. With regard to the width of the observed peaks, the E'/E_{2g}^1 peak is largely independent of thickness. It has been reported that the width of the A_1'/A_{1g} peak drops going from 2 to 6 layers but it remains difficult to use this to distinguish between layer numbers [11, 106].

The evolution of the Raman spectra of monolayer MoS_2 with decreasing L_D has been described by Mignuzzi et al. as follows: The intensity of the $LA(M)$ peak, $I(LA)$, normalized to that of either the E' peak, $\frac{I(LA)}{I(E')}$, or the A_1' peak, $\frac{I(LA)}{I(A_1')}$, is related to

the inverse square of L_D (as with graphene, the average distance between defects) by equation 2.3 [28]:

$$\frac{I(LA)}{I(X)} = \frac{C(X)}{L_D^2} \tag{2.3}$$

In the case where the Raman spectrum was acquired with a 532 nm laser, the following constants were found by fitting experimental data: $C(E') = 1.11 \pm 0.08\ nm^2$ and $C(A'_1) = 0.59 \pm 0.03\ nm^2$. $X = E'$ or A'_1 for depending on the peak studied. With rising disorder, the increase of these intensity ratios is attributed to two concomitant factors: (i) an increase in the absolute intensity of the defect-activated $LA(M)$ peak, and (ii) a decrease in the intensity of the E' and A'_1 peaks that is possibly due to the ablation of the specimen [28]. Naturally, samples have an initial value for defect density as a function of their preparation method. Even 'pristine' 2D materials used in this work have a non-infinite initial L_D subject to variation between samples prepared by different methods.

Chapter 3

Modification Methodology

In chapter 2, the two key materials of this work were identified, namely graphene and MoS_2, and some of their extraordinary properties were described. In this chapter, the field of nanomaterial engineering will be introduced and the modification methods which dominate this work will be highlighted. The primary method used in this work for the modification of 2D materials is by the application of an energetic ion beam in an ion microscope which is capable of nanoscale resolution. These ion microscopes as ion sources will be briefly described and there will be an exploration of the ion-beam sample interaction. Methods for simulating ion beam interactions such as molecular dynamics and Stopping and Range of Ions in Matter software (SRIM) are also introduced and discussed.

Another modification method uses a high energy electron beam in a scanning electron microscope (SEM) to excite gas atoms for reactions with a surface. Finally, the alteration of MoS_2 by oxidation in air is discussed in detail, as it will be shown to be highly controllable through the use of ion irradiation.

3.1 Nanomaterial Engineering

Of far greater interest than the already extraordinary family of 2D materials is the behaviour of those materials once engineered, especially if done on the nanoscale. In order to realise cost-effective device manufacture, it may be desirable to engage a method which can alter all of these properties with precision, high resolution (scale

of 10s of nanometres) and throughput. At present, scalable modification is often achieved by a wide variety of methods including defect-engineering in synthesis, or with plasma or ion implantation, doping by a range of techniques including chemical reactions and ion irradiation, encasement in other materials to create heterostructures and more. While chemical reactions and plasma etching can have a great deal of control over properties, they are typically unable to do so with much spatial specificity. It has been shown previously in experiments and simulations that ion and electron irradiation can selectively etch or alter the properties of selected regions of 2D materials with high spatial resolution [37, 41, 113–116]. Sputtering is the removal of near-surface atoms from a target, and the sputtering yield is the mean number of sputtered target atoms per incident electron/ion. Broadly speaking, electron beams can achieve atomic or near-atomic resolution but with a throughput much lower than that of ion beam techniques due to their lower sputtering yield. Ion beam methods can still achieve several nanometre resolution at a fraction of the cost/time.

Considerable alteration of 2D materials is possible by tailoring the **crystal structure/defect density**, **layer number**, **stoichiometry/doping state** and **geometry** including polytypes and nanostructures like pores and nanoribbons. Defects have been introduced to MoS_2 on a large scale during CVD with extensive control over the resulting electrical properties [20, 90]. DFT simulations have demonstrated that the modification of **crystal structure** by the controlled addition of defects can be used to tune the electronic structure and transport properties of MoS_2 [117]. While electron transport is practically isotropic in pristine MoS_2, strong anisotropy is observed in the presence of defects. Localised midgap states are observed in semiconducting MoS_2 that do not contribute to the conductivity but scatter the current with direction-dependency.

Since there is such a significant difference in the behaviour of single layer versus bulk MoS_2 (including the considerably different band structure as previously discussed), thinning of MoS_2 has been researched using a wide variety of different techniques. These include laser ablation, ion/electron irradiation and chemical reactions e.g. XeF_2 and Ar^+ plasma etching [12, 37, 112, 118]. Laser ablation is diffraction limited in terms of spatial resolution and electron irradiation is typically limited in throughput.

Devices fabricated from MoS_2 monolayers with lower sulphur in their **stoichiometry** have negligible current-voltage hysteresis and a threshold voltage of ~0 V [119]. Alteration of the **geometry** of MoS_2 can also result in modified electrical and magnetic behaviour [22]. It will be shown in this thesis that all of these characteristics can be altered to some extent using ion irradiation.

With regard to **geometry**, nanoribbons are particularly desired. These strips of extremely thin and narrow material (typically defined as having a width of less than 100 nm), can have superlative properties especially with pristine crystallinity and edges of a specified orientation (i.e. zigzag, armchair) [120]. Simulations show that MoS_2 nanoribbons with such edge orientations and widths of ~3 nm (within the quantum confinement regime) can be vastly different in behaviour depending on the edge termination. For example, zigzag MoS_2 nanoribbons are ferromagnetic and half-metallic whereas armchair MoS_2 nanoribbons are non-magnetic and semiconducting [17, 22, 121]. Of the many methods used to fabricate nanoribbons in MoS_2, few have achieved all of the following: good crystal structure, well-defined edges, reproducibility and widths of less than 10 nm [30, 31]. Electron irradiation in a TEM has been used to fabricate ribbons of MoS_2 down to sub-nanometre widths [33]. However, the TEM is a low throughput fabrication tool due to a relatively weak beam-sample interaction and stringent sample requirements (supported, thin, low levels of contaminants, vacuum stable). Similarly, nanoribbons of graphene have been fabricated using scanning probe microscope-based lithography, but again issues of throughput and controllability persist [122–124].

3.2 Ion Beams

The conventional FIB has been commonplace for several decades and uses a liquid metal ion source (LMIS) to accelerate gallium ions (Ga^+) to energies in the typical range of 1-30 keV. In operation, Ga^+ is focused into a fine probe, which on modern instruments can be small enough to obtain image resolutions in the 3 to 5 nm range [125]. Due to the energy and large mass of Ga^+, there is a very strong sample interaction, which causes the sputtering of specimen material. For imaging purposes, this causes the small detail being examined to be removed during image acquisition

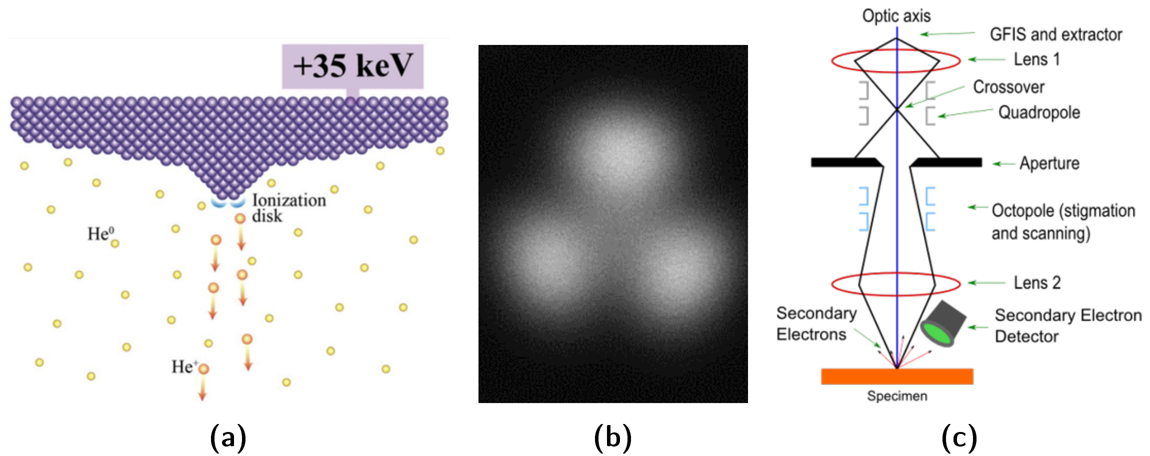

Figure 3.1: The GFIS in the GIM. (a) A schematic view of a GFIS [127]. (b) Imaging a trimer in SFIM mode in a Gas Field Ion Source microscope [126]. (c) Schematic of a GFIS microscope [126].

[125]. Thus, many of the uses of a Ga^{+} ion beam are related to micromachining and nanofabrication rather than imaging [126].

The gas ion microscope (GIM) is a more recent development with very different underlying physics governing its ion source [126, 128, 129]. One such tool is the *Zeiss ORION* series of microscopes such as the *Zeiss ORION Plus* (He^{+}) and *Zeiss ORION Nanofab* (He^{+} or Ne^{+}) utilised in this work. The *ORION Nanofab* is equipped for operation with two types of gas using the same source and optics, and switching gases is fast and simple. The GIM utilises a pyramidal GFIS to accelerate gas ions as shown in figure 3.1(a). The source can be imaged in a scanning field ion microscopy (SFIM) mode which maps the positions and intensities of emitter atoms as shown in figure 3.1(b). A tip of three associated tip tungsten atoms (trimer) as pictured is found to be both stable and bright when compared to other configurations such as a dimer or a single atom source [126, 128]. The best imaging voltage (BIV) is the extractor voltage which gives the maximum current from the three atoms of the trimer. Although it will vary for emitters of different shapes, it is typically around 25 to 35 keV [126]. A quadrupole electrostatic lens system is used in the upper column for beam alignment and an octupole is used in the lower column for the correction of astigmatism.

As in SEM and FIB, images are formed in the *Nanofab* microscope by detecting secondary electrons generated by the primary beam. However, these images present different information than in SEM. This is because of the different nature of the ion beam-sample interaction and resultant significantly smaller penetration depth of ions compared to electrons. Images acquired using He^+ are much more surface sensitive than energetically equal electrons [113]. It is found that in imaging applications and using He^+, the GIM can outperform the SEM, given its smaller interaction range (hundreds of nm compared to μm) and probe size (0.35 nm compared to ~0.8 nm for a world class SEM) [126, 128–130]. Due to the relatively low mass of He^+ compared to other available accelerated ions it has a lesser ability to sputter material when compared to either Ne^+ or Ga^+ at the same angle and energy. However, its interaction at the specimen surface is still far greater than that of an electron beam of equal current. Given its much higher mass, Ne^+ has an enhanced calculated milling capability compared to He^+ (at least an order of magnitude for copper at an energy of 20 keV) [129].

Due to the very high brightness of the GFIS source, the attainable probe size of 0.3-0.5 nm in He^+ mode is much smaller than that of Ga^+ in the FIB. Potential resolution of the Ne^+ mode when further developed is also suggested to be as low as sub-nanometre [129]. However, in practice the current achievable probe size of Ne^+ is approximately 2.5-5 nm which is similar to Ga^+.

3.3 Ion Beam Sample Interaction

Ion irradiation has an illustrious record over many decades in the scalable, precise defect-engineering of materials [23]. Given the pivotal importance of defect-engineering and nanofabrication methods in the materials science of today, it is imperative that the capabilities and side-effects of ion beam fabrication methods on 2D materials be well understood. The ion species and energies used in this work are particularly significant due to their high resolution capability for nanofabrication and defect-engineering.

To precisely irradiate material to alter its properties, it is critically important that the interaction between specimen atoms and the incident ion beam be understood.

As a beam of ions reaches the specimen, collisions with the surface will transfer energy to the sample. The maximum transferable energy from an ion to a specimen atom by elastic scattering (modelling the atom and ion as two spheres, reasonable given the high energies involved), T_m, depends on the particle energy, E, and the ratio of the ion mass, M_2, to the specimen atom mass, M_1 [23], where:

$$T_m = \frac{4M_1M_2}{(M_1 + M_2)^2}E \tag{3.1}$$

An ion interaction leading to the removal of a specimen atom has a cross-section $\sigma_{d(ion)}$. This is given in equation 3.2 where e is the charge of an electron, Z_1 and Z_2 are the atomic numbers of the specimen atoms and beam ions respectively, and T_D is the threshold displacement energy of the specimen atom, such that [23]:

$$\sigma_{d(ion)} = \pi\frac{M_1}{M_2}Z_1^2Z_2^2e^4\frac{1}{E}\left(\frac{1}{T_D} - \frac{1}{T_m}\right) \tag{3.2}$$

3.4 Simulating Ion Interactions

SRIM is a software package, which is used to model the interaction of ions with matter. The trajectory and penetration depth of an ion beam can be simulated in a specimen surface with a variety of inputs including ion species and energy and the specimen composition [131]. SRIM is based on a Monte Carlo simulation method, namely the binary collision approximation. In calculating the sputtering yield of atoms from a supported 2D material, SRIM accounts for: those atoms directly removed by the primary ion beam, those which are removed by backscattered primary ions and those which are removed by secondary atoms, excited in the substrate near the surface. It is a singularly useful tool for comparing the effects of ion energy and species on the milling and patterning of materials. Figure 3.2 shows a comparison of the trajectories of He^+, Ne^+ and Ga^+ into a 4 nm layer of MoS_2 on a substrate of magnesium oxide (MgO) calculated using SRIM.

However, SRIM is not expected to be completely quantitatively accurate for ion-nanomaterial systems. There are several assumptions and caveats therein which much be considered. For instance, SRIM relies upon the binary collision approximation, assuming an amorphous structure and homogeneous mass density for all materials. This means that orientation dependent phenomena such as ion channelling

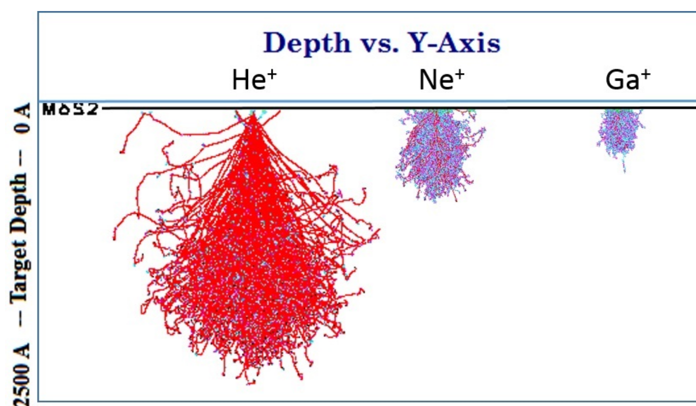

Figure 3.2: A Stopping and Range of Ions in Matter software simulation of ion trajectories. The figure shows a calculation for 30 keV He^+, Ne^+ and Ga^+ beams incident on a 4 nm layer of MoS_2 sitting on a substrate of MgO.

are neglected. The amorphous structure assumed here is also highly inapplicable to measurements of 2D materials due their typically highly ordered lattices and their 2D nature.

Therefore, molecular dynamics and DFT are in many cases a superior choice where accuracy in 2D material systems is concerned. However both are far more computationally expensive choices with DFT being particularly so [28, 34, 132–135]. While SRIM and molecular dynamics methods do not distinguish between the effects of atoms and ions (chemical effects) these are expected to be negligible in this work given the high energies of the direct ion beam. Where possible, values calculated from molecular dynamics in the literature are referred to rather than SRIM.

3.5 Dose and Substrate Effects

The direct beam can be used to modify geometry by the removal of material to produce nanostructures such as nanoribbons. This requires using sufficient ions per unit area, also known as dose. However, if insufficient doses are used, the result is structural damage only and not the desired area-specific removal of material. A beam of ions cannot be focused to a zero sized probe, so damage to surrounding

material is unavoidable. Excessive doses are undesirable due to the way in which they exacerbate this effect while also reducing fabrication throughput. In addition, the resolution of long exposures may be subject to drift of the sample with respect to the beam. Since modelling and reducing the impact of undesired damage will be one of the challenges of this work, optimising the irradiation dose for complete milling is of great importance. As an example, the dose required to remove a layer of supported MoS_2 will be estimated. Since the area of the MoS_2 unit cell (a = 0.31625 nm) is ~0.14 nm^2, there are 1.5×10^{15} cm^{-2} sulphur atoms and 7.3×10^{14} cm^{-2} molybdenum atoms. An estimate for the dose of ions, D, required to remove a given area is given by

$$D = N/P \tag{3.3}$$

where N is the total number atoms per unit area and P is the average probability of removing an atom. Here we use the sputtering yield as calculated from SRIM simulations (see section 3.4) for He^+ at 30 keV, $P = 0.03$. This method ignores the distribution of such atoms and will thus underestimate the true dose. The effects of ion beam-induced deposition will also cause an underestimation. However, the value of D obtained is of the order 1×10^{17} cm^{-2} which has been found in preliminary experiments to be correct to within an order of magnitude, see chapter 6.

Irradiation induced defects in 2D materials come from two main divisions: those introduced directly by the ion beam and, in the case of supported samples, there are also defects introduced indirectly by the interaction of backscattered primary particles and secondary sputtered substrate atoms [136]. The difference in the behaviour of 2D materials between supported and freestanding geometries is important especially when under ion irradiation as the effects of secondary atoms are profound. Such atoms have a much lower energy and therefore by equation (3.2) a much higher cross section for sputtering interaction with the atoms at the surface. These collisions occur to a far greater extent for supported material where the substrate both facilitates backscattering of the primary ion beam and provides a source of secondary atoms [136]. For high energy ions, a substrate is expected to increase the rate of damage per ion given the supply of secondary atoms and backscattered ions. For low energy ions, a substrate is expected to greatly lower the damage probability per ion. Zhao et al. found that the energies above which irradiation damage was enhanced in

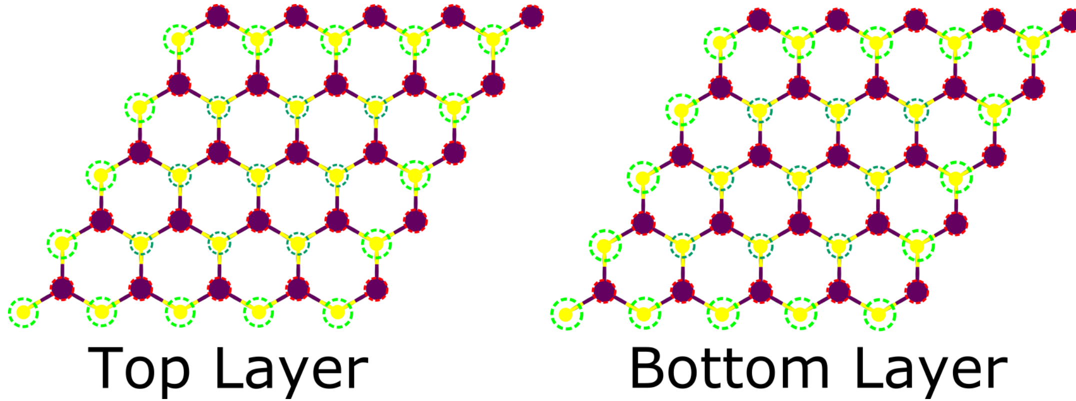

Figure 3.3: Displacement cross sections of atoms in MoS_2 with 30 keV He^+. Mo atoms are shown in purple and S atoms are shown in yellow. The size of the circles shown in dotted lines represents the sputtering cross sections of the respective atoms.

supported graphene (on a substrate of SiO_2) were 5 keV and 3 keV for Ar^+ (M=18) and Si^+ (M=14) respectively [136].

3.6 Displacement Threshold in MoS_2

Most experimental studies of the sputtering of MoS_2 note that S atoms are sputtered preferentially. Since they also make up two thirds of the total atoms and there are no Mo-Mo bonds in pristine MoS_2, it is reasonable to say that to remove all material (from a freestanding sample at least) it is essentially necessary only to directly remove the S atoms. For that reason, the removal of S atoms will be explored in some detail. The displacement threshold of an S atom is a major factor in deciding the probability of sputtering as in equation (3.2), see figure 3.3.

Within a sample of MoS_2 there are many factors affecting the displacement threshold value. The first is that assuming a 0° angle of incidence in MoS_2, the displacement threshold of S atoms in the top layer (nearer the beam) are considerably higher than for the bottom layer (T_D = 6.9 eV for bottom, 8.1 eV for top) [115]. It is thought that a reason for this is that the displaced atom can be stopped by the other layers. Another factor is whether the S atom is near an existing edge or defect

site. In tungsten disulphide (WS_2) the displacement energy for S atoms at the edge is 4.2 eV compared to 7.0 eV away from the edge[1] [115].

3.7 Ion Beams and 2D Materials

With the demands of modern semiconductor technology, precise nanoscale control of 2D material properties is much sought after and eminently achievable using modern ion irradiation techniques with sub-nanometre probe sizes [35–40, 113]. Given the superlative confinement of such materials, it is possible to restrict the ion-induced effects to an exceptionally small region. Such methods have been used to create nanoribbons with widths of less than 10 nm [36, 37, 137], control doping of graphene by implantation [25] and introduce precise quantities of defects [27–29]. Ribbon widths of this magnitude may be useful in order to exploit the properties of quantum confinement. However, nanoribbons must also have well-defined edge orientations and good crystallinity which are limited by a shortfall in our understanding and subsequent control of the beam-sample interaction. Whether this can be achieved by He^+ milling has not yet been reported and fabricated edges have been insufficiently studied to date by methods of sufficient resolution. Effects of the same scanning strategies varied across materials have also not been investigated to any meaningful extent.

More nuanced and innovative uses are also possible than simple direct write milling. He^+ irradiation of graphene encapsulated in hexagonal boron nitride has even been used to introduce n-type doping [41]. Defect-engineering is also readily achievable with a great deal of both precision and spatial resolution. A host of optical, mechanical and electronic properties can be controlled in this way, by using the He^+ beam to create vacancies [138].

In short, the further development of irradiation methods for a given material is predicated on a thorough understanding of the relationship between irradiation strategy and dose and the corresponding rate of defect introduction and the nature and size of defects. The spatial spread of beam-induced effects is also of paramount

[1] This 40% difference was used to estimate the value for MoS_2 in figure 3.3

importance, limiting the ultimate minimum feature size, of critical importance to nanofabrication.

3.8 Electron Beams and Defects

Another modification method used in this work is the etching of graphene in a SEM using nitrogen activated by the electron beam. While the SEM has been shown to be capable of selective deposition and removal of material, an electron beam of typical energy in a SEM ($<$30 keV) is not energetic enough to efficiently sputter carbon atoms. However etching is quickly and efficiently achieved by other methods including the introduction of a gas into the system [139–142]. The electron beam is used to generate reactive ions which locally etch the sample surface in close proximity to spots defined by the microscope [140, 141, 143]. This technique provides direct, top-down fabrication of nanostructures using a maskless and resistless process. Of particular interest is the ability to create nanopores in graphene.

Oxygen is the most commonly used gas as the etching species. State of the art e-beam etching was recently demonstrated with water vapour, producing feature sizes down to 7 nm [142]. Etching of a graphene surface has previously been observed to occur when it was irradiated with an electron beam in a nitrogen atmosphere [143]. In chapter 5 nitrogen gas is shown to be preferable to oxygen as it reacts less aggressively with the graphene, allowing smaller feature sizes, down to 4.5 nm, to be demonstrated compared to other methods.

3.9 Oxidation of FLM-MoS_2 in the Literature

The oxidation of MoS_2 to MoO_x considerably affects its electronic, chemical, optical, and tribological properties, of paramount importance given its use in bulk and powdered forms as an industrial lubricant for many decades [144]. The material switches from hydrophobic to hydrophilic upon oxidation and its mechanical stability is reduced leading to failure [145, 146]. Given this long history, the reaction has been well scrutinised as a function of temperature, time, humidity and other parameters. When heated in the presence of oxygen, the Mo and S atoms react to form

molybdenum trioxide (MoO_3) and sulphur dioxide (SO_2) molecules, respectively.

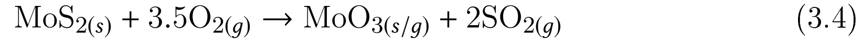

$$MoS_{2(s)} + 3.5O_{2(g)} \rightarrow MoO_{3(s/g)} + 2SO_{2(g)} \quad (3.4)$$

The temperature at which the reaction occurs depends greatly on the condition of the material with pulverised MoS_2 having oxygen content at temperatures as low as 100°C and some coatings being stable up to 400 °C [144, 147]. The case of the oxidative reaction of few layer or monolayer (FLM)-MoS_2 is of far greater interest to the modern nanomaterials scientist and has been developed to a far lesser extent due to the relatively recent proliferation of the material. Yet, the implications for applications under the categories of device fabrication, stability and defect-engineering/doping are profound. FLM-MoS_2 is much more reactive to molecular oxygen (O_2) than an analogous atomic membrane of graphene [148]. It has recently become clear that chemical oxidation occurs preferentially at edges and defect sites [148, 149].

Oxidation has been demonstrated to alter the doping state and performance of FLM-MoS_2 devices and to thin or even completely etch FLM-MoS_2 [20, 95, 148]. McDonnell et al. demonstrated MoO_x as an efficient hole injection layer for p-type field effect transistors (FETs) in TMDs [94]. It is well-established that the oxidative thinning and/or etching of FLM-MoS_2 can be achieved by heating in the presence of O_2 or other oxidants [95, 118, 148, 150, 151]. However, there remains a great deal of room for expanding on this knowledge. For instance, the behaviour of MoO_3 as a reaction product is complex due to its volatility. Whether it sublimes or at least partially remains after the oxidation of FLM-MoS_2 seems to be heavily dependent on the thickness of the starting material [148]. However, there appears to be no proposed mechanism for this phenomenon.

Nanosized MoO_3 is known to be considerably more volatile than in bulk [152]. The sublimation temperature for bulk MoO_3 is about 700°C, but this can be substantially less for nanoscale MoO_3 [144, 152, 153]. Desorption of MoO_3 at ~500°C in vacuum has been reported, allowing atomic layer etching without altering the underlying crystal structure of MoS_2 [154]. At temperatures at which etching or thinning of FLM-MoS_2 is observed (~300°C) additional heat generated from the exothermic reaction may assist in the sublimation of the newly formed MoO_3. Zhu et al. used

a plasma oxidation method and showed that at 400°C the desorption rate of surface oxides is higher than the oxidation rate [154]. This does not exclude the possibility that there is some range of parameters at which MoS_2 oxidation dominates over MoO_3 sublimation, but it is unlikely that FLM-MoS_2 will leave behind large amounts of MoO_3 in typical oxidation conditions.

In reports of bulk and powdered MoS_2 the oxide remains and its relative content can be measured [144, 153]. For non-bulk, but still relatively thick MoS_2 (> 40 nm), oxygen treatment at 400°C was found by Raman spectroscopy to result in conversion to MoO_3 platelets [148]. While no oxide could be found by Yamamoto et al. using the same methods for thinner samples (1-4L), Wu et al. did find evidence of MoO_3 using magnetic force microscopy (MFM) and atomic force microscopy (AFM). They concluded that a discontinuous oxide layer acted as a hole-injection layer, resulting in the p-type doping of the material. This p-type doping has been predicted and found elsewhere which lends considerable credence to at least one of two suggestions: there may be certain heat/time/temperature scenarios where MoO_3 evaporation is not complete, or there is high oxygen content to be found, but only in strictly localised near-edge regions.

A DFT study by K. C. et al. found that the adsorption of molecular oxygen on the monolayer MoS_2 surface is limited kinetically by a large energy barrier despite being thermodynamically favourable [155]. A key figure of scale here is the number of sites available on the surface for adsorption, 1.15×10^{15} O $atoms/cm^2$. The authors found the kinetic energy barrier for adsorption to be relatively high at 1.59 eV, affirming the chemical stability of the surface at atmospheric conditions. However, in the presence of a surface sulphur vacancy defect, the oxygen adsorption barrier and subsequent dissociation barrier are reduced by half (~0.8 eV). Thus when the S deficient MoS_2 surface is exposed to the atmosphere, it will be readily filled by oxygen. For low defect concentrations -typical in high quality specimens- the electronic properties are not changed significantly. However, as the concentration of impurity states increases (and hence O coverage), the band gap decreases from 1.76 eV for pristine MoS_2 to 1.4 eV when saturated with adsorbed O atoms [155].

Although well below their reported etching/thinning temperature, Yamamoto et al. found that oxygen exposure above 200°C resulted in an upshift in the frequency

and decrease in the linewidth of the Raman A_1' mode[148]. Other studies have shown using experiments, DFT and symmetry arguments that these effects on the A_1' mode represent a strong electron interaction for that optical phonon and electron density is significantly diminished by oxygen treatment [105, 156]. This is likely attributable to adsorption rather than oxidation at temperatures below 200°C . Neupane et al. performed experiments similar to the above studies but with a dry O_2 gas [157]. They found that etching could occur at temperatures as low as 270°C.

Wu et al. found thinning and etching of few layer MoS_2 to occur in air at 330°C after 60 mins [95]. They reported thinning as shown in before (a),(b) and after (c),(d) optical images of figure (3.4). Samples were frequently thinned to 1L rather than being completely etched. The authors offered an explanation for this which consists of thinning originating at the edge/active sites of the MoS_2 nanosheet. Heat then dissipates slower between MoS_2 layers than between the bottom MoS_2 layer and the silicon dioxide (SiO_2)/Si, substrate which acts as a heat sink, serving to protect this bottom layer [112]. Samples, which were thinned to 1L demonstrated comparable optical (PL spectra) and electrical properties (IV characteristics) to their mechanically exfoliated, pristine 1L equivalent as shown in the Raman spectrum of figure 3.4 (e). Neupane et al. demonstrated in Raman and PL that annealing in H_2 caused a reversal in the effects of adsorbed oxygen on the doping state of the remaining material [157].

Wu et al. reported the etching of equilateral triangular pits which left behind a mesh of MoS_2 after heating, particularly for long heating times (15 h) [95]. These pits are shown in AFM images in figure 3.4 (c,d). These triangular pits had the same orientation within a specimen flake and were found to be of diverse size, typically less than 200 nm. Optical microscopy (OM), AFM, MFM and X-ray photoelectron spectroscopy (XPS) were all used to investigate the material, which remained in the mesh structure. The authors reported conversion of the intrinsically n-type MoS_2 to p-type MoS_2 (using gated electrical characterisation) upon thinning, attributing this to the existence of MoO_3 on the thinned MoS_2. Ionescu et al. used similar methods and discussed triangular, star, and hybrid etched patterns [151].

Yamamoto et al. looked at the etched pits and showed that they grow faster with both increasing oxidation time and temperature. However, they also found that the

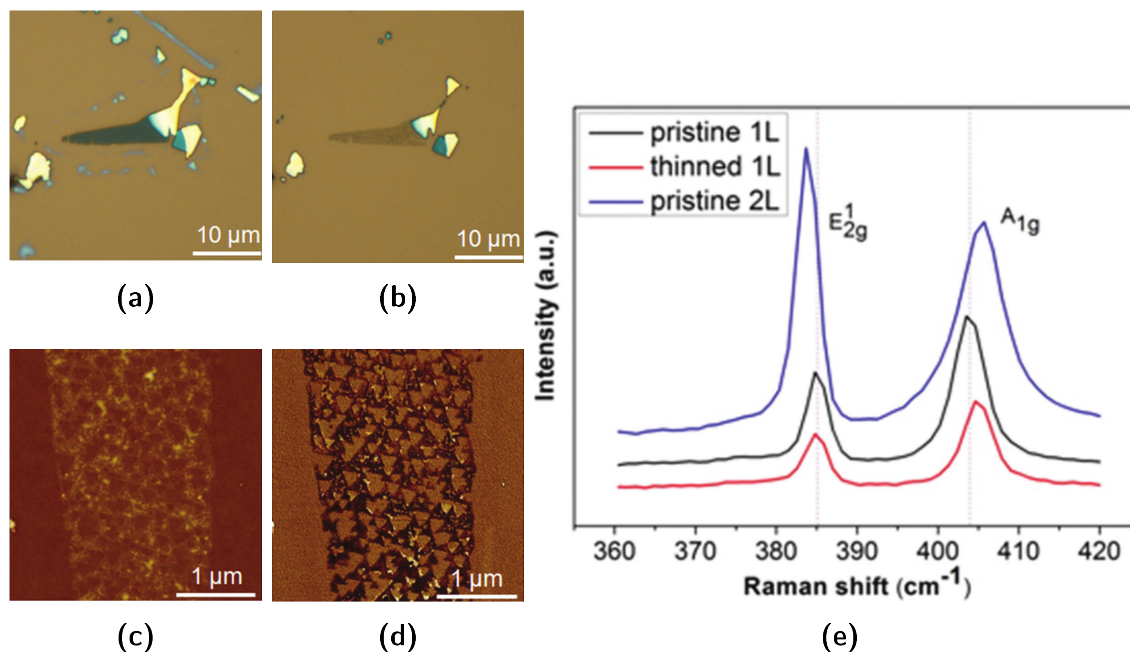

Figure 3.4: Thermal thinning and etching of 2L MoS_2 nanosheets. Wu et al. showed thermal thinning (a),(b), and etching (c),(d), of 2L MoS_2 nanosheets to 1L MoS_2 at 330°C for 10 h [95]. Optical images of a MoS_2 nanosheet before (a) and after (b) thermal annealing. AFM height (c) and phase (d) images of the same MoS_2 nanosheet shown in (b) after thermal annealing. (e) Raman spectra of pristine 1L MoS_2, pristine 2L MoS_2 and 1L MoS_2 produced from 2L MoS_2 by thermal annealing.

density of etched pits is largely uncorrelated with oxidation time (1h to 6 h), oxidation temperature (once above ~250°C) and MoS_2 thickness when compared to variations between samples [148, 149]. A clear implication is that oxidative etching of MoS_2 is initiated at intrinsic defect sites, the concentration of which varies substantially between samples. In broad agreement with the previous studies, etching was not observed below 340°C.

Rao et al. used Raman spectroscopy in oxidation experiments over a wide range of temperatures (330-1100°C) [158]. The decline of the monolayer MoS_2 peak intensities was faster at higher temperatures. The measured decay rate in multilayer MoS_2 (from an Arrhenius plot of the A_1g peak decay rate) provided a reaction energy of ~0.54 eV. Since calculated theoretical values for this energy barrier (1-5 eV) are higher, it is concluded that this is the reaction energy for *defective* MoS_2 and that defects in MoS_2 are essential to the reaction rates observed at the temperatures used in similar works [155, 158].

Zhou et al. performed first principles calculations (DFT) and experiments to investigate the formation mechanism of the triangular pits [150]. The authors studied three main types of edges for the etched triangles: Mo terminated zig-zag edge (ZZ-Mo), S_2 terminated zig-zag edge (ZZ-S_2) and armchair-terminated edge (AC). The pit cannot be composed of AC edges since it would have a hexagonal shape due to the six-fold symmetry of AC directions. Therefore, the MoS_2 layer typically exposes one of the zig-zag terminated edges (ZZs) [159, 160]. Zhou et al. went on to find that the oxidation of the ZZ-Mo edge had the more exothermic first step as shown in figure 3.5 [150]. This was also found by Gan et al. who used DFT and experiments to find that the equilibrium morphology of etched triangles is the ZZ-Mo edge, with each Mo atom bonded to two O atoms in a wide range of O chemical potentials. Furthermore, edges induced by O etching are p-doped, suggesting an effective strategy to realise p-type MoS_2 devices.

It is widely found that the approximately triangular etched pits formed by oxidation of few layer MoS_2 conform to one orientation on a given flake of uniform thickness [95, 148, 150, 161]. The resemblance of the pits and their host triangle to the Sierpinski triangle fractal set is notable. The lowest-energy stacking order of MoS_2 sheets is composed of Mo atoms in each layer being directly on top of the S

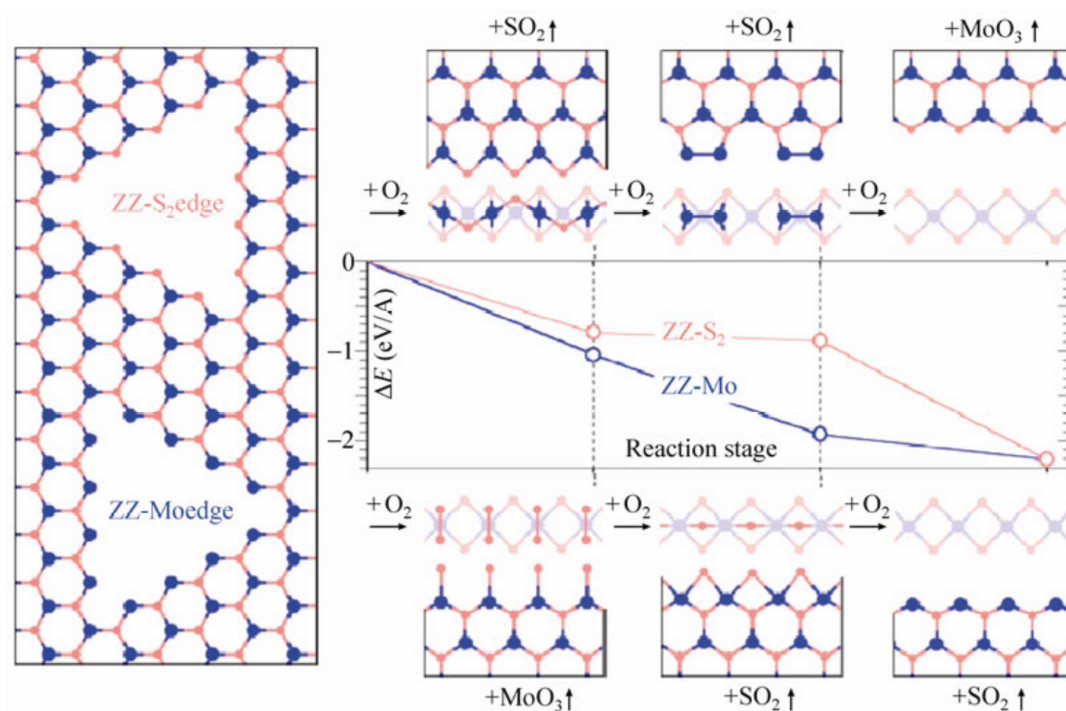

Figure 3.5: Modelling the etching of triangular pits in MoS_2 by Zhou et al. [150]. An atomic mechanism shows the formation of triangular pits in MoS_2 layers. The Mo and S atoms are represented by large (blue) and small (red) circles, respectively. Right: The atomic edge structures (top and side views) during oxidation of ZZ-Mo are shown in the bottom panels, and those for ZZ-S_2 are displayed in the top panels. In the side views, only two ZZ rows near the edge are rendered for clarity, where the deeper one is shown in pale color. The edge energy variations during oxidation are shown in the middle, where the energy of the oxygen-intact edge is set as zero.

Ref.	Sample	T_{min}	T_{ads}	Time	Gas	Oxide Detection
[95]	1, 2, 4L	330°C	-	60 mins	Air	MoO_3-AFM & MFM
[150]	1-10L+	345°C	-	120 mins	Air	None-Raman
[148]	1-4L, >40nm	320°C	200°C	120 mins	Ar/O_2	MoO_3-Raman[2]
[157]	CVD, 1-3L	240°C	-	90-120 mins	O_2	-

Table 3.1: Key figures from the literature concerning the oxidation of MoS_2.

atom in the preceding layer and vice versa. This means that the ZZ-Mo and ZZ-S_2 directions should be reversed in two neighbouring regions with a layer number difference of one [150]. Therefore, pits are expected to be in opposing orientations on adjacent regions with a layer number difference of one. This is experimentally demonstrated in the supplementary information of Zhou et al. and also in the work of Yamamoto et al. and Gan et al. [148, 150, 161]. Several of the key papers discussed here are summarised in table 3.1.

Another question of particular interest in the field of fabrication and patterning concerns the ability to selectively activate material spatially for reaction. However, oxidation studies to date have demonstrated little or no ability to confine the reaction spatially, an important requirement for scaling this process to applications. In chapter 7, localisation of the oxidation reaction to arbitrary regions of MoS_2 is demonstrated. Unprecedented spatial control of the reaction by pre-treating with an ion beam is demonstrated, and several aspects of the reaction are clarified e.g. the presence of molybdenum oxide (MoO_x), the effects of temperature and time, and the influence of ion dose.

To summarise this section, oxidation of few layer MoS_2 in controlled oxidising environments can be used to thin and etch the material. Some samples have been reported to be etched with an extremely high density of pits, creating a mesh feature. When etched, removed regions tend to be triangular in shape and the best available evidence suggests that the ZZ-Mo edge bounds these pits. The behaviour of the

[2] Only found for much thicker samples and higher temperatures, > 400°C. Thin samples were etched before this temperature with no detection of MoO_3 in Raman Spectroscopy.

resultant MoO_x species is unclear, with some evidence that they may not fully sublime for some reaction conditions. In particular, the change in doping state suggests the continued presence of oxide species, even if only in small quantities which are undetectable in Raman spectroscopy. The oxidative etching of MoS_2 is initiated at edges and intrinsic defect sites. Since ion beam-induced defects can be very highly confined spatially, it is now intended to activate desired regions for oxidative etching using an ion beam. To date, no reports of spatially moderating the reaction have been reported which will be demonstrated in chapter 7.

Chapter 4

Analysis Methodology

In chapter 3, the modification methods used in this work were introduced. Whether by highly focused ion beam, ion activated gas or ion moderated chemical reaction, the modification of 2D materials performed by these methods must be quantified accurately and reproducibly. In this chapter, the characterisation methods used for quantification and analysis will be introduced. These include Raman spectroscopy, a non-destructive and high throughput method for characterising the structure of materials. A thorough discussion of the Raman spectra of both graphene and MoS_2 will be provided as well as models relating these spectra to defects in the materials. PL spectroscopy is often performed concurrently with Raman spectroscopy for the characterisation of optical and electronic properties and this method will be introduced. Next, several microscopy techniques will be discussed including SEM and TEM, high resolution imaging methods, which also allow in situ measurements such as EDX.

4.1 Raman Spectroscopy

Raman scattering is an inelastic phenomenon involving the exchange of energy between an incident photon and the vibrational modes of a material. These phonons arise from thermally excited and kinetically active species in the material. Optical phonons are relatively high in energy and arise from out of phase vibrations between neighboring atoms within the unit cell. In phase vibrations give rise to acoustic

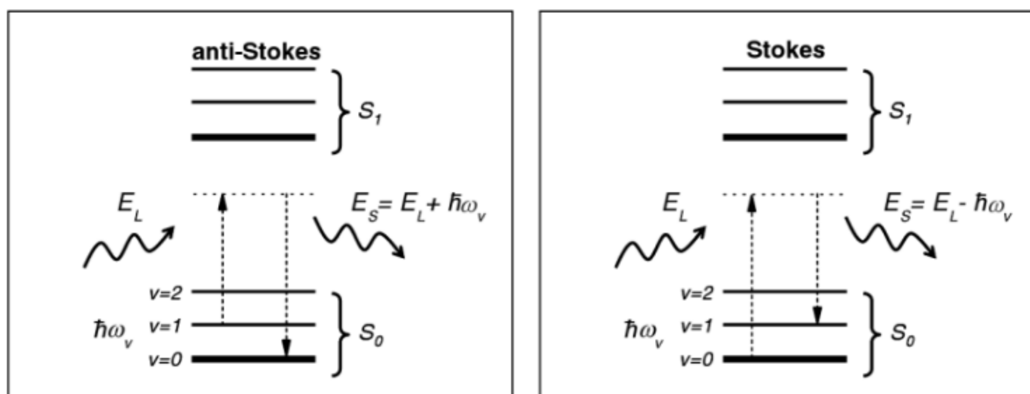

Figure 4.1: Jablonski diagram illustrating Stokes and anti-Stokes shifts [164].

phonons with high wavelength although these are usually considered only in ordered materials rather than in molecules or amorphous material. In practice, conventional Raman spectroscopy is used predominantly for optical phonon measurements as the acoustic phonons are usually very low in energy. However, in the case of nanomaterials, confinement can lead to high energy acoustic modes, detectable in conventional Raman [162]. Both optical and acoustic phonons may be longitudinal or transverse giving rise to polarisation effects in Raman spectroscopy (many peaks are preferentially excited by or cannot be excited by p or s type lasers) [99, 163]. After scattering, the new photon will have a frequency equal to the sum or difference (a consequence of a Stokes or anti-Stokes shift) of the frequencies of the incident photon and the frequency of the vibrational mode interacted with, illustrated in figure 4.1.

Group theory is a study of symmetry which uses algebraic structures (groups) to label molecular and solid state configurations [165]. Character tables provide the result, type and number of symmetry operations for specific symmetry species. In vibrational spectroscopies, each mode of vibration in a species is represented in the character table. Only those vibrational motions with the symmetry properties described in the character table are allowed. The complete set of normal vibrational modes of a molecule will belong to one of the following three categories: Raman active, infrared active, or silent [163]. There are fundamental differences between Raman and IR active modes such that there is a rule of mutual exclusion between

their excitation. It is found that for simple molecules (possessing a centre of symmetry), vibrational modes can be Raman or IR active but not both (they can still be neither). This does not hold for more complex molecules without a centre of symmetry such as proteins where modes can be active in both. For a transition to be Raman active there must be a change in the polarisability of the molecule during the vibration (i.e. it must be polarisable). It has been observed that molecules with a strong dipole moment are typically hard to polarize. Group theory allows the prediction of Raman and IR active modes in molecules and crystals such as fullerene and MoS_2 [166, 167]. In practice, Raman spectroscopy is a scattering method (a grating is used to disperse the emitted photons based on their energy) whereas IR spectroscopy is an absorption method where the transmitted photons are detected.

In Raman spectroscopy, a monochromatic light source (laser) is used to excite the specimen, and emitted photons are collected with a lens. A grating is used to separate photons for collection based on their energies. A spectrum is thus produced which is a measure of the Raman shift. A typical Raman spectroscopy tool is limited in resolution by diffraction, meaning that signal is typically collected over a range of about 1 μm in the sample. This technique benefits from a high throughput and a typically low capacity for specimen destruction.

Since the detected vibrational modes arise from molecular vibrations, they might be expected to possess well defined intervals in their energy levels in accordance with quantum theory, represented by perfectly sharp peaks in the Raman spectrum. However, such peaks are affected by the environment of the vibrational modes including factors such as proximity to and density of defects, species adsorbed to the surface, strain, doping state, temperature etc. The observed shape in a spectrum is the sum of the vibrational modes, all of which are affected by their environment. In practice, functions must be fitted to peaks to account for this variation over the collection region and overlapping peaks often need to be separated.

An additional application of Raman spectroscopy besides characterising defects, strain etc. in the context of 2D materials is the identification of different layer numbers, for example graphene [26, 65] and MoS_2 [11, 28]. Changes in layer number can also give rise to previously inactive vibrational modes such as the shear mode (SM) and layer breathing mode (LBM) which occur only in multilayer MoS_2 [108,

168]. Similarly, changes in defect density can give rise to defect-activated peaks such as the *D* peak in graphene and *LA*(*M*) peak in MoS_2 which cannot be detected in the pristine monolayer forms of those materials. full width at half maximums (FWHMs), intensity ratios and peak positions of peaks can all be changed by ion irradiation since it is expected to influence many characteristics of the subject 2D material including local strain, inter-defect distance and thickness. This makes Raman spectroscopy an invaluable tool in this work.

Fitting to the peaks in a Raman spectrum usually involves a Gaussian distribution (typical in solid materials, features a curving centre and abrupt tails) or a Lorentzian distribution (typical in fluid materials due to dephasing, features a sharper centre and longer tails). Examples of these distributions are shown in figure 4.2(a). The key figures of merit for a vibrational mode in a material are thus the FWHM, centre (i.e. position) and height (i.e. intensity). There are many ways in which the quality, environment etc., of a material can affect these characteristics of its Raman peaks. For instance, narrower peaks typically correlate with better crystal structure [169].

Raman spectra may also contain signals due to fluorescence where vibrational transitions are coupled with an electronic transition. Since the peaks from a fluorescence signal are very wide on a Raman spectrum, removal of this signal through background subtraction or curve fitting is a necessary but also very simple process (shown in figure 4.2(b)), possible in many software packages [171, 172]. Fluorescence is common in the spectra of electron and ion-irradiated materials because of beam-induced deposition (BID) of amorphous carbon.

Raman spectroscopy was carried out on graphene with a *Horiba Jobin-Yvon LabRAM-HR* (λ_L=633 nm) laser with a 1200 lines/mm diffraction grating and a 100× objective aperture (NA=0.66). There is a small artifact peak at ~2330 cm^{-1} apparent in the spectra corresponding to the N_2 molecule in the environment. These spectra were acquired from a single point for each irradiated region. 10 acquisitions, each of 1s were made and averaged.

For MoS_2, Raman spectroscopy was performed with a *WITec alpha 300R* tool with a laser wavelength of 532 nm, a 100× objective (NA=0.95) and a 1800 lines/mm diffraction grating. These spectra were acquired from the desired region by averaging the relevant area of an acquired Raman map with a spectrum at each point [173].

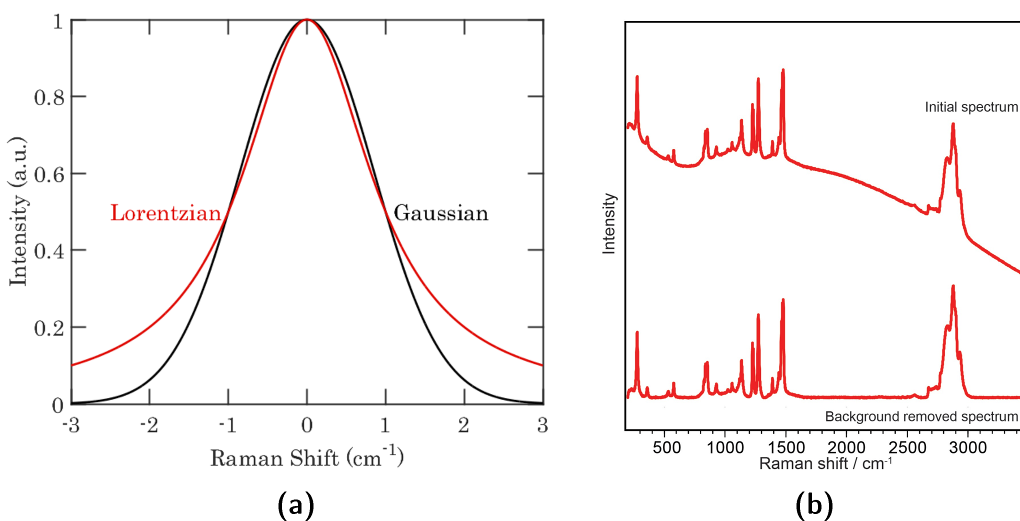

Figure 4.2: Data treatment in Raman spectroscopy. (a) shows both Lorentzian (red) and Gaussian (black) distributions with the same height, centre and FWHM. (b) shows a sample Raman spectrum as initially acquired and after the removal of the broad fluorescence background. The remaining spectrum is flat in the absence of local peaks and is easily analysed by fitting peaks to it [170].

Maps were generated by taking four spectra per μm in both x and y directions over large areas.

For both materials, the laser power was around 1 mW or less to minimise damage to the samples and the laser spot size was ~0.7 μm for the *Horiba Jobin-Yvon* and ~0.3 μm for the *WITec alpha 300R*.

4.2 Low Frequency Raman Spectroscopy of MoS_2

In Raman spectroscopy, the <50 cm^{-1} regime is often referred to as the low frequency/wavenumber part of the spectrum [168]. Typical Raman spectrometers cannot detect these energies without a specialised filter because they are very close to the Rayleigh line. 2D materials exhibit vibrational modes in this low frequency regime due to interlayer vibrations. The interlayer SM and LBM in MoS_2 are prime examples of this. The SM is composed of the in-plane motion of metal and chalcogen atoms, while the LBM involves the out-of-plane motion of metal and chalcogen atoms, illustrated in figure 4.3 [83, 174]. It must be noted that these peaks do not occur in monolayers since there can be no interlayer vibrations.

Owing to the relative difficulty in obtaining spectral data in the low-frequency region, low-frequency Raman spectroscopy has been the focus of just a few studies thus far. With increasing opportunities for preparing heterostructures with different layered TMDs, the low-frequency modes are very useful for directly measuring interlayer coupling in 2D materials [175]. Recent studies have shown the appearance of a new LBM and suppression of the SM in stacked MoS_2/molybdenum diselenide ($MoSe_2$) and MoS_2/tungsten diselenide (WSe_2) heterostructures whose frequency decreases with increasing stacking mismatch angle [175, 176]. Investigation of the low-frequency SM and LBM has been suggested as a far more powerful and versatile method of determining layer number in TMD materials than conventional Raman spectroscopy as shown in figure 4.3 [108, 111, 168, 177]. Mapping these modes gives a very clear picture of layer numbers present in MoS_2. Zhang et al. found that twisting significantly alters the interlayer stacking and coupling, leading to notable frequency and intensity changes of the low-frequency modes [111]. In contrast to the low-frequency interlayer modes, high-frequency intra-layer Raman modes are much

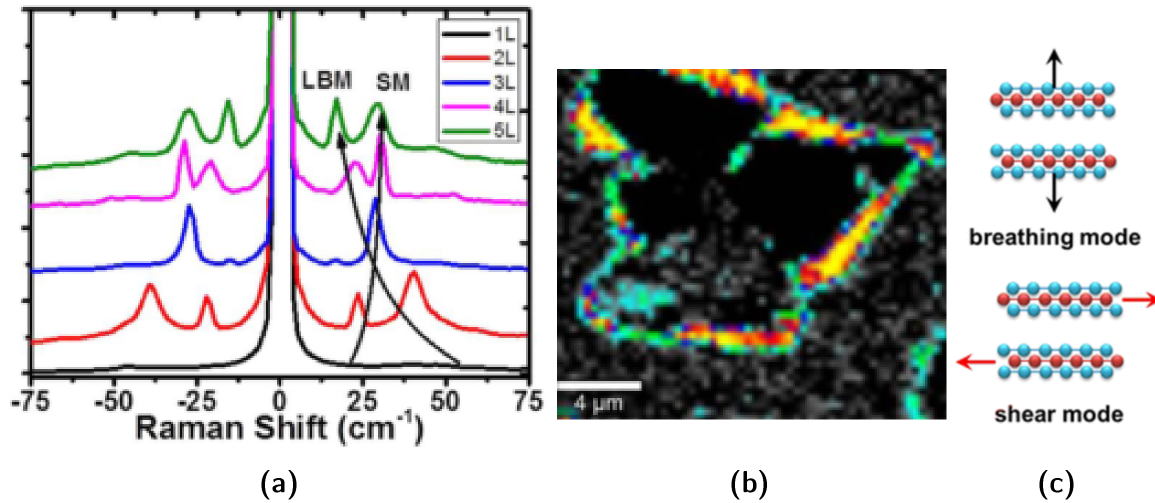

Figure 4.3: Low frequency Raman spectrum and peak intensity map of the layer breathing mode of 2L MoS_2. (a) Low frequency Raman spectra for several different layer numbers in MoS_2. (b) Peak intensity map of the LBM for 2L MoS_2 at ~40 cm^{-1} [168]. (c) Graphic showing the direction of vibration for the LBM and SM respectively.

less sensitive to interlayer stacking and coupling [111].

For the purpose of measuring these modes, a special low energy filter (rayshield coupler) was employed on the above-mentioned *WITec alpha 300R* tool so that the low frequency Raman modes could be observed clearly [168].

4.3 Photoluminescence Spectroscopy

Luminescence is the emission of visible light caused by the relaxation of an electron from an excited state to a ground state. Photoluminescence occurs in the case where the electron is excited by incident light of energy larger than the material's band gap. This absorption creates an electron-hole pair in the conduction and valence bands respectively. When energy and momentum relaxation occurs, the electron and hole recombine with the emission of a photon.

Although the fundamental interaction is very different to that of Raman, both analytical methods share a typically non-destructive interaction in which the speci-

men is illuminated with monochromatic light. PL is extremely useful in the analysis of 2D materials including MoS_2 and WS_2 because of its dependence on crystal structure/quality and layer number [178, 179]. In this thesis, PL spectra were acquired using the instrument also mentioned above for Raman spectroscopy, the *WITec alpha 300R*. A 532 nm excitation laser with a power of <1 mW was used in order to minimise sample damage. A spectral grating with 600 lines/mm was used for PL measurements. Maps were generated in the same way as for Raman.

4.4 Microscopy and Resolution

The highest useful magnification in any microscope is constrained by its resolution limit. If the resolution of a microscope is limited by the diffraction of its probe particle (i.e. photons, electrons, ions) then it is said to be diffraction-limited. The process of resolving two adjacent features is therefore constrained when the first diffraction minimum of the image of one source point coincides with the maximum of another. This is a restriction which is better known as the Rayleigh criterion which can be mathematically stated thus: [180]

$$r = \frac{0.61\lambda}{n\sin(\theta)} \tag{4.1}$$

where r is the minimum resolvable distance between two objects, λ is the wavelength of the probe, n is the index of refraction of the media surrounding the two points and θ is the half-angle between the optical axis and the furthest light that exits the lens. In approximate terms, this means that the resolution limit is about one half to one third of the wavelength of the imaging particle. Thus the best achievable resolution in a conventional OM is approximately 200 nm (depending on the lens quality).

4.5 Scanning Electron Microscope

The most widely used category of electron microscope is the SEM. The principles behind it are broadly similar to those of the GIM. In SEM, electrons are provided by the electron gun and a beam is conditioned by a system of electromagnetic condenser

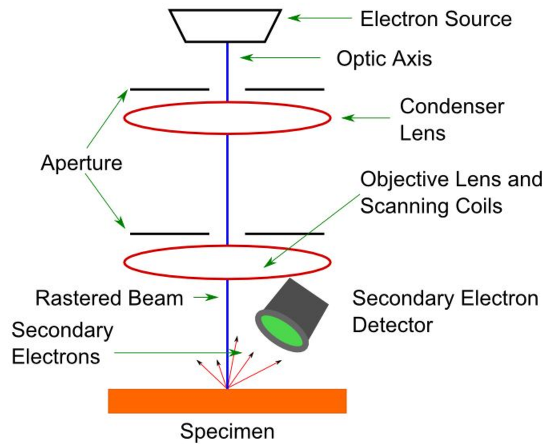

Figure 4.4: Outline of a scanning electron microscope

lenses and apertures in the electron column. At the bottom of the column, deflection coils allow the periodic scanning of the beam and the objective lens focuses the beam to a sharp probe. The specimen is thus investigated by a finely focused and rastered beam of electrons (see figure 4.4).

Secondary electron (SE) or through the lens (TTL) detectors are among the most commonly used to collect signals from each pixel in the rastered pattern although other detectors of various types are available [181, 182]. The attainable image resolution greatly surpasses that of OM since it is not limited in practice by diffraction. This is because of the short wavelength of the high energy electrons (of the order of pm at an energy of 30 keV). Resolution of high end SEMs now approaches 0.5 nm [182]. In addition, a host of other analytical techniques are available in many SEMs including: cathodoluminescence spectroscopy (CLS), EDX, secondary electron spectroscopy (SES) and more.

The most common detectors used in both GIM and SEM involve the collection of electrons which emerge from the specimen. When primary beam electrons backscatter from within the sample they are labelled backscattered electrons (BSE). Secondary electrons are generated by inelastic scattering on the atomic core or on the electrons of the atomic shells of the sample material [182]. SEs are low energy electrons (<50 eV) which are typically divided into categories labelled type 1 (SE_1),

type 2 (SE_2) and type 3 (SE_3) [181]. SEs generated by the incident beam are designated SE_1. Since SE_1s are generated in extreme proximity to the incidence of the primary beam, they convey very high resolution information [181, 182]. SE_2s are produced by plural scattering such as by BSEs which excite the sample electrons on their way back to the surface. Since SE_2 signal strength depends on the amount of BSEs generated they contain information about the volume from which the BSEs originate, a volume which is typically much larger than the range from which SE_1s are produced. After leaving the sample and if not intercepted by a detector, stray BSEs can also generate SE_3s which are emitted from the interior surfaces of the specimen chamber and therefore do not contain any useful information.

The TTL or inLens detector in many modern SEMs is positioned above the objective lens and detects directly in the reversed beam path. The SE electrons are re-accelerated and focused through an electromagnetic field to the detector where they hit a scintillator. The information is multiplied in a photomultiplier and then output as a signal which is then electronically utilised. This detector is optimised for the collection of SE_1s meaning that it produces highly resolved images. The topographic information is not typically dominant due to the top-down viewing angle. However, since the SE_1s signal is highly surface dependent, this is typically the superior choice of detector for most applications involving 2D materials.

The Everhart-Thornley (ET) or SE_2 detector is common to both the SEM and GIM. It is mounted outside the pole piece and therefore views the specimen at an angle to the incident beam. For this reason, it provides a great deal of topographic contrast such as with surfaces angled towards the detector appearing brighter and other shadowing effects. A biased collector grid surrounds the detector to attract electrons and enhance the signal. The bias can usually be changed to reduce the detection of SEs although the higher energy BSE signal is not altered. Electrons moving to the detector are absorbed, accelerated and directed to a scintillator. Flashes are directed through a lightguide and transferred to a photomultiplier and hence converted to electronic signal. Compared to the TTL detector, it receives many BSEs which provides a great deal of material contrast because of the dependence of BSE production on atomic mass.

Since SE_1s possess a lower average energy than SE_2s it has been suggested that

the collector cage of many ET detectors acts to filter out this SE_1 signal by trapping the low energy component on the wires of the cage [183]. Since the TTL detector is comparatively very dependent on low energy SE_1s, images it produces are thus highly sensitive to the specimen work function.

Two models of field emission SEM were used in this work a *Zeiss Supra* and a *Zeiss Ultra*, both manufactured by *Zeiss Microscopy GmbH*, Jena, Germany. Both are essentially identical in typical operation and equipped with SE and TTL detectors. Both also employ a *Gemini* column allowing high performance operation at energies from 30 keV down to even below 1 keV. The *Zeiss Ultra* was also equipped with a transmission mode scanning electron microscopy (TMSEM) detector mentioned in appendix A. The highest pressure at which SEM was performed was 2×10^{-5} mbar although typically the vacuum reached 1×10^{-6} mbar.

4.6 Transmission and Scanning Transmission Electron Microscopy

With a far greater resolving power, TEM and STEM are used in this work to provide images of the highest resolution. Both use a beam of electrons with typical energies far higher than those used in scanning electron microscope (SEM) (60-300 keV in typical modern tools). The beam must pass through a sufficiently thin specimen, fortunately not difficult in the case of 2D materials. In TEM, the electrons travel in a parallel beam and in STEM the beam is convergent on the plane of the specimen. An illustrative outline of both systems is provided in figure 4.5.

The formation of images from TEM is built upon complex contrast mechanisms including mass-thickness contrast, diffraction contrast and phase contrast. Amongst the specimen related variables affecting the contrast in an image are the atomic mass, crystal structure and thickness. Some of the instrument related variables include the defocus, selection of objective aperture and angle with respect to the specimen. A high resolution image of a crystalline material depends heavily on phase contrast such that the resulting image will have a great degree of periodicity in it. A calculation called a fast Fourier transform (FFT) can be performed which creates a

representation of the crystal in reciprocal space. The FFT of an image is essentially analogous to the electron diffraction pattern in that the central spot corresponds to the direct beam and the surrounding spots represent diffracted beams. As such, the intensity ratio of the central spot to one of the diffraction spots can be used as a measure of crystallinity in that a lower value corresponds to better crystallinity [184].

In STEM the electron beam is focused into a convergent probe which is focused at the plane of the sample and rastered in a rectangular pattern much like in GIM and SEM. The contrast mechanism of STEM is much more straightforward for interpretation being dependent only on thickness and mass. Electrons are deflected by elastic nuclear interactions (Z dependent) to high angles. A HAADF detector is commonly used which can resolve the atomic structure of a sample in an easily interpretable image. A column of atoms produces an intensity which (in a thin specimen) is directly proportional to the number of atoms in the column [184].

The TEM and STEM reported in this thesis was all performed using an *FEI Titan 60-300*.

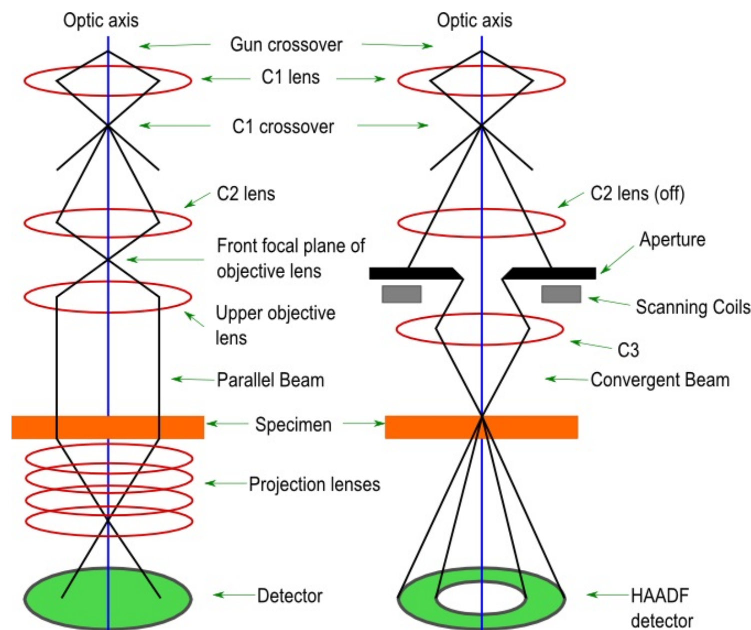

Figure 4.5: Outline of a transmission electron microscope (left) and a scanning transmission electron microscope (right) [184].

4.7 Energy Dispersive X-ray Spectroscopy

Chemical analysis is possible in many types of electron microscopes. There is a wide variety of methods including CLS, EDX and electron energy loss spectroscopy (EELS). In this work, EDX was very useful to measuring stoichiometric changes in MoS_2. This analysis was performed primarily in the above-mentioned *FEI Titan 60-300*. During electron beam irradiation of a sample, core electrons are excited to unfilled higher energy levels. In relaxing to their ground state, these electrons emit X-ray photons of an energy which is characteristic of the atomic species. Many of these photons within the microscope chamber reach a semiconductor based detector where the X-ray energy is converted to a voltage signal. Processing of the acquired spectra can provide very localised stoichiometric information. The EDX reported in this thesis was all performed in the *FEI Titan 60-300* stimulated by an electron beam of energy 300 keV.

Chapter 5

Modifying Graphene by Charged Particle Beams

IN this chapter, two methods will be demonstrated for the precise modification of graphene. A focused, low-energy (5 keV) electron beam was used to locally activate etching of a graphene surface in a low pressure (0.3 Pa) N_2 environment. To date there has been a basic understanding of the etching mechanism. However, to enable it as a widespread technique a more fundamental model is required. In this work the etching was systematically investigated as a function of the different parameters which could be controlled, i.e. beam dwell time, nitrogen gas pressure, beam current and sample temperature. The method allows the flexible and efficient fabrication of nanopores with sub 5 nm diameters. Nanopore growth rates were investigated systematically. The effects of nitrogen pressure, electron beam dwell time and beam current were characterised in order to understand the etching mechanism and enable optimisation of the etching parameters. A diffusion-based model is suggested to describe the spread of ionised nitrogen which determines the nanopore growth rate. In addition, the application of this technique to other material systems is both desirable and instructive. Etching of other 2D materials was attempted as demonstrated with MoS_2. The lack of etching observed supports a model of a chemical reaction-based mechanism. The understanding of the etching mechanism will allow more materials to be etched by selection of an appropriate ion species.

The second method discussed in this chapter uses high energy ion species for

the defect engineering of graphene. In chapter 2, the model developed by Lucchese et al. was described in detail which relates the inter-defect distance, defect size and several other variables to the ratio of the intensity of the D and G peaks in Raman spectra. In graphene, the defect yield and the nature of defects introduced by He^+ and Ne^+ species at 30 keV are inferred from Raman spectra using established models [26, 27, 71]. While a comparison of defect sizes introduced by energetic noble gas ions in graphene has been performed using molecular dynamics, this is (to the authors' knowledge), the first experimental comparison for graphene. It is also one of very few reports to distinguish between supported and freestanding graphene since the measured properties are highly influenced not only by quality, but also by environment [185, 186]. The effect of the environment on the fabrication process must also be quantified [113].

5.1 Electron Beam-Induced Nitrogen Etching

A graphene sample was prepared by collaborators (A. O'Neill, J.N. Coleman, TCD) by sonicating pristine graphite in isopropanol for 48 h. After sonication, the sample was centrifuged at 2,000 rotations per minute (RPM) for 45 min to remove large pieces of graphite that did not fully exfoliate. The resulting supernatant was decanted and retained for further use. The dispersion quality was previously reported by O'Neill et al. [56], with flakes typically 1 μm in length and with thicknesses of less than ten layers, as confirmed by AFM and Raman mapping. MoS_2 flakes were also produced by the same collaborators using a similar method, MoS_2 powder was sonicated in N-methyl-pyrrolidone (NMP) as described by O'Neill et al. [187]. The dispersions were dropped onto a lacey carbon TEM grid and allowed to dry naturally in air.

For the etching rate experiment (figure 5.4) graphene flakes of a known thickness were required. These samples were prepared by Dr. Yangbo Zhou by micromechanical exfoliation onto a 300 nm SiO_2 layer on a Si substrate. Flake thickness was confirmed by optical contrast [188]. An optical image of the flakes before transfer can be found in appendix B. The flakes were then stamp transferred to a holey carbon film on a TEM grid. The transfer process is described in detail in [189]. In

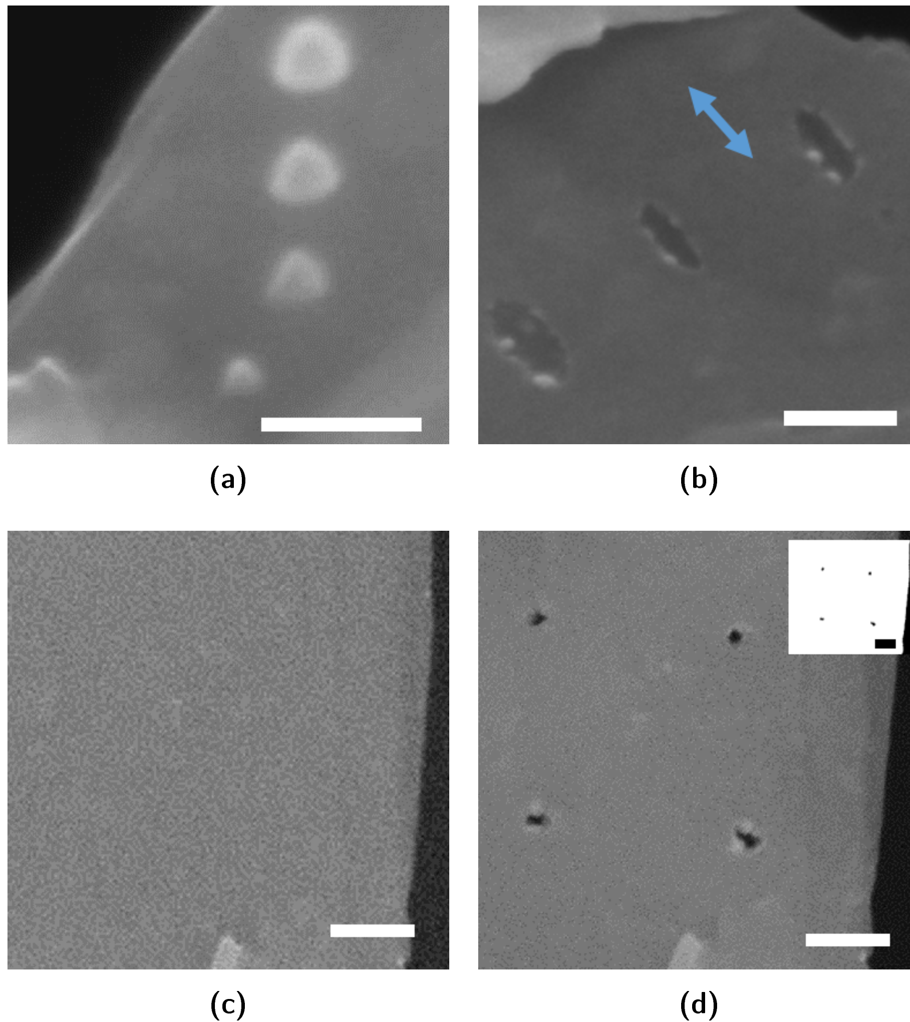

Figure 5.1: SEM images of electron irradiated graphene with and without nitrogen gas. (a) Four spots of beam deposited carbon before the nitrogen gas was introduced, each produced with different beam dwell times (beam energy 5 keV). (b) Three partially etched regions. The arrow indicates the direction of elongation of the features. (c) SEM of a graphene flake before etching. (d) Four holes etched into the flake from (c). Inset is the binary image used to measure the pore sizes. Scale bars are 100 nm.

each etching experiment the electron beam was focused onto a spot of ~5 nm on the surface of the graphene flake. A nitrogen flux was delivered directly to the region of the beam-sample interaction through a nozzle. The flux was adjusted by monitoring the gas pressure in the SEM chamber. The varied parameters were nitrogen pressure, electron beam dwell time, beam current, and sample temperature. The etching of the graphene was studied by measuring the area of material removed from each exposed region after the experiment. This etched area was calculated by taking an image of the flake in the SEM and converting it to binary, i.e. black and white, using imagej [190]. A histogram of the area was then used to find the size of the holes etched in the material (see appendix B). TEM imaging was performed in an *FEI Titan 60-300* operating at 300 kV with a low (<1 nA) beam current.

SEM images of typical freestanding flakes of few layer graphene (FLG) (typically less than three layers) are shown in figure 5.1. For a 5 keV beam with a beam current of 50 pA, deposition of carbon contamination was observed to occur before introducing nitrogen gas into the chamber. The contamination appeared as bright circular features in figure 5.1(a), four of which (each created with different beam dwell times) are shown. The contamination grew in size as the dwell time increased. The nitrogen gas flow was then turned on. Partial etching of three areas on a thick flake (>10 layers) is shown in figure 5.1(b) with a beam dwell time of 180 s at each point. The elongated shape of the etched areas indicates sample drifting, which is typically approximately 0.2 nm/s in these experiments. This shape was observed because the rate of etching was not high enough to etch through all of the layers of the sample before the area drifted out of the region of the beam probe. This is typical of thicker flakes (>10 layers). Fabrication of the smallest pore sizes requires either a thinner sample or a higher etching rate be used, or both. FLG flakes were selected for the etching experiments; they were identified using TMSEM. Figure 5.1(c) shows one such flake before etching. Four different pores were successfully etched through the flake, as shown in figure 5.1(d). There is some variation in the pore shapes, most likely due to the profile of the beam not being perfectly round and minor surface contamination variations. The average pore size is 14 nm ± 1 nm (measured from the inset binary image) showing the high level of pore size reproducibility achievable by this method.

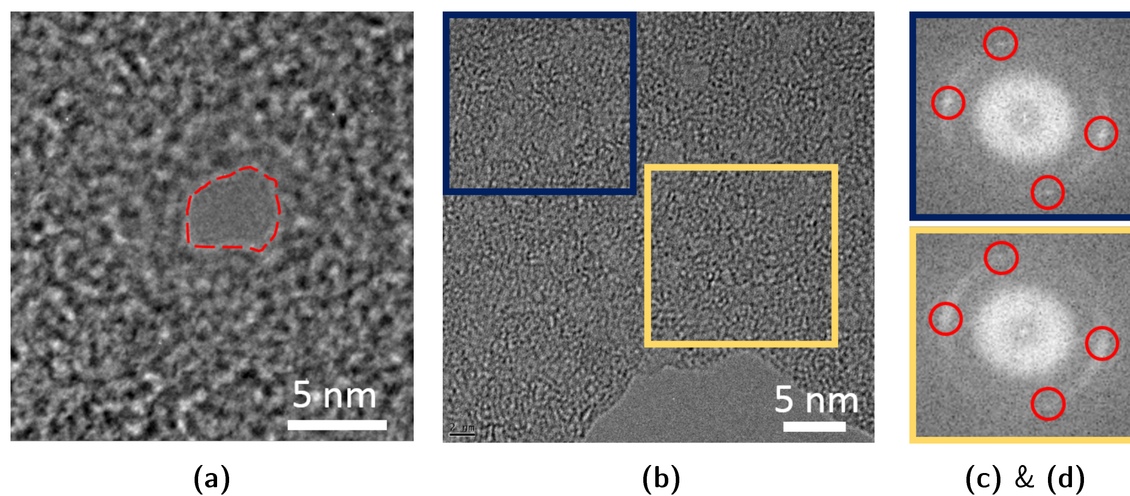

Figure 5.2: TEM images of electron beam-assisted nitrogen etched graphene. (a) TEM image of an etched pore with an average diameter of just 4.5 nm. (b) TEM image of the area beside an etched nanopore. (c) The FFT of the top left area in the blue box in (b). The spots showing the good crystal structure are circled. (d) The FFT of the bottom right area in the yellow box in (b). The spots were not observed in this image.

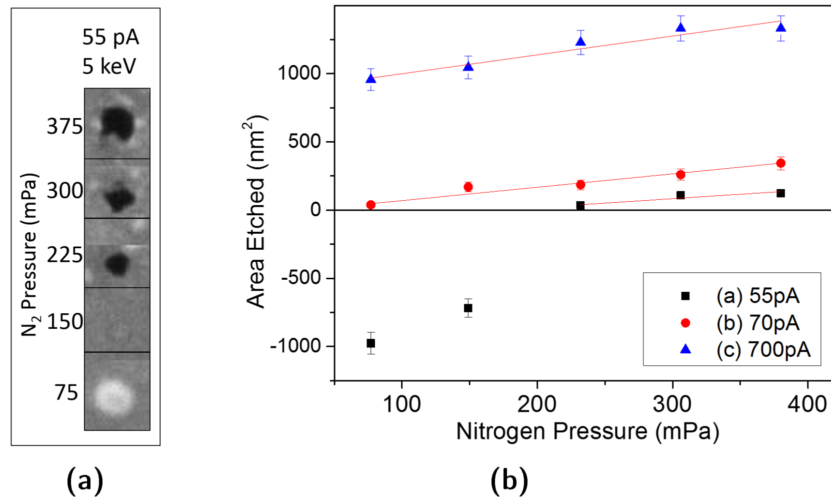

Figure 5.3: Etching and deposition rates as a function of beam current. (a) An example of the deposition and etching observed at 55 pA beam current is shown. (b) At the lowest beam current (55pA, black squares) hydrocarbon contamination was initially observed. Upon increasing the nitrogen gas pressure the deposition was observed to be suppressed and etching then began to dominate. The etching rate was observed to be increased at higher beam currents of 70 pA and 700 pA. In all cases the rate of etching grows with higher gas pressure.

Figure 5.2(a) shows an example of one of the smaller pores which can be etched; this pore has an average diameter of 4.5 nm as measured from the TEM image. Pores of this size can be etched in FLG within a few hundred milliseconds (5 keV e-beam energy, 150 pA e-beam current, 300 mPa N_2 pressure). This is an order of magnitude faster than the TEM for similar pore sizes [191, 192]. Figure 5.2(b) is a high resolution TEM image of the region beside an etched pore. The edge of the pore can be seen at the bottom of the image. Annealing could be used to recover the crystal structure at the pore edge if required. In TEM nanopore milling damage is usually seen at the pore edge. In situ annealing has been used to recover the graphene structure after irradiation [192]. The crystal structure surrounding He^+ fabricated nanopores has not yet been assessed.

Investigation of the effect of the various etching parameters is required both to control and optimise the etching rate, and to understand the mechanism by which

the etching occurs. The effect of the nitrogen gas on the etching was assessed by varying the pressure of the nitrogen gas in the system. The e-beam dwell time was set to 30 s. The dwell time refers to how long the electron beam probe was left focused on a single spot on the sample. Five adjacent regions on the same flake were irradiated at different gas pressures. Images to show the effect of the exposure at 55 pA beam current are shown in figure 5.3(a) with the lowest gas pressure at the bottom. In figure 5.3(b), with a fixed beam current of 55 pA (black squares), effective etching only occurred when the nitrogen pressure was higher than ~200 mPa. Hydrocarbon contamination was observed at lower pressure settings. The deposition is expressed as a negative etching rate in figure 5.3(b). The increasing nitrogen pressure was observed to suppress hydrocarbon contamination and enhance etching. The experiment was then repeated with larger beam currents. At a beam current of 70 pA (red circles in figure 5.3(b)) deposition of contamination at low nitrogen pressure was not observed. At 700 pA (blue triangles) etching was again observed to occur, but at a faster rate. In all cases the etching rate was observed to increase with increasing nitrogen pressure. It was found that the etching rate was linearly dependent on the nitrogen pressure within the experiments. For the following experiments the nitrogen pressure was fixed to approximately 300 mPa.

The beam dwell time effect was studied by observing the amount of material etched for a range of dwell times. A fixed nitrogen pressure (~300 mPa) and beam current (~180 pA) were used. The experiment was conducted on two flakes, a single layer and a ten layer thick flake. An image of the etched flakes can be found in appendix B. As shown in figure 5.4, the etched areas of the two flakes both increased as the dwell time was increased until eventually reaching saturation. However, the area etched for a given time is different for the one layer and ten layer thick samples. This difference can be attributed to the different thicknesses of the flakes used and it indicates that the number of layers in the flake had an effect on the etching rate. The ten layer thick sample required longer to etch than the single layer sample. The data, of sigmoidal shape, was found to be well fitted with the error function as shown in figure 5.4. This was chosen since nitrogen, excited by the electron beam, is expected to propagate with diffusion characteristics. Diffusion equations dictate that there is an exponential decay in the concentration of ionised nitrogen molecules with

increasing distance from the electron beam. This mechanism would therefore cause the pore growth rate in a line to decrease exponentially with increasing distance from the beam. This is due to a reduced availability of the etching species (nitrogen ions) with increasing distance from the source (electron beam). This becomes analogous to diffusion with time in one dimension which is solved by the complementary error function.

The effect of the beam current on the etching rate was investigated. Initially at a very low beam current range, 10 pA - 40 pA, figure 5.5(a) the deposition of contamination was observed, graphed as negative etched area. When the beam current continued to be increased etching was seen to dominate. The etching rate then increased as the beam current continued to be raised. In figure 5.5(b) a further increase was observed in the etching rate with larger beam currents (~300 pA).

From these results it was observed that deposition of carbon based contamination is always a competing process to the etching. This deposition can be overcome with a sufficiently high etching rate. The etching rate can be increased by raising the pressure of the etching gas, by increasing the electron beam current, by reducing the thickness of the sample, or by reducing the electron beam energy (with a trade-off in electron beam size) as shown previously [143]. Once etching has begun, the area of the nanopore will grow with time. The pore growth rate will be observed to decay exponentially. This is due to the diffusion of the ionised nitrogen molecules. The nitrogen is directly ionised by the electron beam. The electron beam has a diameter of ~5 nm. We investigate pores with a diameter larger than this value to eliminate the effect of direct electron beam interaction with the sample. In this regime the nitrogen ions diffuse from the electron probe and interact with the reactive dangling bonds of the carbon atoms at the nanopore edge [193].

The nanopore growth rate observed in figure 5.4 clearly exhibits exponential decay, to be expected from a diffusion model. An investigation into the temperature dependence of the etching rate was undertaken. A stage with greater stability and a greater range of temperature control is required for a more complete investigation. We were limited to a sample drifting rate of ~80 nm/s and a temperature range of -25 to 50°C. With these limitations we were not able to determine the effect of temperature on the etching rate in a quantitative manner. The results can be found

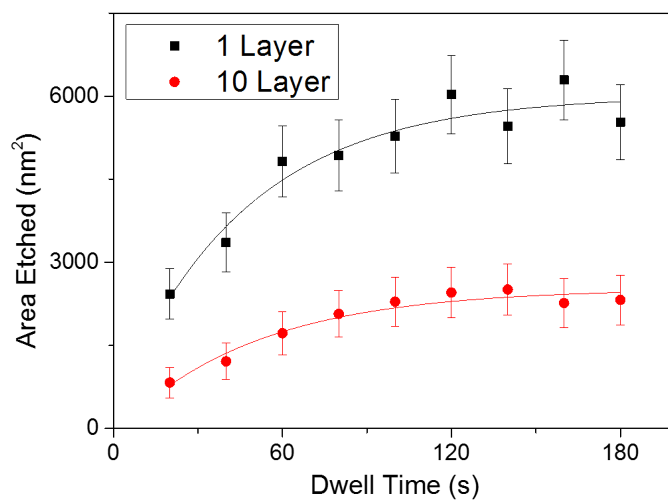

Figure 5.4: The area of graphene etched as a function of electron beam dwell time. A longer etching time leads to a larger pore, until a saturated value is reached. A large difference in etching rates was observed for different thicknesses. The ten layer sample has a lower etching rate than the single layer sample. The data was fitted with the error function.

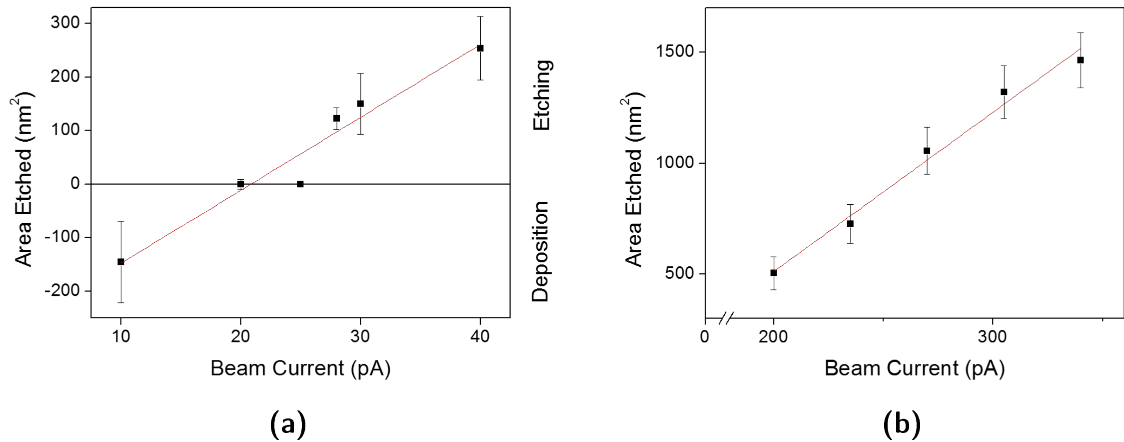

Figure 5.5: Nitrogen etching rate as a function of beam current (a) The transition from deposition to etching at higher beam current is observed. (b) A higher rate of etching occurs with increasing beam current.

in appendix B.

The nitrogen gas-assisted electron beam etching technique was developed using graphene. This technique would have a much broader appeal if it could be applied to a range of materials. Therefore, etching of a few-layer flake of MoS_2 was attempted. Figure 5.6 shows a flake of MoS_2 after an attempt at etching. The electron beam was focused on a point within the red box. The beam energy was 5 keV, the beam current was 150 pA, the nitrogen gas pressure was 380 mPa, and a significant dwell time of 300 s was used. No observable etching occurred. This result was attributed to two factors. Firstly, each layer of MoS_2 is three atoms thick, unlike the single atom thick graphene. As was observed earlier, the thickness of a sample substantially affects the rate of etching. Secondly, the MoS_2 sample consists, in part, of a heavy metallic element which does not react with nitrogen to become a gaseous species which evaporates from the sample. This result indicates that the selection of an appropriate etching gas is essential for producing the necessary etching reaction. For MoS_2, xenon difluouride (XeF_2) has been shown to be an effective etching gas [194]. It must be determined if a gaseous product exists when assessing the applicability of this etching technique to new materials. It was also found that contamination was

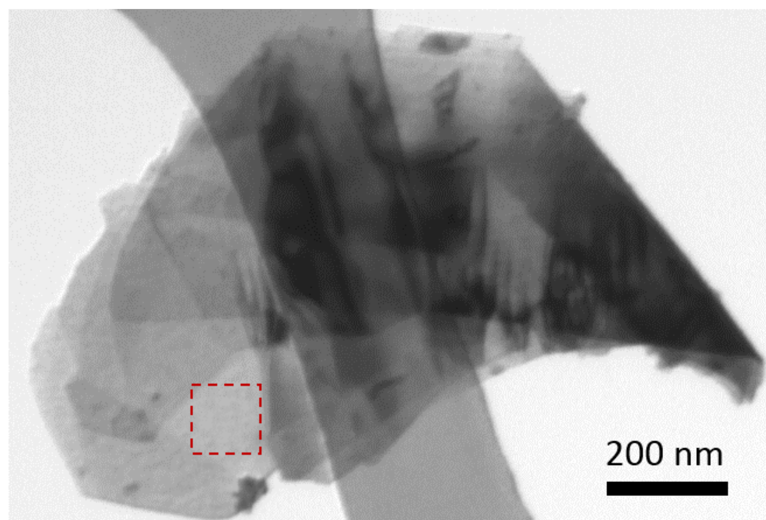

Figure 5.6: MoS_2 flake after an etching attempt with nitrogen gas. No observable etching occurred.

not deposited on the MoS_2 flake. Any deposited carbon would have been etched by the nitrogen ions.

5.1.1 Summary

A technique to controllably fabricate sub 5 nm nanopores in graphene with a low energy electron beam has been demonstrated. This method overcomes the limitations suffered by many other techniques, providing high spatial control of the etching [194]. A systematic investigation of the effects of the different parameters in the system was undertaken in order to understand and optimise the etching process. These optimised parameters were used to efficiently etch nanopores with uniform sizes and precise positioning into a flake of graphene. A model which is supported by our data was established. Ionised nitrogen molecules generated by the electron beam diffuse away from the beam resulting in an exponentially decaying etching rate. A preliminary investigation into the temperature dependence of the etching was undertaken. However, further work is required to understand its contribution. MoS_2 etching was also attempted; the lack of etching observed served to further

confirm our model which states that a chemical reaction is required for this etching mechanism to occur. This method will facilitate the fabrication of materials with controlled properties for nanodevice applications.

5.2 Defect-Engineering by He^+ and Ne^+ Irradiation

CVD was used by collaborators (G. Duesberg, Y. Zhou, TCD) to grow the graphene sample which was then transferred to a Si substrate as outlined in the literature [113]. The *ORION NanoFab* microscope was used to irradiate arrays of 5×5 μ m regions in graphene with He^+ and Ne^+ at an energy of 30 keV and at an angle of incidence of 0°. These regions received doses ranging from 1.5×10^{11} to 1×10^{16} Ne^+ cm^{-2} or 1×10^{13} to 1×10^{17} He^+ cm^{-2}. The regions were found using low dose, low magnification He^+ imaging. He^+ was chosen to minimise damage to the sample and utilise its superior imaging quality. A low dose was carefully ensured (less than 1×10^{10} He^+ cm^{-2} total from imaging). Once the desired region was located on the specimen, the desired ion species was selected. The beam was slightly defocused to ensure a uniform distribution of ions and the sample was irradiated at the desired dose. A 1 pA beam current and 10 nm pixel spacing were used. The beam dwell time at each pixel and/or the number of repeats at each position were varied to achieve the desired dose.

Raman spectra were acquired from each irradiated region and from a nearby non-irradiated region for reference. Peaks in the Raman spectra of graphene were fitted with Lorentzian functions using the fityk software package as these were found to fit the spectra most closely [172]. Error bars, where used and unless otherwise stated, are the largest of either the instrumental (1 cm^{-1}) or the fitting error as acquired from fityk which uses a weighted sum of squared residuals to measure agreement between the fit and the data [195].

In figures 5.7(a)-(d), four sets of Raman spectra, with intensity as a function of Raman shift are presented in each. The spectra obtained from the non-irradiated regions of both supported and freestanding samples are shown in black and agree with values from the literature for monolayer graphene as stated in chapter 2 [64, 66]. However, the spectra do not represent completely pristine graphene. This variation

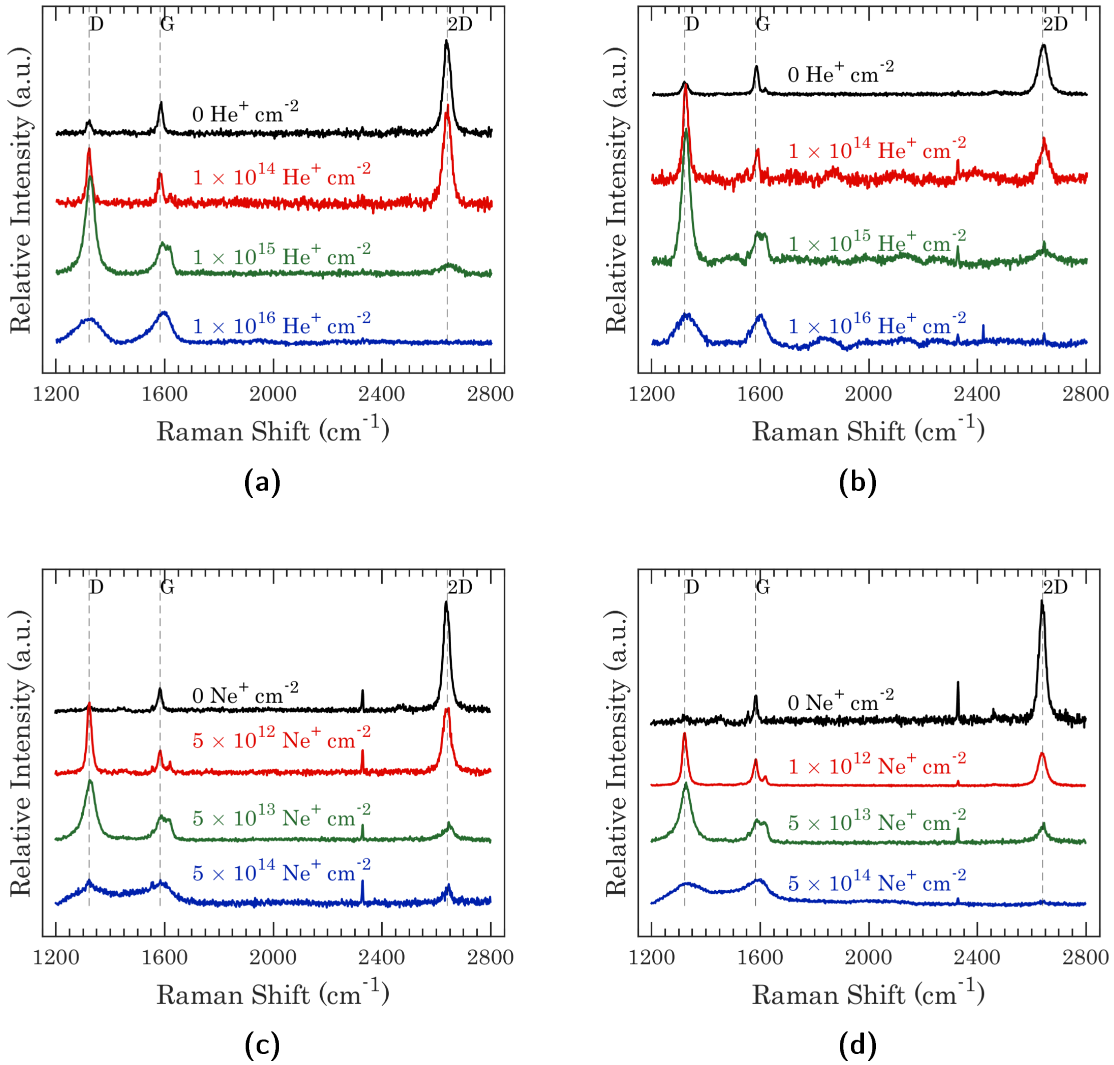

Figure 5.7: Representative selection of irradiated CVD graphene Raman spectra. The sample was excited by a 633 nm laser and irradiated with ions at 30 keV with a 0° angle of incidence. (a) freestanding graphene irradiated with He^{+}, (b) supported graphene irradiated with He^{+}, (c) freestanding graphene irradiated with Ne^{+}, (d) supported graphene irradiated with Ne^{+}. The evolution of the spectra with increased ion dose is shown descending from the top in black to the bottom in blue. The spectra are normalised to the maximum of the G peak.

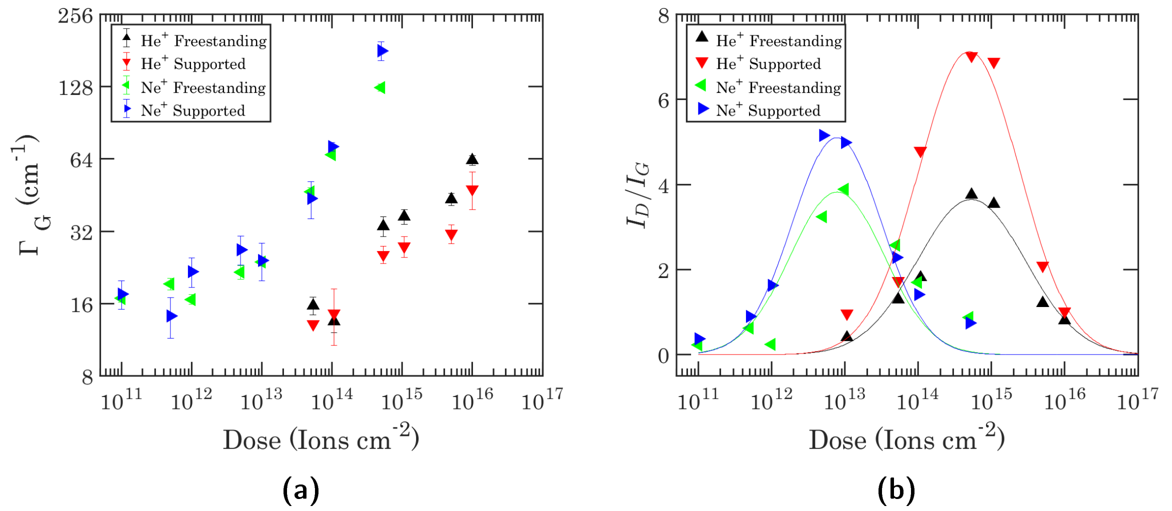

Figure 5.8: Evolution of full width at half maximum of the G peak and intensity ratio in graphene. (a) Evolution of FWHM of Lorentzian fits to the G peak, Γ_G, as a function of dose for He^+ and Ne^+ for both freestanding and supported graphene. (b) The evolution of the I_D/I_G ratio of graphene with irradiation dose. A Gaussian function has been fitted to each of the four data sets in this graph for illustrative purposes only.

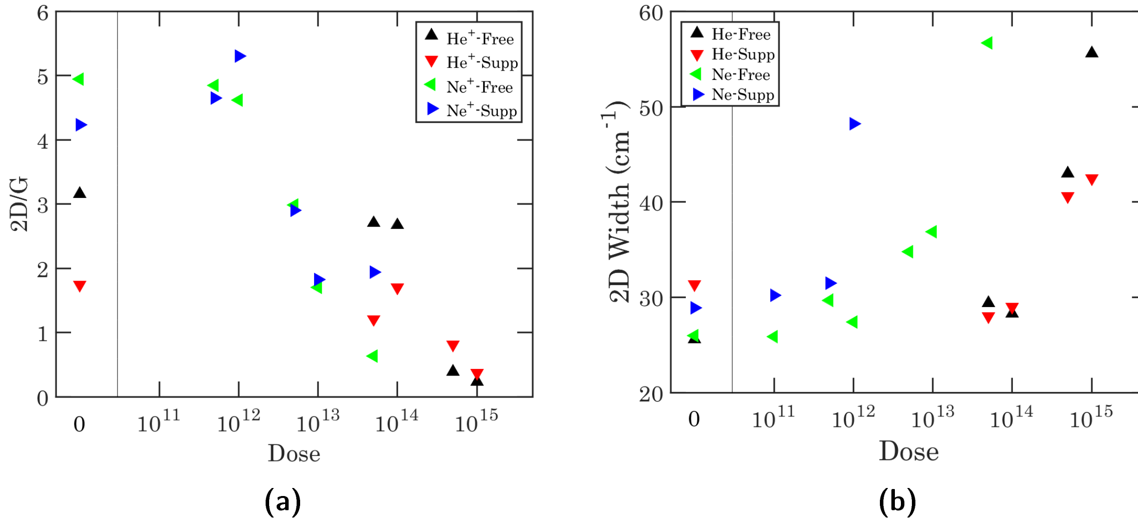

Figure 5.9: The $2D$ peak in graphene Raman spectra. (a) Graph of intensity of $2D$ over G peak as a function of ion dose. It shows inconsistency between the samples used for He^{+} and Ne^{+} not apparent in the I_D/I_G ratio. (b) Graph of FWHM of $2D$ as a function of ion dose.

is not expected to be important due to the magnitude of change affected by the ion beam being far greater. Though monolayer, the initial material is not of pristine quality. This is evidenced by the small D peak and the difference between the $2D$ peaks of the non-irradiated He^{+} sample (figure 5.7 (a),(b)) and the Ne^{+} sample (figure 5.7(c),(d)). Figure 5.9 (a) shows a graph of intensity of the $2D$ peak divided by that of the G peak as a function of ion dose. It shows inconsistency between the samples used for He^{+} and Ne^{+} not readily apparent in the I_D/I_G ratio. However, the peak was symmetrical and well fitted by a single Lorentzian in each case. The starting material always had a $2D/G$ ratio of close to 2 or more, indicative of monolayer - if slightly defective or strained - graphene. Figure 5.9 (b) shows a graph of the FWHM of the $2D$ peak as a function of ion dose. A FWHM of ~30 cm^{-1} is indicative of monolayer graphene [64, 75].

In each graph in figure 5.7, multiple spectra are shown, descending with increased ion dose. Evolution through the previously discussed stages is illustrated as follows: The first spectrum (black) represents the non-irradiated graphene; the second spec-

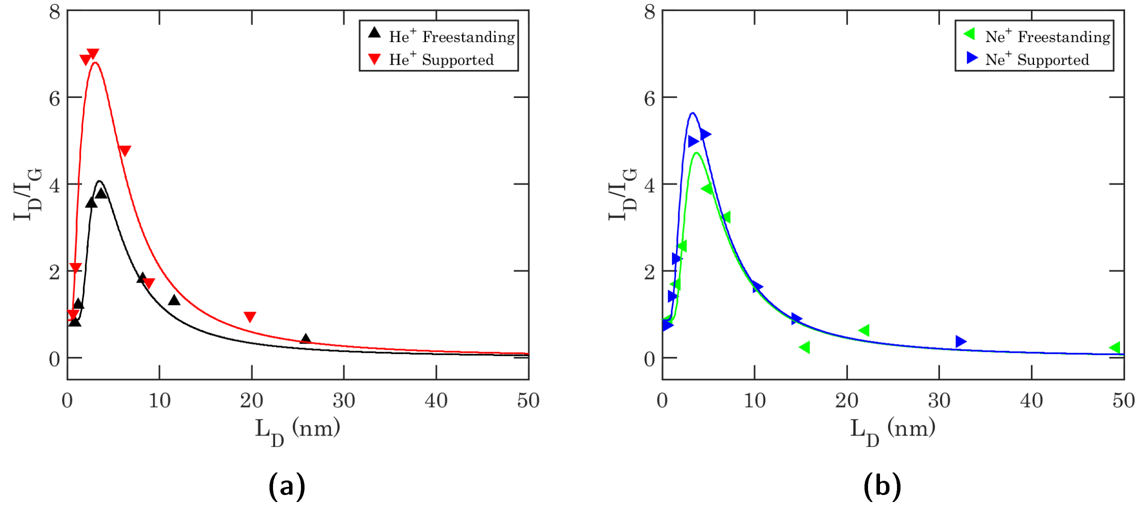

Figure 5.10: The evolution of the I_D/I_G ratio of freestanding and supported graphene with L_D for (a) He^+ and (b) Ne^+. The points represent experimental data and the lines are from a non-linear fit of equation (5.3) [26].

trum (red), represents the first stage (as defined in chapter 2), where the defect activated D peak can be observed to have increased in intensity (w.r.t G band) at ~1322 cm^{-1}; the third spectrum (green) cannot be assigned unambiguously to a stage, but it is approximately at the end of the first or the beginning of the second stage as evidenced by the D peak being close to its maximum; finally, the fourth spectrum (blue) represents the third stage. Here the highest ion dose was applied, and the Raman spectra have now been altered such that the material is amorphous carbon with little to no remaining crystallinity.

The width of the G peak increases as a function of ion dose as shown in figure 5.8(a) for both He^+ and Ne^+. With increasing dose, the G peak is observed to consistently broaden and decrease in intensity, representing an unequivocal increase in structural disorder. Given their increased mass, Ne^+ ions have an enhanced milling capability at the incident surface compared to He^+, and here the effect of using the heavier Ne^+ instead of He^+ at the same energy is highly pronounced [129]. While the trends are similar, the incidence of the Ne^+ species causes evolution of the G peak to occur at ion doses which are lower by between one and two orders of magnitude.

Ion	Graphene	$\gamma_{C(SRIM)}$	$\gamma_{C(MD)}$	$\alpha_{C(fit)}$
He^{+}	Freestanding	0.010	0.006	0.016
He^{+}	Supported	0.137	–	0.027
Ne^{+}	Freestanding	0.236	0.156	0.414
Ne^{+}	Supported	3.15	–	0.965

Table 5.1: Sputtering yields and defect per incident ion values of carbon atoms in graphene. Irradiation performed with He^{+} and Ne^{+} at 30 keV and 0° angle of incidence for the four different arrangements discussed in the main text. $\gamma_{C(SRIM)}$ is calculated using SRIM, $\gamma_{C(MD)}$ is calculated using the online simulation code from Lehtinen et al. and $\alpha_{C(fit)}$ is calculated from the fits shown in figure 5.10 [134, 196].

Two reasons for this inconsistency and non-pristine behaviour are suggested. The first is the inherent non-uniformity which is possible in CVD prepared graphene. Regional inconsistency even for the same layer number is not unusual for the $2D$ peak of CVD-grown graphene [63]. The second is the possible inconsistent levels of polymer residue left over from the transfer process used in preparation. In either case, this inconsistency is not expected to be dominant due to the magnitude of change affected by the ion beam being far greater.

In figure 5.8(b), the evolution of the I_D/I_G ratio against dose is displayed for both He^{+} and Ne^{+} and for both freestanding and supported graphene. The three stages previously outlined are observed. I_D/I_G of the supported graphene is noted to rise faster and reach a much higher maximum than the freestanding material. This is discussed further in relation to defect sizes later. To aid the understanding of these results, the interaction of the ions upon incidence with the specimen must be considered.

The sputtering yields of graphene were calculated using SRIM simulations ($\gamma_{C(SRIM)}$) [131, 197]. SRIM is not expected to be quantitatively accurate for ion-nanomaterial systems where molecular dynamics is a superior, albeit far more computationally expensive choice [34, 132–134]. In calculating the yield of carbon atoms from graphene, SRIM accounts for those carbon atoms removed directly by

Labels	Limit		Initial		Limit
L_S (nm)	1	$\leq$	2	$\leq$	5
r_S (nm)	1	$\leq$	0.6	$\leq$	5
C_A	7.6	$\leq$	10.8	$\leq$	14.1
C_S	0.87	$\leq$	0.87	$\leq$	0.87
α_C	0.00	$\leq$	γ_C	$\leq$	2^1

Table 5.2: Initial fitting parameters for use with the modified version of the model developed by Lucchese et al.

Ion	Graphene	r_S (nm)	r_A (nm)	$L_D \left(\frac{I_D}{I_G}\right)_{max}$ (nm)	$\left(\frac{I_D}{I_G}\right)_{max}$
He^+	Free	1.83	2.93	3.48	3.93
He^+	Supp	0.68	2.81	2.75	6.47
Ne^+	Free	1.62	3.19	3.70	4.72
Ne^+	Supp	1.12	3.02	3.28	5.64

Table 5.3: Key figures calculated from fitting the model developed by Lucchese et al.(as in equation (5.3))[26]. r_S is the average defect size, calculated from fitting equation 5.3 to graphene experimental data as in figure 5.10.

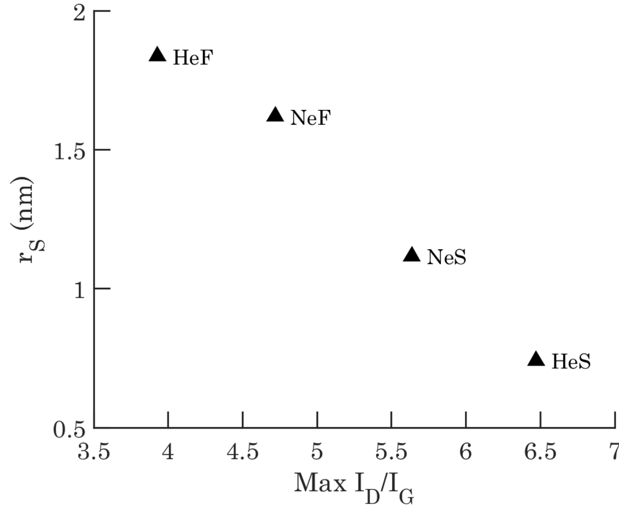

Figure 5.11: Graph of defect size (r_s) against the maximum of the I_D/I_G peak for each of the four irradiation scenarios for graphene.

the primary ion beam and those which are removed by backscattered primary ions. The sputtering yields of both ions when interacting with the sample (both freestanding and supported) are shown in table 5.1. The four scenarios applied in experiment were also simulated: (i) freestanding, irradiated with He^+, (ii) supported, irradiated with He^+, (iii) freestanding, irradiated with Ne^+, and (iv) supported, irradiated with Ne^+. As can be seen in table 5.1, the sputtering yields calculated using SRIM for each ion are much larger for supported than freestanding graphene. The effects of secondary atoms from the substrate and, to a lesser extent, ions backscattered by it are thus expected to have a significant impact on the rate of defect introduction to the graphene layer. Nonetheless, SRIM was used to provide initial estimates of sputtering yields for an iterative fit of equation 5.3 to experimental data. Values calculated using molecular dynamics are also presented in table 5.1. These were calculated from the work of Lehtinen et al. who investigated the effects of different ion species on the incidence of single vacancy, double vacancy and other more complex defect types in freestanding graphene [134].

In the previous work of Lucchese et al., low energy (90 eV) Ar^+ ions were used

to alter L_D in graphene which was investigated using Raman spectroscopy [26]. This study provided a model with which to quantify defects in graphene. Cançado et al. expanded the model to multiple Raman excitation energies [27]. In these studies, L_D was calculated based on the expected density of defects, σ, which is estimated from the irradiation dose, S, in ions per nm^{-2}. The approximation that $\sigma \simeq S$ was used which assumes a random distribution of ions, yielding:[26, 28, 29]

$$L_D = 1/\sqrt{\sigma} \tag{5.1}$$

This is a valid assumption for ions with a suitable cross-section for creating a single carbon vacancy defect. The 90 eV Ar$^+$ ions applied to graphene by Lucchese et al. are one such example due to their relatively large mass and low energy. The vast majority of ions do indeed interact with surface carbon atoms but due to the low energy can only remove one carbon atom each. However, in this work the irradiation species are much lighter and at much higher energies than those used by Lucchese et al., making this assumption no longer valid. The dose used to calculate L_D must be corrected by the probability of creating a defect (i.e. the number of D band active zones created per ion), α_C, so that $\sigma \simeq S\alpha_C$ and thus:

$$L_D = 1/\sqrt{S\alpha_C} \tag{5.2}$$

α_C is distinguished from the sputtering yield of carbon from graphene, γ_C, because not all defects causing D band activation need necessarily be a vacancy. However, γ_C, is easily calculated as a useful reference and is used as a seed value for α_C in fitting.

This is a valid assumption for ions with a suitable cross-section for creating a single carbon vacancy defect. The 90 eV Ar^+ ions applied to graphene by Lucchese et al. are one such example due to their relatively large mass and low energy. The vast majority of ions do indeed interact with surface carbon atoms but due to the low energy can only remove one carbon atom each. However, in this work the irradiation species are much lighter and at much higher energies than those used by Lucchese et al., making this assumption no longer valid. The dose used to calculate L_D must be corrected by the probability of creating a defect (i.e. the number of D band active zones created per ion), α_C, so that $\sigma \simeq S\alpha_C$ and thus:

$$\frac{I_D}{I_G} = C_A \frac{(L_S^2 + 2r_S L_S)}{(L_S^2 + 2r_S L_S - r_S^2)} \left[e^{-\pi r_S^2/L_D^2} - e^{-\pi(L_S^2+2r_S L_S)/L_D^2} \right] + C_S \left[1 - e^{-\pi r_S^2/L_D^2} \right] \tag{5.3}$$

The fitting of equation (5.3) was performed using the *lsqcurvefit* function in *matlab*. The initial values and bounds for the parameters were informed from the literature and used as in table 5.2 [26, 71]. γ_C as from table 5.1 was selected as a seed value for α_C. C_A is calculated from equation (2.2) with a relatively large margin of error at 10.8±3.3 for the 633 nm wavelength excitation source used here [27]. It was then found to consistently converge between 7.6 and 8 so it was set at its lower bound of 7.6 and the fitting repeated. The values shown in table 5.3 were obtained. r_A was calculated from the relation $r_A = L_S + r_S$.

The fits of equation 5.3 are applied to the four data sets in 5.10(a) and (b), showing the close agreement of the experimental data and the fitted equation. The values for α_C obtained by fitting, $\alpha_{C(fit)}$, are shown in table 5.1 alongside their corresponding seed values found using SRIM, $\gamma_{C(SRIM)}$, and those found using the molecular dynamics-derived method of Lehtinen et al., for freestanding graphene only, $\gamma_{C(MD)}$ [196]. The sputtering yield of He^+ on freestanding graphene has also been measured experimentally before using a single pixel exposure to completely mill through a graphene layer [198]. The value reported by Buchheim et al. is $\gamma_C = 0.007$, which is in close agreement with atomistic simulations [198]. Given that this figure neglects defects that do not involve sputtering, it is expectedly smaller than the value of α_C obtained in this work. Similarly, in the case of Ne^+ on freestanding graphene, we obtain a value of α_C which is more than twice the value of γ_C from molecular dynamics. In freestanding graphene, the dominant defect introduction process is expected to be the interaction of the direct ion beam. However, in supported graphene this is in conjunction with defects introduced by low energy secondary atoms which have been sputtered from the substrate. The obtained result, that α_C is consistently larger for supported than freestanding graphene, is thus in keeping with expectations.

It is noted that the maximum I_D/I_G value is considerably higher for supported graphene than for freestanding graphene. It is observed from equation 5.3 and demonstrated in figure 5.11 that there is a negative linear relationship between r_S and the I_D/I_G ratio. Depending on many factors, but principally the irradiation

	Ion	r_S	m_a	
	He^+	0.68 nm	4	
<	Ne^+	1.12 nm	20.1	
<	Ga^+	1.6 nm	69.7	[39]

Table 5.4: Comparison of three ion species at 30 keV. The average size of defects they induce in supported graphene and their masses are compared.

species, energy and angle, we can generally expect r_S values between approximately 0.8 and 2.5 nm [29, 199]. It has been established that larger incident species generally produce larger defects. [29, 134, 196] However, in the freestanding case, r_S is unexpectedly not found to be larger for Ne^+ than He^+, despite the very different ion mass. This He^+ behaviour may be related to a similarly unexpected experimental finding by Gawlik et al. [199]. Also observable are the substantially higher values for r_S for freestanding than supported graphene. Lehtinen et al. found that the size of defects introduced by the direct ion beam typically increases with ion energy [134]. While the high energy interaction of the direct beam is expected to be causing large defects, it also energises lower energy atoms which in turn produce numerous, smaller graphene defect sites.

For supported graphene irradiated with 30 keV He^+, r_S has been found to be ~0.8-1 nm [39, 74]. The value obtained in this work for He^+ is slightly smaller than previous reports [39, 74]. Since the mass of Ne^+ is between those of He^+ and Ga^+, by a simple argument, it might be expected that the corresponding r_S value would be similarly intermediate. Although unclear in the case of freestanding experiments as previously discussed, this is indeed true for supported graphene (. Ga^+, also incident on supported graphene and also at 30 keV, has been reported to create defects of r_S = 1.6 nm [39]. Thus the trend for supported graphene is clearly one of increasing defect size (with increasing ion mass, m_a, see table 5.4). It is proposed that the larger ion transfers energy more efficiently to substrate atoms (the masses of Si and Ne are very close), and it is these atoms, being more energised than their He^+ induced counterparts, which create larger defects in the graphene layer. The

variety of r_S values obtained in this work suggest a variety of defect types with different weighting in the four different experimental scenarios. Such defects may include single vacancies, double vacancies, complex defects or amorphisation events [134, 196]. It underscores the importance of choosing ion and substrate carefully for both nanofabrication and defect engineering.

An assumption made in this work is that, in calculating the sputter yield, it is independent of L_D. However, it is known that under-coordinated atoms are more easily displaced and this might mean that the α_C values calculated in this work are likely too high for pristine material and too low for defective material [200].

There is clear evidence that different maximum I_D/I_G ratios are not caused by substrate effects alone (using plasma to control L_D in this reference) [201].
There are other possible effects of the substrate; it has been reported to increase the threshold displacement energy of atoms in graphene [136]. This effect should not have a very large impact under the direct beam due to the much higher energy involved, but it may be important for secondary atom interactions [202]. In addition, one experimental report using Ga^+ found that single layer graphene on a SiO_2/Si substrate was removed ~7 times slower than freestanding graphene [132]. However, since this study used scanning electron microscopy rather than Raman spectroscopy, it did not measure the progression of the crystal quality of the material with dose.

There is a stark contrast between the maximum transferable energy, T_m, of He^+ and Ne^+ to Si atoms. Calculated using equation 5.4, the values for He^+ and Ne^+ to Si atoms are 13.1 keV and 29.1 keV respectively. Furthermore, SRIM gives average values of energy transferred to sputtered Si atoms as 1.5 keV and 2.2 keV, respectively. This suggests that Ne^+ is more likely to create sputtering cascades in the near surface region, with secondary atoms of greater energy than thos induced by He^+. This should greatly enhancing the probability of creating defects in supported graphene and should also be responsible for creating larger defect sizes.

$$T_m = \frac{4M_1M_2}{(M_1 + M_2)^2}E \tag{5.4}$$

The simulation was used to track 100,000 He^+ or Ne^+ at an angle of incidence of 0° into freestanding or supported graphene. The graphene samples were set up as a 0.35 nm carbon layer (C density = 2.25 g cm^{-3}). The supported graphene samples

were also set up to include a 700 nm Si substrate (Si density = 2.32 g cm^{-3}). For freestanding graphene, the atomic displacement threshold energy, T_d, used was 23 eV. It is in good agreement with values from a range of methods including molecular dynamics and first principles calculations [203–205]. For supported graphene, T_d=68 eV and the surface binding energy, E_B=15 meV, were used as in other studies [44, 136, 206].

5.2.1 Summary

The effects of He^+ and Ne^+ irradiation at 30 keV on graphene have been explored using models applied to Raman spectra. We believe this represents the first experimental comparison of defect sizes produced in 2D materials by different noble gas ion probes. The dose dependence of irradiation species and arrangements to inter-defect distance has been established for graphene. In addition, a comparison of the sizes of the defects produced demonstrates the effects of both ion species and secondary, substrate atoms in graphene. The effects of substrate atoms on defect production and size are also highlighted as a concern for nanofabrication technology due to the clear secondary atom effect. These results will allow a substantially better informed and more precise defect engineering of graphene which is both supported and freestanding.

Chapter 6

Irradiation and Patterning of MoS_2

In this chapter, the engineering by ion irradiation of MoS_2 was investigated, including: changes to Raman spectra for a variety of layer numbers; the preferential sputtering of sulphur (and consequent effect on stoichiometry) and the localised tuning of resistivity MoS_2.

In chapter 5, noble gas ion beams were used for precise defect-engineering of graphene, characterised by Raman spectroscopy. A model established a clear relationship between the Raman spectra and the average inter-defect distance. A similar model is applied here in the defect-engineering of monolayer MoS_2. The first report of ion irradiation effects on the low frequency (<50 cm^{-1}) Raman modes of bilayer MoS_2 is also provided as well as a study of various effects on thicker (4-5 L) material.

By adjusting the He^+ ion dose, semiconducting, metallic-like, or insulating behaviours were induced. Amorphous MoS_x with metallic-like behaviour has been demonstrated for the first time. A variety of irradiation methods were also developed for the high-resolution patterning of nanoribbons and for the tuning of thickness in MoS_2. Fabrication of MoS_2 nanostructures with 7 nm dimensions and pristine crystal structure was also achieved. The damage at the edges of these nanostructures was typically confined to within 1 nm. This damage was also modelled using an array of Gaussian distributions. Nanoribbons with widths as small as 1 nm were reproducibly fabricated. These micro and nanoscale modification techniques are readily generalizable to various 2D materials and can alter a wide range of material properties and geometries.

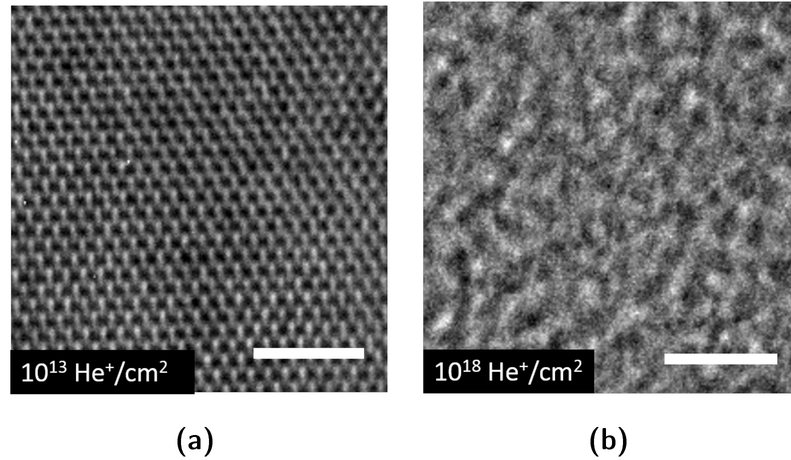

Figure 6.1: Modification of few layer mechanically exfoliated MoS_2 crystal structure with He^+ imaged in TEM. (a) and (b) show TEM images of irradiated MoS_2 with low (1×10^{13} He^+ cm^{-2}) and high (1×10^{18} He^+ cm^{-2}) doses respectively. The scale bars are 2 nm in length.

6.1 Structural Modification and Defect-Engineering

As discussed in chapter 4, Raman spectroscopy is a high throughput and usually non-destructive optical technique which can be used to characterise the vibrational modes of crystal structures. Chapter 5 showed the use of the model developed by Lucchese et al. for relating the average inter-defect distance to the Raman spectrum of graphene [26]. To expand this study to reflect the wide variety of 2D materials being modified with ion beams, similar experiments were performed with a variety of MoS_2 samples of different layer number and prepared by different methods. However, since MoS_2 has stoichiometric amongst other complexities when compared to graphene, other experiments were also performed.

Mechanical exfoliation of MoS_2 flakes was performed from bulk MoS_2 crystals (*SPI Supplies*) on a Si substrate with a 285 nm oxide layer by the *Scotch*-tape micromechanical cleavage technique. The layer thickness was identified using optical contrast and AFM. Few layer samples (monolayer to trilayer) were selected for the experiment. The crystal structure was directly observed by high-resolution TEM imaging of a freestanding mechanically exfoliated sample. The TEM used was an

FEI Titan 60-300 operated at 300 kV. The TEM chamber pressure was 40 μPa. For EDX mapping, the system was operated in STEM mode. The STEM beam had a probe size of 0.5 nm and a probe current of 0.5 nA. A pixel spacing of 1.7 nm and an acquisition time of 1 s per pixel were used during mapping.

Figure 6.1(a) shows the hexagonal structure of MoS_2 which has been irradiated with a low He^+ dose of $1.00 \pm 0.02 \times 10^{13}$ He^+ cm^{-2}. In figure 6.1(b) at a He^+ dose of $1.00 \pm 0.02 \times 10^{18}$ He^+ cm^{-2} the hexagonal crystal structure was no longer observed so the sample was amorphous. For a freestanding sample, a He^+ dose that is approximately one order of magnitude greater is expected to be required to create the same irradiation effects as a sample on a substrate [113]. It is clear from the Raman and TEM results that the crystal structure of the MoS_2 was controllably amorphised by the He^+ irradiation process. This combination demonstrates the ability of He^+ irradiation to alter the crystal structure by defect introduction and material removal.

Another sample of MoS_2 was synthesised by collaborators (M. O'Brien, G. Duesberg, TCD) using a previously reported CVD technique and regions of bilayer material were identified by OM [207]. The thickness was confirmed by a separation of the E^1_{2g} and A_{1g} peaks of 21 cm^{-1}, characteristic of bilayer MoS_2 [11, 112]. The effect of He^+ irradiation on low frequency interlayer Raman modes was then studied. MoO_3 precursor substrates were placed face-up in a ceramic boat with a blank substrate face down on top of this. This was then placed in the centre of the heating zone of a quartz tube furnace, and ramped to 750°C under 150 SCCM of Ar flow. Sulphur vapour was then produced by heating S powder to ~120°C in an independently controlled upstream heating zone of the furnace, and carried downstream to the MoO_3 for a duration of 20 mins after which the furnace was held at 750°C for 20 mins, then cooled down to room temperature.

Figure 6.2(a) shows the acquired spectra. Two peaks are found which are in excellent agreement with the expected positions for bilayer MoS_2 [108]. The first is the SM at ~22.5 cm^{-1} and the second is the LBM at ~39.5 cm^{-1}. It should be noted that for the 8×10^{14} He^+ cm^{-2} dose, there is an additional peak found at ~29 cm^{-1}. This is likely due to the selected region not being made up of entirely bilayer MoS_2. The presence of 3L or 4L MoS_2 would result in a peak appearing near this position. Therefore, that region and corresponding dose has been omitted from subsequent

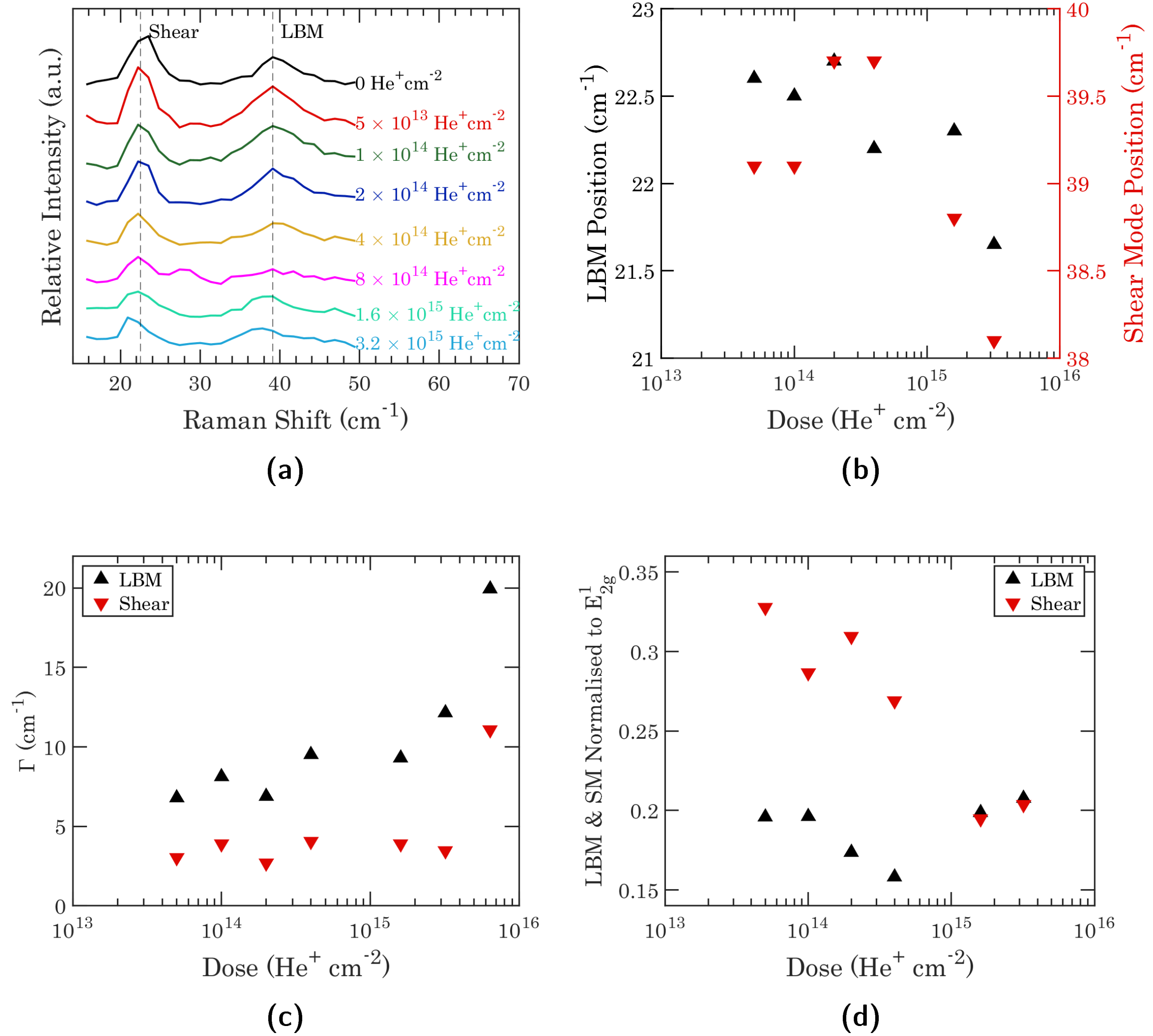

Figure 6.2: Low frequency Raman modes in bilayer MoS_2. (a) shows the acquired low frequency spectra with the two characteristic peaks labelled accordingly. (b) is the evolution of the peak position with dose showing the red shift of both peaks. (c) is the evolution of the widths of the two low frequency modes with dose. (d) shows the height of the two peaks normalised to the E^1_{2g} peak.

analysis.

Figure 6.2(b) shows the position of the two peaks as a function of dose. There is little significant observed change below a dose of 1×10^{15} He^{+} cm^{-2} after which it appears that both peaks begin to red shift. This is in good agreement with the literature where it has been shown that biaxial strain present in suspended MoS_2 causes a similar shift of both peaks in bilayer material [83]. That ion irradiation introduces local strain is already well established from studies of the E^1_{2g} peak [104].

Figure 6.2(c) shows the changing widths of the two peaks. In this case the lowest dose at which a significant change is observed is 3.2×10^{15} cm^{-2}. Both peaks are observed to broaden at the highest dose, attributable to the general increase in disorder. Figure 6.2(d) shows the heights of the two low frequency modes normalised to the E^1_{2g} peak in the normal spectral range. Interestingly, the intensity of the LBM is relatively constant with respect to the E^1_{2g} peak while the SM is clearly observed to diminish. Since the ion beam is expected to introduce a large density of defects in the material, it is quite likely that these defects affect the tribological behaviour of the interacting layers, restricting the SM while leaving the LBM relatively unaffected. Previous reports of high energy ions and bulk MoS_2 suggest strong effects on the tribological behaviour, in particular a greater friction coefficient [208].

Figure 6.3(a) shows PL spectra from the same regions of bilayer MoS_2 as studied with low frequency Raman spectroscoy. Figure 6.3(b) shows three of the highest doses replotted for clarity. The PL spectra were acquired with a *WITec alpha 300R* using a 532 nm laser with a power of <1 mW and a spectral grating with 600 lines/mm.

Absorption peaks are expected at 670 nm and 627 nm corresponding to the A and B direct excitonic transitions respectively [9, 209]. While both are present, the B exciton appears unusually weak in intensity compared to the A exciton. This could be caused by several scenarios including the presence of some monolayer MoS_2 which has very high A exciton intensity. This would cause the B exciton to appear relatively weak. Alternatively, strain effects could be causing enhancement of the A exciton as has been noted for bilayer MoS_2 before[83].

The A exciton peak intensity decreases with increasing ion dose, particularly in the range between 8×10^{14} He^{+} cm^{-2} and 1.6×10^{15} He^{+} cm^{-2}. It is finally undetectable at the dose of 1.28×10^{16} He^{+} cm^{-2}. It also red shifts as shown in figure 6.3(c). This

shift in position is attributed to strain caused by ion-induced defects [209]. The B exciton peak is extremely weak compared to the A peak and it also declines with increasing dose. Its weakness makes measuring changes to its position too inexact for comparison. Although other forms of ion and plasma irradiation have been associated with increases in both peaks, that is not apparent here [210, 211].

Another sample was prepared using the same CVD method and this time regions of monolayer MoS_2 were identified. In figure 6.4, the characteristic E' and A'_1 peaks of monolayer MoS_2 are marked by grey dashed lines. They are clear in the pristine spectra (in black) and are in good agreement with the literature. The E' peak, visible at ~383 cm^{-1} comes from the intra-layer, in-plane motion of Mo and S atoms with respect to each other. The A'_1 peak at ~401 cm^{-1} comes from the intralayer, out of plane motion of S atoms [11, 13, 84, 101, 106, 212]. The small separation of these two peaks (~18 cm^{-1}) is indicative of monolayer MoS_2. With increasing ion dose, reductions in intensity and broadening of these two characteristic peaks are observed. This reflects the growing disorder which the ion beams create in the material. To examine the spectra in greater detail, Gaussian peaks were fitted to the spectra and their parameters compared. The evolutions of peak width and peak position of the E' and A'_1 peaks are shown in figures 6.5 (a) and (b) respectively. Both peaks are observed to broaden with increasing disorder. The onset of broadening occurs at a substantially lower dose for Ne^+ than for He^+, although the trend has a similar shape as expected. The most dramatic change with increasing dose of both ions is the red shift of the E' peak. This downward shift in energy is attributed to the introduction of defects causing lattice distortion, reflected in the Raman spectrum similarly to tensile strain [11, 104, 106, 111, 112, 135]. Changes in the position of the A'_1 peak are considerably lower in magnitude, although it does blue shift for some of the higher doses used, as previously reported [28].

Figure 6.4 also shows the emergence of a new peak, particularly at high doses. This peak, at ~226 cm^{-1} in these spectra (dashed grey line), has been labelled as the $LA(M)$ mode [103]. Its fitting is discuseed in appendix D. Mignuzzi et al. drew an analogy between the $LA(M)$ peak in MoS_2 and the D peak in graphene as both are defect-activated and when normalised represent a good measure of disorder [28].

Mignuzzi et al. used equation 2.3 to describe the effect of introducing defects on

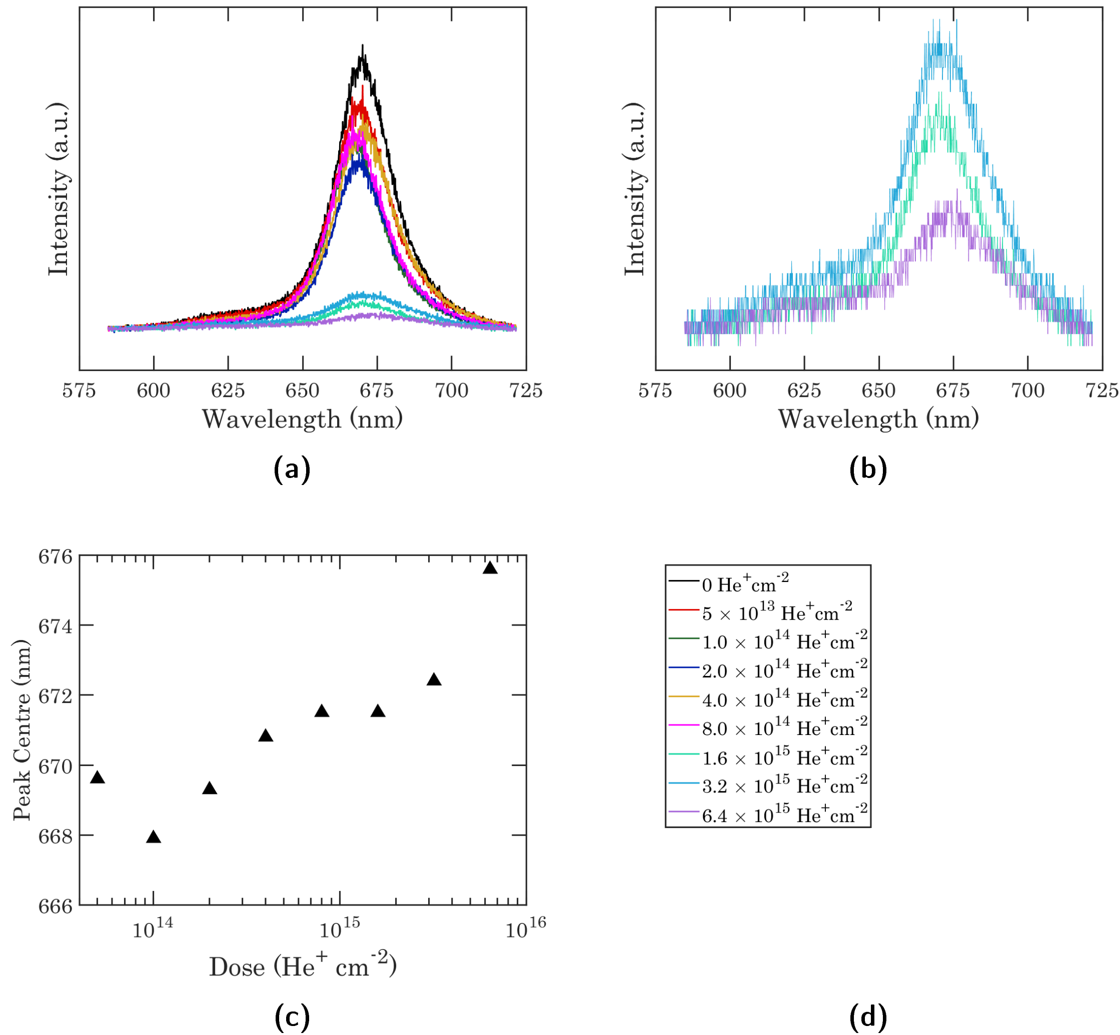

Figure 6.3: Ion dose dependent photoluminescence spectroscopy of bilayer MoS_2. (a) shows the decline of intensity with dose. (b) replots the three highest doses from (a) for clarity. The B exciton is relatively strong in these highly irradiated regions compared to the pristine and low dose regions. (c) is a graph showing the changing position of the A exciton peak with dose. (d) is the legend applicable to the graphs in (a) and (b).

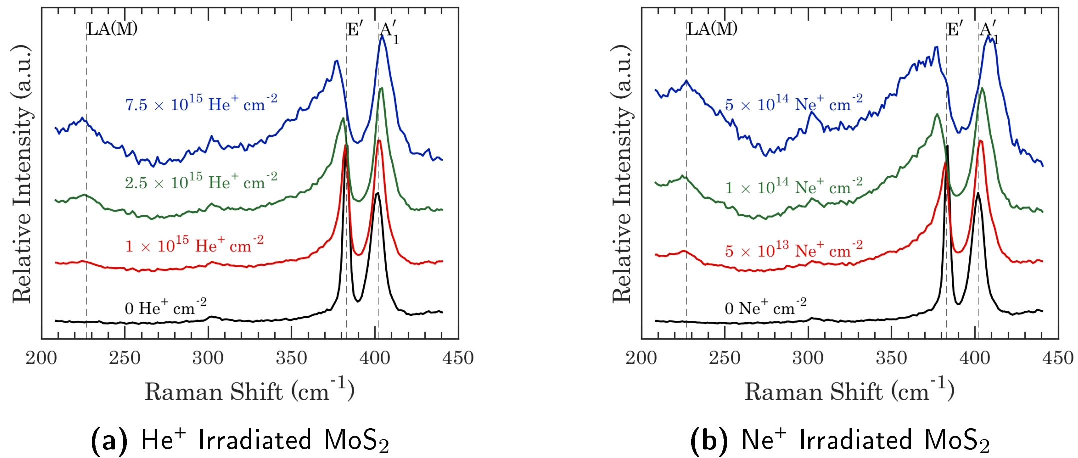

(a) He^+ Irradiated MoS_2 **(b)** Ne^+ Irradiated MoS_2

Figure 6.4: A representative selection of Raman spectra of monolayer MoS_2 with increased ion doses descending from pristine at the bottom (in black) to the highest dose at the top (in blue). A 532 nm laser was used as the excitation source. Material irradiated with He^+ is shown in (a) and material irradiated with Ne^+ is shown in (b). Both ion species had an incident energy of 30 keV.

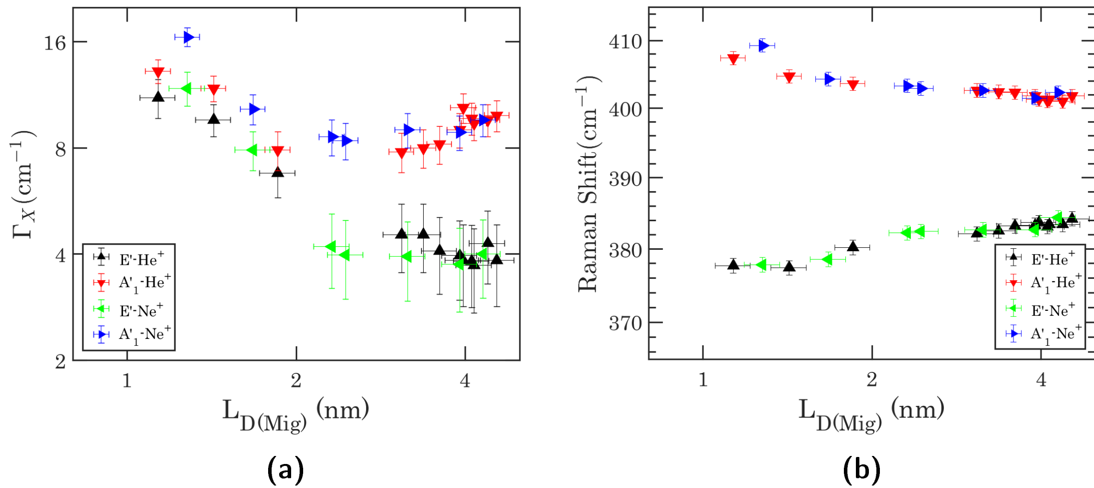

(a) **(b)**

Figure 6.5: Evolution of the FWHM and peak position with $L_{D(Mig)}$ for monolayer MoS_2. (a) shows the FWHM (Γ_X) of MoS_2 Raman modes and (b) shows the peak position with $L_{D(Mig)}$.

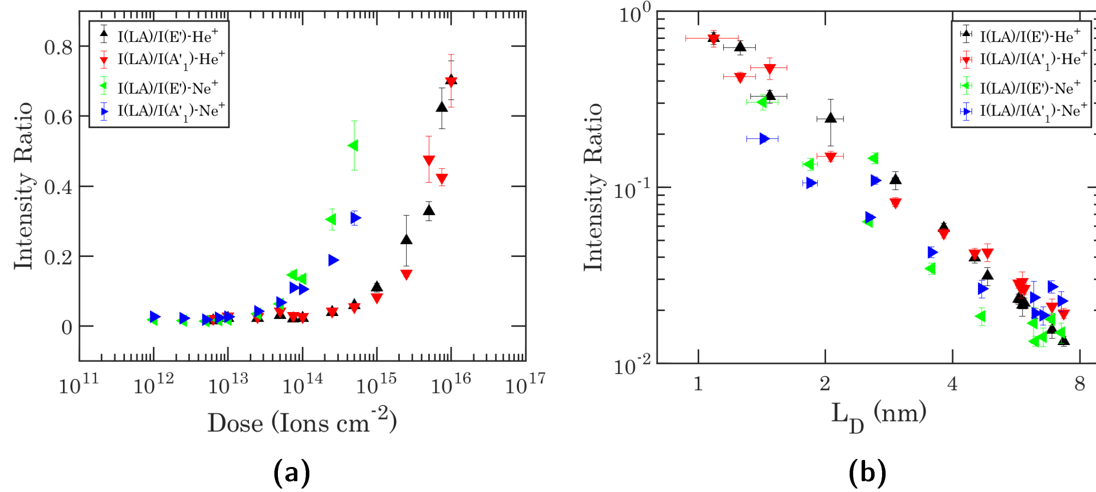

Figure 6.6: Evolution of the ratios of the intensity of the $LA(M)$ peak to the intensity of the E' and A'_1 modes for both He^+ and Ne^+ irradiated monolayer MoS_2. (a) plots these ratios against ion dose and (b) plots the same ratios but against L_D (the values of which are calculated as described in the main text).

the Raman spectrum of MoS_2 [28]. These ratios are shown for the He^+ and Ne^+ used in this work in figure 6.6. This equation and the constants provided previously were used to calculate the corresponding average inter-defect distance from experiment, $L_{D(Mig)}$, for both peaks. The average value from both the E' and the A'_1 peaks was then calculated for each ion species. It is this value which is used on the x-axis of figures 6.5(a),(b) and 6.6(b). In addition to the caveats associated with this equation previously discussed for graphene, there is the compounding factor that MoS_2 is not a monoatomic material, suggesting a more complex nature between its defects and its Raman spectrum. In addition, Mignuzzi et al. make an implicit assumption that each ion causes one defect. However, unlike in the work of Lucchese et al. where ions of much lower energy were used, this is not a safe assumption for either the 25 keV Mn^+ used by Mignuzzi et al. or indeed the 30 keV ions used in this work.

Doses above approximately 5×10^{15} He^+ cm^{-2} or 5×10^{14} Ne^+ cm^{-2} have resulted in severe changes in the spectra to the extent that little or no resemblance is borne to the starting material. This severe breakdown occurs at a Ne^+ dose which is between

one and two orders of magnitude less than that of He^+.

6.2 Stoichiometry Tuning

To gain a better understanding of the effects of the He^+ irradiation process, chemical composition analysis was performed using EDX. Doses from $1.00 \pm 0.02 \times 10^{16}$ to $1.60 \pm 0.03 \times 10^{20}$ He^+ cm^{-2} were used to irradiate a mechanically exfoliated, freestanding, few-layer MoS_2 sample. Suitable regions were identified using TMSEM as discussed in appendix A. The irradiated region of MoS_2 is displayed in the HAADF STEM image in figure 6.7(a). Each region (labelled from 1 to 15) was irradiated with twice the dose of the previous region with a starting dose of $1.00 \pm 0.02 \times 10^{16}$ He^+ cm^{-2} at region 1. At doses of $2.56 \pm 0.02 \times 10^{18}$ He^+ cm^{-2} (region 9) and above milling was observed. EDX spectra from each of the regions labelled 1-8 were recorded. The evolution of the stoichiometry of the material with respect to the He^+ dose is shown in figure 6.7(b).

It was observed that as the He^+ dose increased to 10^{17} He^+ cm^{-2} (where the sample is predominantly amorphous), preferential sputtering of sulphur from the sample occurred. Intuitively it is clear why sulphur should be subjected to preferential erosion compared to molybdenum. The mass of sulphur atoms is three times less than that of molybdenum. Upon collision, He^+ transfers more energy to sulphur than to molybdenum. As in the collision of spherical objects in classical mechanics, the closer the masses are, the more efficient the exchange of energy is. The helium ion is much lighter than both sulphur and molybdenum, but is still much closer in mass to sulphur than molybdenum. After the collision sulphur atoms will have a lot more energy than molybdenum atoms. This preferential sputtering of sulphur has been observed for both electron and argon ion beams in the past [33, 213]. However, our technique enables localized stoichiometry modification and regions with a range of stoichiometries were produced within a region of just a few tens of nanometres. At doses above $\times 10^{18}$ He^+ cm^{-2} (region 9) complete removal of material was observed for this sample.

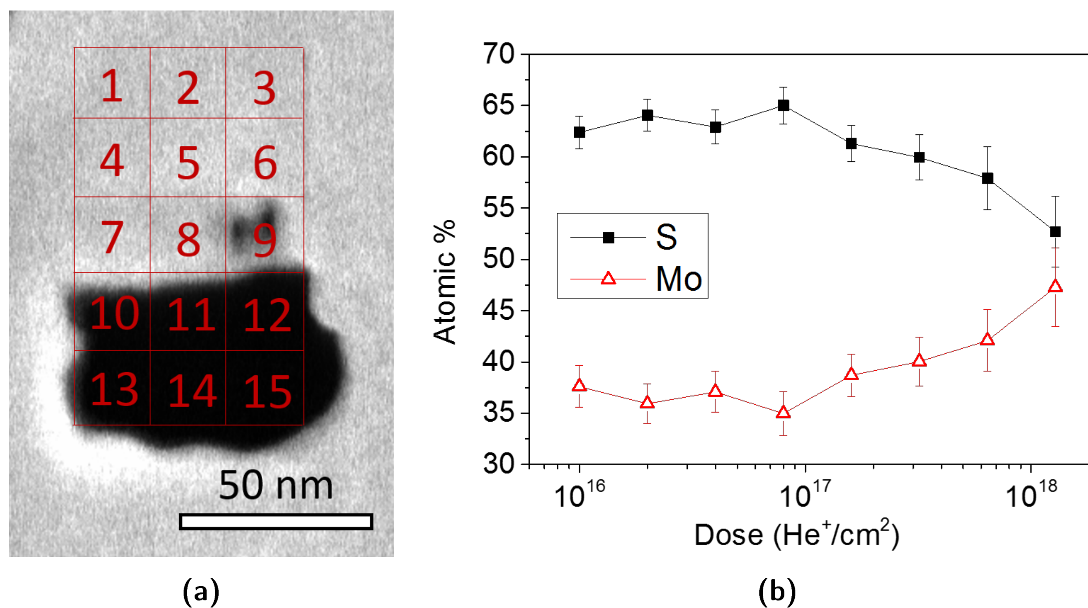

Figure 6.7: Stoichiometry alteration of a few layer MoS_2 flake by He^+ irradiation. (a) STEM image of a freestanding MoS_2 flake irradiated with 15 different He^+ doses. Each region was irradiated with twice the dose of the previous region, starting with a dose of $1.00 \pm 0.02 \times 10^{16}$ He^+ cm^{-2} at region 1. Regions 9 ($2.56 \pm 0.02 \times 10^{18}$ He^+ cm^{-2}) and above were milled. (b) Concentration of Mo and S for different He^+ doses as extracted from EDX analysis. The error bars were obtained by the fitting of EDX data.

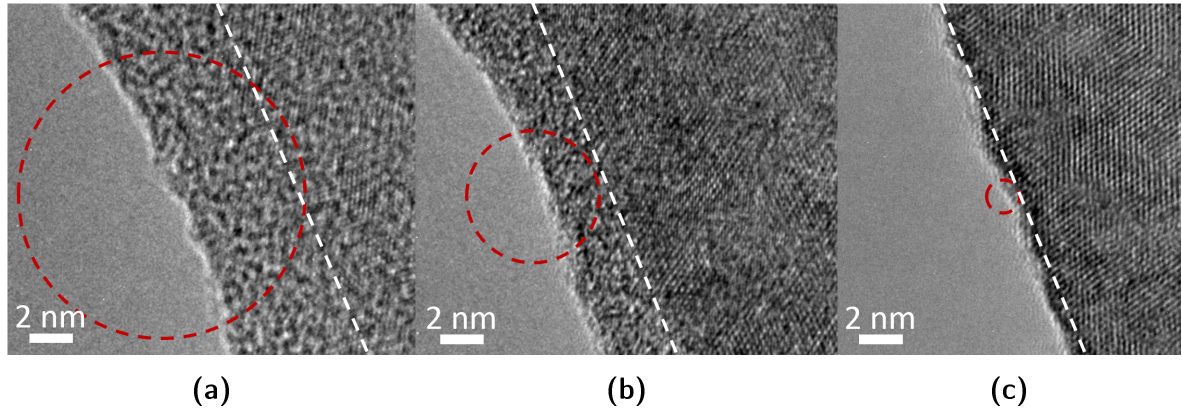

Figure 6.8: HRTEM images of the edges of three regions in the same freestanding MoS_2 flake milled with three different probe sizes. Edges milled with 12 ± 1(a), 5.9 ± 0.7(b), and 1.7 ± 0.2 nm (c) He^+ probes, respectively. The probe size is indicated by the red dashed circles overlaid on each image. The white dashed lines approximately show the edge of the amorphous region and agree well with the simulated values for the damage extension.

6.3 Nanostructure Fabrication

For few-layer samples of MoS_2, the interaction volume can be approximated to an interaction area. In this case, the He^+ probe size plays a crucial role on the lateral damage extension and crystal structure of milled nanosystems. An experiment was designed in order to better understand the relationship between the probe size and lateral damage extension in the material. This enables control of the width of the amorphous edge region.

As an example, defocus was used to adjust the probe size to 12 ± 1, 5.9 ± 0.7, and 1.7 ± 0.2 nm (details on the probe size measurement can be found in appendix E). In figure 6.8, three different edges were fabricated on a mechanically exfoliated, freestanding MoS_2 flake. Each edge was fabricated with a different probe size. Each probe delivered the same dose of $1.90 \pm 0.04 \times 10^{18}$ He^+ cm^{-2}. The structure of each edge was imaged in high-resolution TEM. Figure 6.8 (a)-(c) corresponds to the ~12, ~5.9, and ~1.7 nm probe sizes, respectively. The lattice structure was not affected at a distance (white line) from the edge which is approximately equal to the probe

size (red circle). The distributions of He^+ ions for the three different probe sizes used in the experiment were simulated. During imaging and milling, the He^+ beam is moved from pixel to pixel in a raster scan. An array of Gaussian distributions was simulated in order to account for beam overlap during scanning (see figure 6.11). The milled MoS_2 edge was assumed to be found where the dose drops below $1.30 \pm 0.03 \times 10^{18}$ He^+ cm^{-2}; a dose below this value was found experimentally to produce extensive damage but not complete milling. The point at which the crystal structure was assumed to remain intact was where the ion dose drops below $1.00 \pm 0.02 \times 10^{17}$ He^+ cm^{-2}, as determined by Raman spectroscopy. Our simulation predicts an amorphous region that extends 7, 3.5, and 1.0 nm for the 12 ± 1, 5.9 ± 0.7, and 1.7 ± 0.2 nm probes, respectively. The simulation data corresponds well with the probe radii (half the FWHM). It is illustrated in figure 6.11.

Further analysis of the extension of the amorphous region from the milled edges was done using the ratio of spots in local FFTs from the TEM images as shown in figure 6.9. The extension of the He^+ dose from the simulation was plotted as red squares. (a), (b) and (c) correspond to probe sizes of 1.7, 6 and 12 nm respectively. In each figure the higher dose is on the right, where milling of the sample occurs. The black data points correspond to the intensity ratio of the direct beam to one of the surrounding FFT spots. This was used as a measure of the changing crystallinity at different distances from the edge. A lower value corresponds to better crystallinity. Each FFT was acquired from a 2 nm *times* 2 nm area. Ten were acquired for each distance and averaged. The uncertainty graphed is the standard deviation. Due to limitations of field of view and magnification in TEM, only 7-10 points could be acquired in proximity to each edge. The x-axes are overlaid, the y-axes are scaled for best fit. The simulation and experimental data are in good agreement. A smaller extension of amorphisation is achieved by using a smaller probe size. This confines the He^+ ions within a smaller region and limits the extension of damage. Since the simulation simply considers the geometric profile of the probe, the good agreement demonstrates that fabrication precision in 2D materials is determined by the probe size and the extension of the interaction volume in 2D materials is negligible.

With the profound importance of the probe size (1.0 ± 0.5 nm) and minimising the He^+ dose ($3.10 \pm 0.06 \times 10^{18}$ He^+ cm^{-2}) now understood, a few-layer (4-5L)

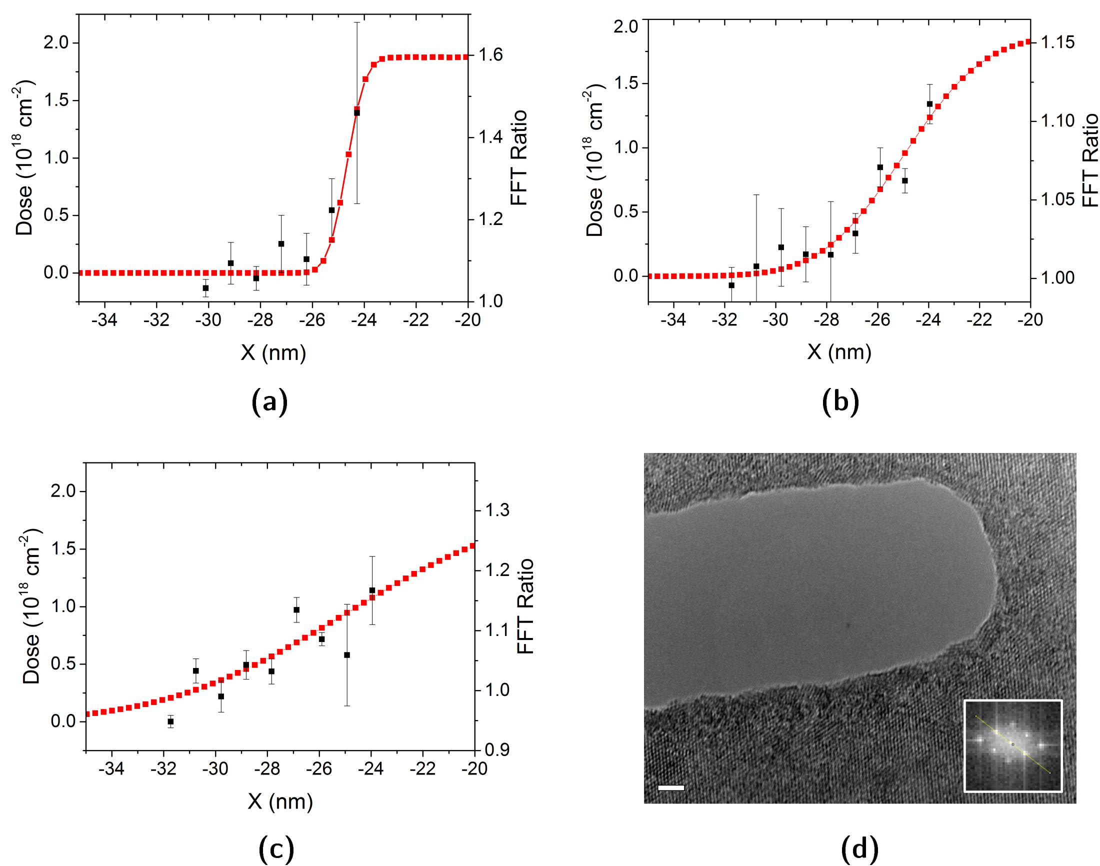

Figure 6.9: Graph of simulated ion distribution at Nanostructure edges with ratio of FFTs. The red data points show the extension of the He^{+} dose from the simulation. The black data points represent the ratio of spots in local FFTs taken periodically from the milled edge out towards pristine material. (a), (b) and (c) correspond to He^{+} probe sizes of 1.7, 6 and 12 nm respectively. (d) shows a feature milled with the 1.7 nm probe size with an inset of a local FFT acquired far from the edges of the feature. The FFT has a yellow line indicating the spots measured in *imageJ* where the values were extracted from. Uncertainties are the standard deviation of three measurements.

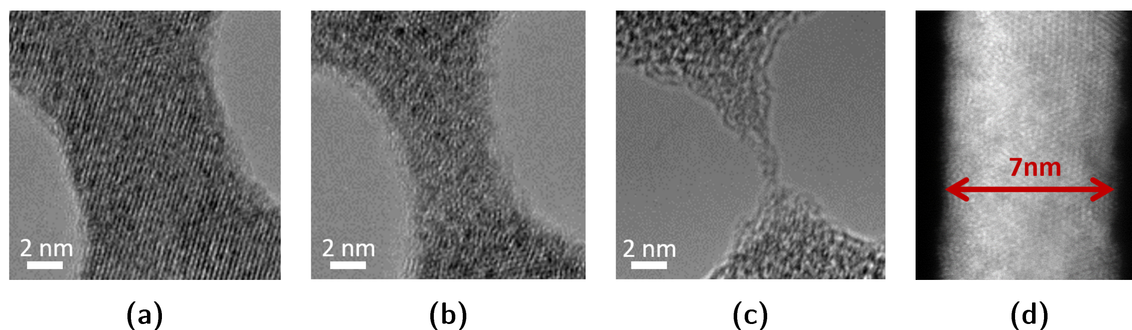

Figure 6.10: TEM images of He^{+} fabricated few layer freestanding nanoribbons in MoS_2. (a) a 9 nm wide crystalline MoS_2 nanoribbon, (b) a 5 nm wide amorphous MoS_2 nanoribbon, (c) an amorphous MoS_2 nanoribbon of 1 nm width at its minimum. (d) A STEM image of a 7 nm wide crystalline MoS_2 nanoribbon.

MoS_2 flake was selected and nanoribbons were fabricated. In figure 6.10(a), a 9 nm wide ribbon is shown. The well-defined crystal lattice fringes span across the whole ribbon, demonstrating that crystal structure structure of the MoS_2 remains entirely intact. In figure 6.10(b), a 5 nm wide ribbon with an amorphous structure can be seen. The width of the narrowest structure that can be reproduced consistently is less than 1 nm, though the structure is no longer crystalline MoS_2, figure 6.10(c).

The narrowest crystalline nanoribbon was 7 nm wide as shown in figure 6.10(d). MoS_2 ribbons are theoretically stable down to widths of ~1 nm [17]. It is speculated that a heating effect may be occurring during milling, which might destabilize ribbons narrower than 7 nm [214]. Future work will aim to address this question. The edges of these crystalline ribbons exhibit well-defined lattice configuration, indicating a sub-nanometre precision of structuring.

6.4 Electrical Characterisation

To investigate the effects of structure, stoichiometry, and geometry changes on the transport properties of an MoS_2 flake, electrical measurements were performed (with the assistance of Dr. Yangbo Zhou, TCD). Mechanically exfoliated bilayer MoS_2 on a 300 nm SiO_2/Si substrate was used for these experiments (determined by optical con-

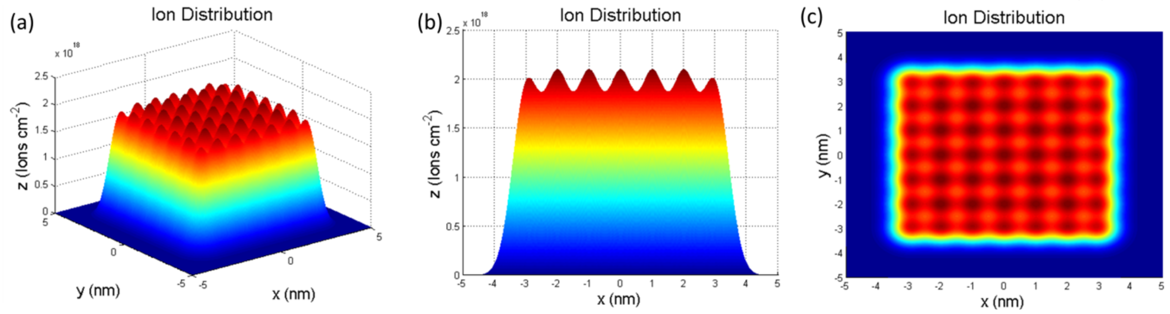

Figure 6.11: Simulation of the distribution of ion dose produced by a Gaussian array. Simulated array is composed of 7 × 7 pixels, spaced by 1 nm in each direction with an area dose of 2×10^{19} He^{+} cm^{-2} and a probe FWHM of 1 nm (a) Diagonal, (b) side and (c) plan views are shown.

trast methods). A MoS_2 transistor device was prepared using electron beam lithography (EBL) and the film deposition of 5 nm Ti and 45 nm Au layers. The electrical measurements were carried out using an *Agilent B2912A* dual channel sourcemeter with a nanomanipulator system (*Imina technologies miBots*) for electrical contacts. The He^{+} irradiated devices were measured in ambient conditions while the ribbon devices were measured in a SEM vacuum chamber (base pressure of 300 μPa). In figure 6.12(a), the resistivity evolution of mechanically exfoliated bilayer MoS_2 as a function of He^{+} dose was plotted, which shows four distinct stages. In the first stage, the resistivity decreased with the increasing dose and dropped by 28% at a dose of $1.00 \pm 0.02 \times 10^{14}$ He^{+} cm^{-2}. The second stage shows a dramatic increase in resistivity (by 5 orders of magnitude) as the dose increased from 10^{14} to 10^{15} He^{+} cm^{-2}. As the dose further increased to 10^{17} He^{+} cm^{-2}, the resistivity drastically decreased, recovered its initial value of the intact sample (10^{6} Ω), and decreased to a lower value (10^{5} Ω, 1 order of magnitude smaller than the initial value). In the last stage, the resistivity increased sharply to $10^{1}1$ Ω, as the dose increased to 10^{18} He^{+} cm^{-2}. To understand the change in the resistivity, I-V characteristics were measured, see figure 6.12(a). The pristine MoS_2 flake exhibited a nonlinear current-voltage response (red I-V response curve in figure 6.12(b)), revealing the semiconducting nature of the pristine MoS_2. The semiconducting behaviour of the irradiated MoS_2 flake was well

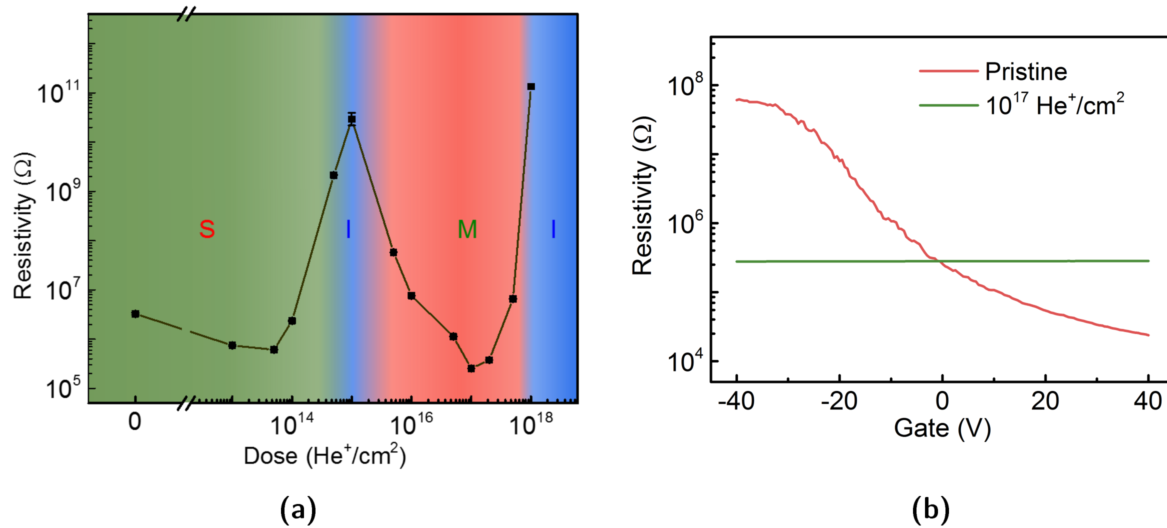

Figure 6.12: Electrical characterization of He^{+} modified devices. (a) Double log plot of electrical resistivity versus He^{+} dose for a substrate supported, mechanically exfoliated bilayer MoS_2 flake. The letters S, I, and M correspond to regions with semiconducting, insulating, and metallic-like behaviour, respectively.
(b) Resistivity measurement as a function of gate bias. The resistivity of the pristine sample (dashed red line) was widely tunable. The sample irradiated with 10^{17} He^{+} cm^{-2} showed little gate response (solid green line).

maintained in the first stage of beam irradiation, while the high resistivity indicates that the MoS_2 flake has been tuned from a semiconductor to an insulator (blue I-V response curve in figure 6.13) in the second stage. For irradiation doses higher than 10^{15} He^+ cm^{-2} (the third stage) a linear current-voltage response (green curve in figure 6.13) was observed. Gate bias measurements were conducted in order to further investigate this behaviour. Pristine MoS_2 showed a semiconducting behaviour with electron doping. The resistivity was tuned over 3 orders of magnitude by applying a back gate from -40 V to +40 V. The resistivity of MoS_2 irradiated with a dose of 10^{17} He^+ cm^{-2} could only be tuned ~3% when applying a back gate from -40 V to +40 V. The linear I-V characteristic, together with the greatly reduced and gate-independent resistivity, indicates that the MoS_2 irradiated with 10^{17} He^+ cm^{-2} was modified to metallic-like behaviour. The decrease in resistance of just one order of magnitude observed between the semiconducting to metallic-like MoS_2 was also reported in the semiconductor to metal phase transition process that occurs in other binary compound transition metals, such as molybdenum telluride ($MoTe_2$) [215] and iron disilicide ($FeSi_2$) [216]. Doses above 10^{17} He^+ cm^{-2} (the fourth stage) increased the flake resistivity while maintaining its metallic behaviour. At a very high irradiation dose of 10^{18} He^+ cm^{-2}, the flake behaved as an insulator again (resistivity >1011 Ω). The morphology modification introduced in previous sections can help to clarify the observed electrical tuning. A He^+ dose on a freestanding sample is expected to have effects about an order of magnitude lesser than on-substrate as discussed in chapter 5. For example, as the EDX was done on a freestanding sample it would be expected that the change in stoichiometry observed at 10^{18} He^+ cm^{-2} would occur at a dose closer to 10^{17} He^+ cm^{-2} for a sample on a substrate. The first stage of irradiation figure 6.12(a) introduced structural defects, while keeping the crystal structure. The structural defects act as dopants to the MoS_2 lattice and cause the decrease in the resistance [115]. This semiconductor-to-insulator transition in the second stage can be be explained as the formation of disordered domains in the amorphized MoS_2 flake [18]. The metallic-like behaviour of this sample in the third stage is most likely due to the preferential removal of sulphur and increased proportion of molybdenum. It has been reported that the existence of these sulphur vacancies can result in the appearance of a midgap state in the band gap of MoS_2 [217, 218] forming an elec-

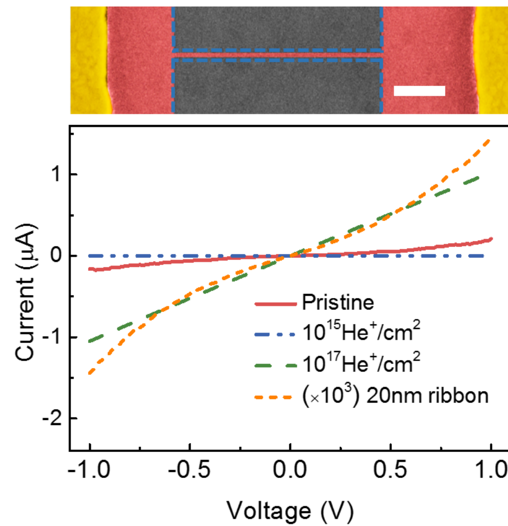

Figure 6.13: Electrical characterization of He^+ manufactured 20 nm nanoribbon. (Top) a 20 nm wide, electrically contacted, MoS_2 nanoribbon. The ribbon is shown with red false colouring indicating the measured region, and the gold electrodes are also coloured. The blue dashed line shows the isolating cut made with the He^+ beam. Scale bar is 500 nm. (Bottom) Current-voltage plots for the indicated doses as well as for the 20 nm wide MoS_2 nanoribbon. All of the results were measured at 0 back gate voltage.

tronic channel and improving the conductivity of MoS_2. The increase of resistance in the last stage can be attributed to the removal of MoS_2 due to excessive milling effects. It is noted that while other methods have been used to produce insulating MoS_2, [219, 220] the observed transition from insulator to metal-like behaviour has not been reported. It is possible that other atomic species, for example, carbon, were incorporated into our sample to passivate the sulphur vacancies, resulting in the metallic-like behaviour observed. More experiments are required to further characterize the metallic-like behaviour observed here (such as temperature dependence of the resistance).

The substrate supported MoS_2 can be milled into nanoscale geometries such as a ribbon with a width below 20 nm (as in the top of figure 6.12(a)). The fabricated MoS_2 nanoribbon had a nonlinear current-voltage response (orange curve in figure 6.12(a)), it therefore still exhibited a semiconducting behaviour. In order to control the electronic and magnetic properties of MoS_2 that occur due to quantum confinement, the ribbon width must be reduced by another order of magnitude [121].

6.5 Summary

In summary, noble gas ion-based patterning techniques can provide sub-nanometre scale precision milling for 2D materials with a scalability not previously practical in electron or ion-based milling. It has been shown that the structure, composition, geometry, and material properties of MoS_2 can be manipulated and tailored using He^+ irradiation. This was achieved by controlling the ion dose and the irradiated area. With a ~1nm He^+ probe, pristine nanoribbons of MoS_2 with sub-10 nm widths were fabricated. This technique can be adjusted for a range of 2D material systems such as those produced by Coleman et al. [221] in order to fabricate nanostructures whose shape, orientation, crystal structure, and stoichiometry can be modified. This will result in the production of novel nanostructures with tunable properties for a wide range of device applications.

Chapter 7

Ion Moderated Oxidation of MoS_2

In the previous chapters, ion irradiation has been demonstrated in the precise defect-engineering of 2D materials. The effects of these defects on physical characteristics have been investigated and discussed. In this chapter, this knowledge is extended by exploring the effects of ion beam-induced defects on the chemical behaviour of MoS_2, specifically its oxidation in air.

A simple, high throughput technique for the selective patterning of sheets of MoS_2 is presented. In this work, chosen regions of MoS_2 were activated for oxidative reaction by the application of low doses of He^+ at 30 keV in a GIM. Raman spectroscopy, OM and SEM were used to characterise both the etched features and the remaining material. It has been found that the application of He^+ (at doses of the order of $\sim 10^{14}$ He^+ cm^{-2}) introduce enough defects to MoS_2 that the irradiated regions are etched preferentially. This is achieved efficiently due to the low required dose and precisely due to the instrument resolution. No residual oxides of molybdenum could be detected in the etched regions suggesting the complete sublimation of MoO_x.

7.1 Ion Dose Dependency

A schematic of a representative ion-moderated etching experiment is shown in figure 7.1. MoS_2 was prepared by collaborators (M. O'Brien and G. Duesberg, TCD) using a CVD technique as in the previous chapter. The thickness was checked using Raman spectroscopy (532 nm, separation of A'_1 and E^1_{2g} peaks of 22.5 cm^{-1}) and

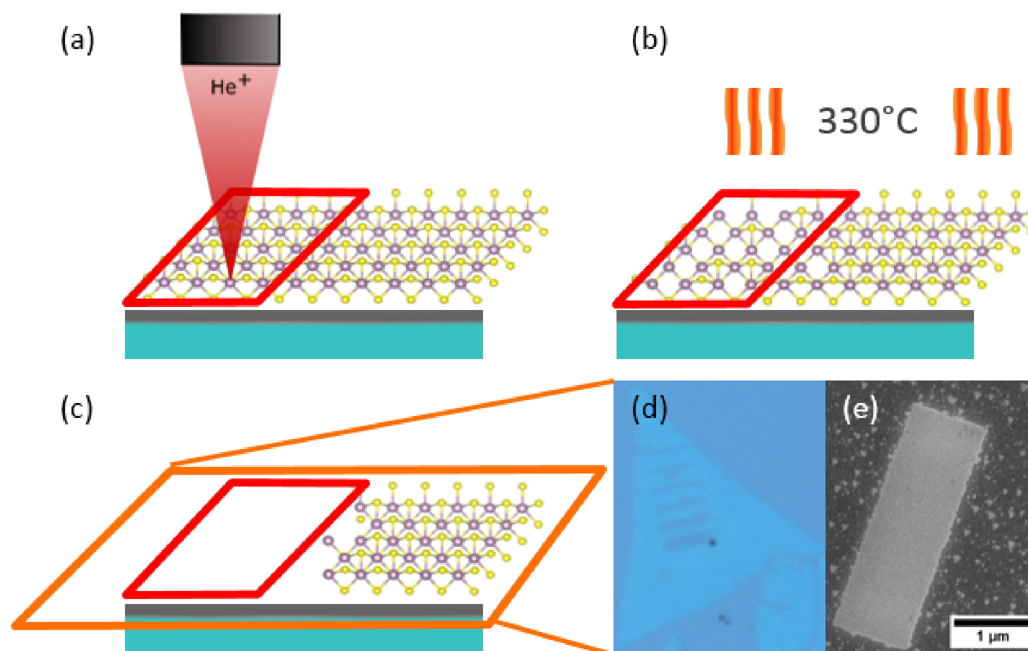

Figure 7.1: Outline of a typical oxidative etching experiment. (a) shows the He^+ beam incident on a rectangular region of CVD grown film of MoS_2. (b) shows He^+ irradiated MoS_2 with S vacancy defects introduced by the beam. (c) shows the same irradiated region, now etched after heating to 330°C. (d) is an optical micrograph showing an array of etched rectangles of decreasing width going upwards on a triangle of MoS_2. (e) is a SEM micrograph of one such etched region.

found to be bilayer. The sample was then loaded into the *Zeiss ORION Nanofab* microscope and imaged with low doses of He^+ in order to minimise damage. Imaging doses did not exceed 2×10^{11} He^+ cm^{-2} which has negligible effects on the sample [37]. An array of 5×5 μm squares was irradiated with increasing doses as in figure 7.2. The squares were irradiated with a beam current of 4.2 pA and a beam energy of 30 keV. The dwell time and number of repeats were varied to ensure that the desired dose was delivered. This allowed the ion dose dependency of the oxidative etching of bilayer MoS_2 to be investigated.

Samples were loaded on a glass slide into the middle of a quartz heating tube in an *MTI Multi-Position GSL-1100X-NT-UL-LD Tube Furnace*. The furnace was then sealed containing only air at atmospheric pressure and without any gas flow. The temperature was raised to the desired etching temperature at a rate in the range of 10 ± 2°C min^{-1}. The sample was heated to a maximum temperature of 330°C at which it was held for 50 minutes. These time and temperature values are typical of or similar to many of the papers mentioned in section 3.9 for the partial etching of ~2-5 layers of MoS_2.

After being allowed to cool to room temperature (RT) naturally, the sample was imaged using OM to confirm which doses had been etched. The minimum dose which resulted in the complete etching of a 5×5 μm bilayer region of MoS_2 was found to be 1×10^{14} He^+ cm^{-2} although some regions with doses up to 4×10^{14} He^+ cm^{-2} were not fully etched. Doses above this were always sufficient to remove all material in a region. In addition, when the heating step was repeated for a further 50 minutes under the same conditions, even the lowest dose (5×10^{13} He^+ cm^{-2}) region was almost completely etched. This dose is below that normally required to remove material by direct ion milling by about 4-5 orders of magnitude. It was also less than the dose required for amorphisation or detectable change in stoichiometry by 2 to 4 orders of magnitude [37].

The same experiment was repeated with a different sample of MoS_2. This sample was prepared by mechanical exfoliation and had a thickness of ~5-10 L (blue-gray colour in OM). However, no oxidation-induced etching was detectable. This is attributed to surface contamination caused by the sticky tape method which may have protected the MoS_2 from oxygen species. This is detailed in appendix F. Some

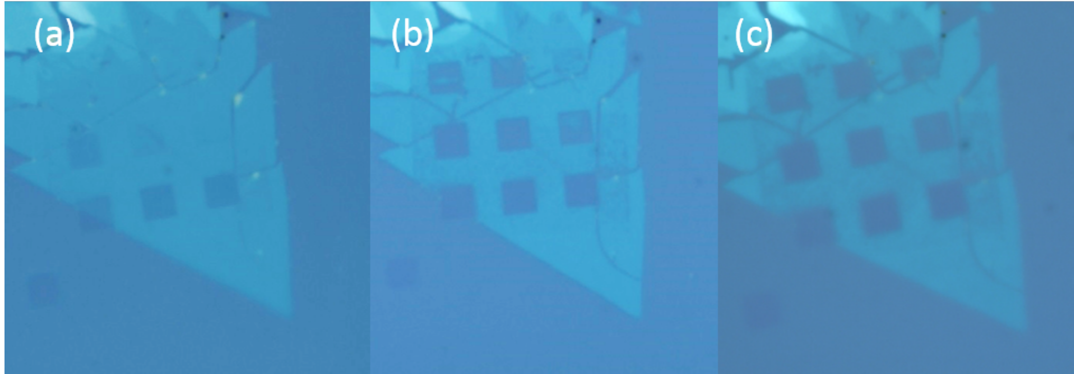

Figure 7.2: Ion dose dependency of oxidative etching of MoS_2. (a) An optical image of 5×5 μm squares of MoS_2 irradiated with increasing dose from right to left and top to bottom (1×10^{13}, 5×10^{13}, 1×10^{14}, 5×10^{14}, 1×10^{15}, 5×10^{15}, 1×10^{16}, 5×10^{16} and 1×10^{17} He^{+} cm^{-2}). (b) The same region after heating for 50 minutes at 330°C. (c) The same region after heating for 50 minutes a second time.

other experiments performed with high aspect ratio irradiation regions caused the production of meshes as discussed in appendix G.

7.2 Expanding the Oxidation Model

Another sample of MoS_2 was prepared by the same CVD process as before and this time an array of rectangles was irradiated in a monolayer part of the sample. An outline of this pattern is presented in figure 7.3(e), a low dose GIM image in which the irradiated patterns are overlaid. Within each row, the designed width decreased from left to right as follows: 1000, 500, 250, 125 and 75 nm. Within each column the dose increased from top to bottom as follows: (5×10^{13}, 1×10^{14}, 5×10^{14}, 1×10^{15}, 5×10^{15}, 1×10^{16} He^{+} cm^{-2}).

The sample was imaged by SEM after irradiation and then after heating to 300°C and so on in 5°C increments up to 335°C. Each heating step was for 50 minutes and otherwise similar to that described previously. A field emission SEM (*Zeiss Supra*, *Zeiss Microscopy GmbH*, Jena, Germany) was used to image the sample. A TTL

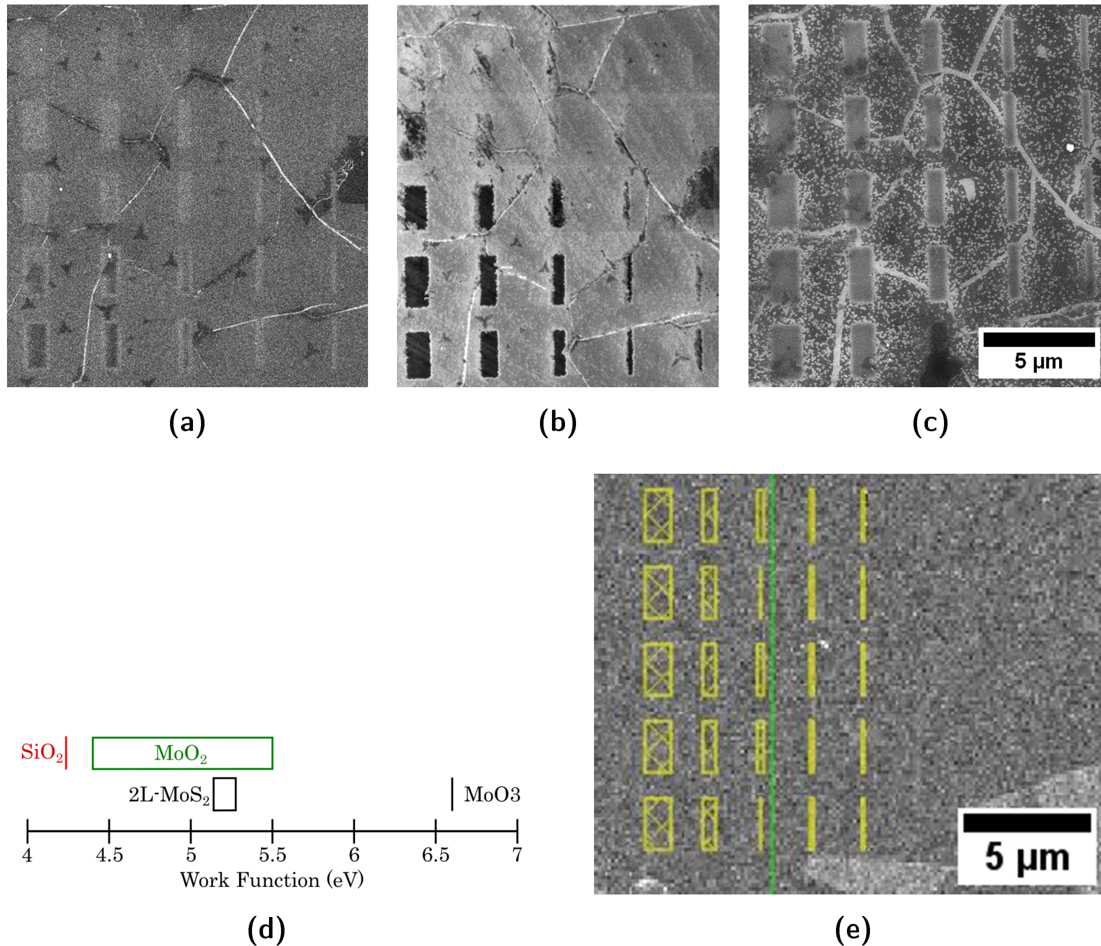

Figure 7.3: Scanning electron microscopy analysis of etching bilayer MoS_2 in a cumulative heating experiment. (a) to (c) is a selection of SEM micrographs at various steps of the cumulative heating process. (a) is after irradiation but before any heating. (b) is after heating to 305°C. (c) is after heating to 330°C. (d) shows the work functions of relevant materials. (e) is a low dose helium ion image overlaid with the patterns for irradiation.

or "inLens" detector is now common in SEM and was employed in this work for its particular sensitivity to the surface and work function of the specimen. Work function is the minimum energy required for the removal of an electron from a solid to a point in the vacuum immediately outside the solid surface. Low work function materials typically appear bright and high work function materials appear dark using an "inLens" detector. The imaging conditions were as follows: a 10 keV primary electron beam and a base brightness level of 49%.

A selection of the SEM micrographs are shown in figures 7.3(a) to 7.3(c). They demonstrate the progression from MoS_2 which has been irradiated to the complete etching of irradiated material after heating. Figure 7.3(a) shows low dose irradiated regions which are lighter than surrounding areas and higher dose regions which are slightly darker. After the 305°C step, figure 7.3(b) shows the same regions where those that received lower doses are still relatively unchanged and those that received higher doses are now very dark. Figure 7.3(c) shows the same regions once again after the 330°C step where all irradiated regions now appear to have been etched. The SEM images sampled in figures 7.3(a) to 7.3(c) are analysed in detail in figure 7.6(a).

The work function of monolayer MoS_2 has been reported to be approximately 4.0 eV in vacuum and up to 4.5 eV with adsorbed O_2 [222]. The work functions of molybdenum dioxide (MoO_2) and MoO_3 are ~4.4-5.5 eV and 6.6 eV respectively [223–225]. The work function of the SiO_2 substrate is 4.3 eV [193]. This range of work functions of possible materials in this system is represented in figure (d). This suggests that should a region of the specimen be observed to darken after heating, it will be due to the presence of oxygen species shifting the work function upward through either adsorption or oxidation. Once the MoO_3 has sublimed and the specimen region is deemed to have been etched, the contrast in each region will revert to that of the underlying SiO_2 substrate which should appear similar to the starting brightness of un-heated MoS_2[1].

The work function is expected to increase monotonically with the application of heat which makes it effectively impossible for SEM measurements to differentiate between oxidation and adsorption effects. Raman spectroscopy gives far more

[1]Albeit the substrate has also been modified somewhat by the ion beam which causes a slight darkening

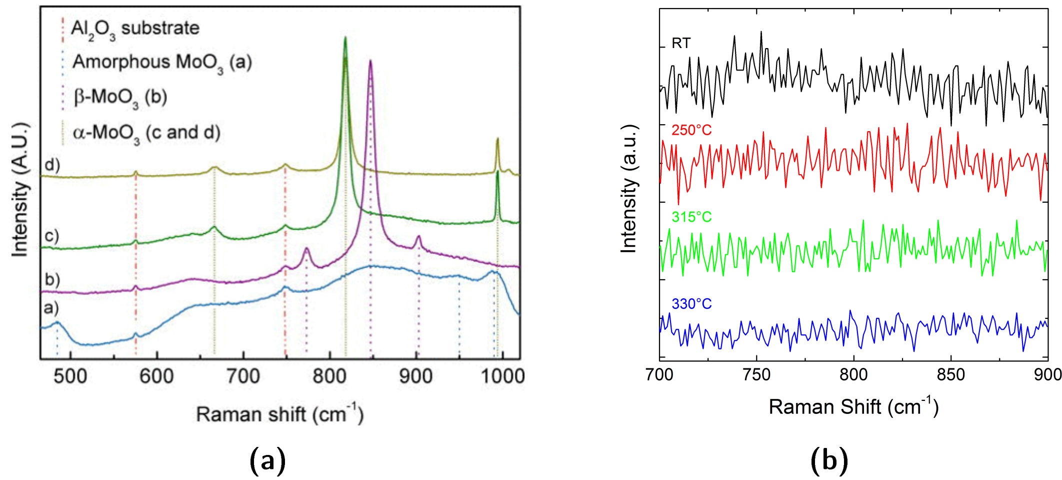

Figure 7.4: Searching for MoO_x in heated CVD MoS_2 using Raman spectroscopy (a) shows a reference Raman spectrum for MoO_3 [226]. (b) displays a selection of spectra showing that there is no evidence of MoO_2 or MoO_3 in MoS_2 irradiated with 5×10^{14} He^+ cm^{-2} at the four labelled temperatures.

material information to help clarify the effects of temperature on these processes. However, since Raman spectroscopy is relatively low throughput compared to SEM, it was decided to heat several arrays to the temperatures of 250, 300, 315 and 330°C rather than one array heated cumulatively. As such, the same arrays were repeated on four new samples for Raman spectroscopy. Although not directly comparable to the previous cumulative heating SEM experiment, the results obtained will provide evidence to clarify the following: the presence of MoO_x by searching for its characteristic peaks; effects on the remaining MoS_2 by studying the diminution, broadening and disappearance of the A_1' and E_{2g}^1 peaks; and in particular evidence in the Raman spectra for the alteration of the doping state of the heated MoS_2.

P-type doping is expected to be caused by oxygen species behaving as hole donors to adjacent MoS_2. With increased defect density the effects on the A_1' peak are expected to be upshifting and broadening. However, with increased p-type doping, upshifting and narrowing of the A_1' peak is expected. A narrowed A_1' peak in spite of the defects introduced by the ion beam would be convincing evidence of p-type doping.

Maps were acquired in a *WITec alpha 300R* with a 532 nm laser and a grating of 1800 lines/mm. There were 4 acquisition points per μm and each acquisition was for 0.06322 s. Spectra were acquired by averaging the spectra at each acquired point in the map which fell well inside the irradiated region. Spectra were also acquired from an adjacent non-irradiated region for reference (no closer than 1 μm to the border of the irradiated feature). Peaks in the Raman spectra were fitted with Gaussian functions using the fityk software package as these were found to fit the spectra most closely [172]. Error bars, where used and unless otherwise stated, are the fitting error as acquired from fityk which uses a weighted sum of squared residuals to measure agreement between the fit and the data [195]. This is chosen instead of the instrumental (1 cm^{-1}) error since the importance of the measurements is usually comparative rather than absolute, thus minimising the effects of systematic error.

The characteristic Raman spectra of MoO_3 in α, β and amorphous phases are shown in figure 7.4(a) [226]. The largest peak is at approximately 811 cm^{-1} for α and amorphous MoO_3 and at approximately 846 cm^{-1} for β MoO_3 [226, 227]. Not pictured is the Raman spectrum of MoO_2 in which a strong expected peak would be between 730 and 740 cm^{-1} [228, 229]. Figure 7.4 (b) shows spectra acquired in this experiment in the relevant range for these oxide peaks. Nothing beyond noise is evident beyond a possible small bump around 770 cm^{-1} in the RT sample which can be attributed to the $2E'$ mode of MoS_2. Since none of the listed peaks are evident, no indication of intermediate oxides can be presented here by Raman spectroscopy.

In figure 7.5 the evolution of the characteristic Raman peaks of MoS_2 with atmospheric heating temperature and He^+ dose is shown. Two sets of spectra are shown which are normalised to the Si peak at ~520 cm^{-1} (since this peak is expected to be only slightly affected by irradiation and not at all by heating). The first, figure 7.5(a) shows four non-irradiated MoS_2 regions from the samples subjected to different temperatures. With increasing temperature, a slight increase in peak separation (larger than both fitting and instrumental errors) is observed as well as a slight narrowing of the A_1' peak. Any change in intensity with respect to the Si peak is small and easily attributed to normal variation in sample. However, the second set of spectra in figure 7.5(b) is very different. This shows spectra acquired from MoS_2 irradiated at the moderate dose of 5×10^{14} He^+ cm^{-2}, again at four different temperatures.

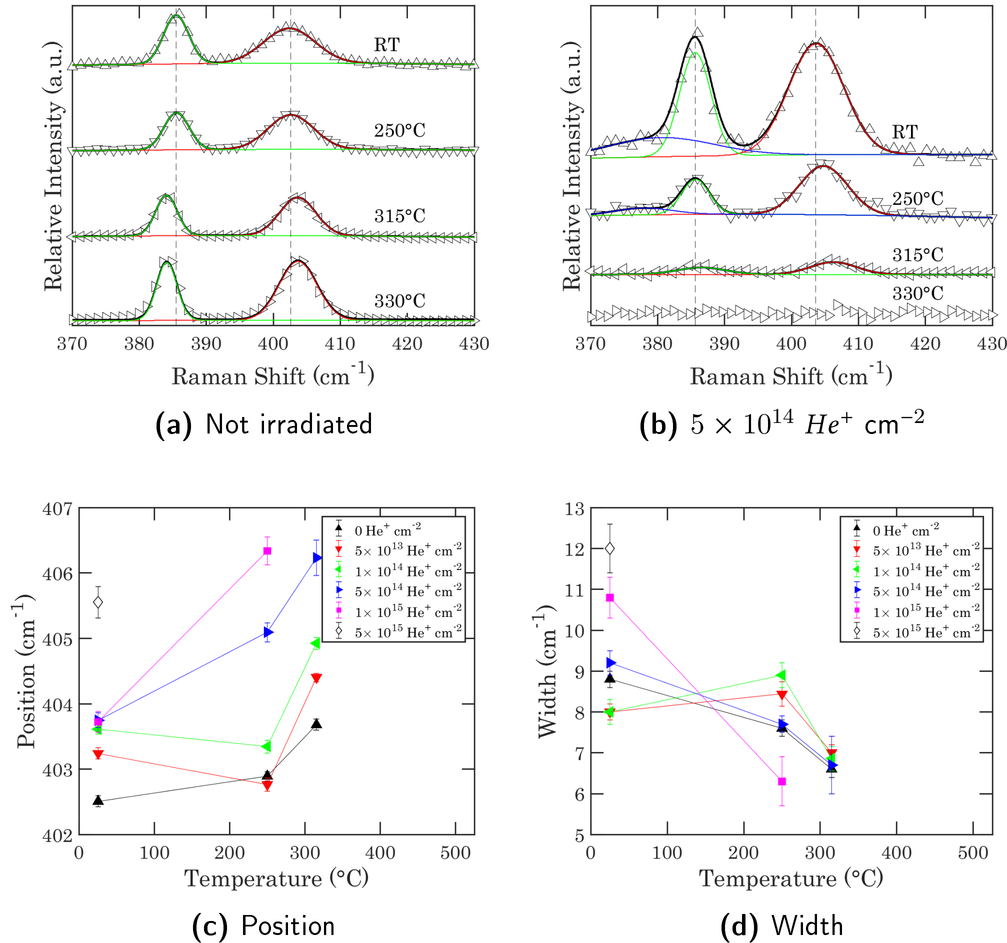

Figure 7.5: Expanding the etching model for monolayer CVD MoS_2 with Raman spectroscopy. (a) and (b) show the progression of Raman spectra with heating for non-irradiated MoS_2 and MoS_2 irradiated with a dose of 5×10^{14} He^+ cm^{-2} respectively. In the spectra, the black line is the fit to all of the data while the green, blue and red lines are fits to the E', E' shoulder and A_1' peaks respectively. The triangles represent individual data points. (c) is a graph of the position of the A_1' peak after heating to three temperatures for a variety of He^+ doses. (d) is a graph of the width of the A_1' peak after heating to three temperatures for a variety of He^+ doses. The error bars in both (c) and (d) are acquired from fitting.

The difference is striking as the intensity of these peaks drops sharply even at the lowest temperature and there are no recognisable peaks at 330°C.

An increase in defect density is expected after irradiation, and this lowers the barrier for oxidation as discussed in chapter 4. Therefore a greater increase in adsorbed oxygen is expected in irradiated rather than pristine MoS_2 after heating. It is important at this point to separate the effect of the initial irradiation from the effect of the heating. The frequency and width of the A_1' peak has been reported to be sensitive to electrostatic doping while the E' peak is essentially inert, being more sensitive to strain [104, 105, 135]. Since doping of the specimen is an expected outcome of the increased presence of oxygen, the evolution of the A_1' peak will now be explored in greater detail [105, 148]. A broadening and blue-shifting of the A_1' peak is expected with an increase in defect density after irradiation [28].

Meanwhile, Chakraborty et al. has demonstrated that n-type doping is indicated by broadening and red-shifting of the A_1' peak [105]. Conversely, narrowing and blue-shifting of the peak may therefore suggest p-type doping. Thus the strongest evidence from Raman spectroscopy of p-type doping would be a A_1' peak which is narrowing in spite of the increased defect density.

Figure 7.5(c) tracks the position of the A_1' peak with heating step. It is observed that without a heating step the lower doses cause little if any significant shift in the position of the A_1' peak, although a dose of 5×10^{15} He^+ cm^{-2} does show a large upward shift of more than 3 cm^{-1}. After the first heating step, to 250°C, the Raman spectra of this dose is too noisy to be fitted and now an ion dose of 5×10^{14} He^+ cm^{-2} is observed to cause a blue shift of more than 4 cm^{-1} compared to non-irradiated MoS_2. After the 315°C heating step, the highest doses have etched and all other doses are now upshifting in similar fashion. Figure 7.5(d) shows the evolution of the width of the A_1' peak with dose as a function of the heating step as before. In the case of width, the ion beam causes a consistent and large increase at RT. However, once heated to 250°C the width decreases substantially for the larger doses and even more so for all doses at 315°C. This is strongly suggestive of p-type doping introduced by oxygen content.

Stage	Temp	$\omega_{A'_1}$	$\Gamma_{A'_1}$	W	Regime
0	RT	A.D. ↑	H.D. ↑	H.D. ↑	Increased Defects
I	< 305°C	A.D. ↑	H.D. ↓	H.D. ↑	O_2 Adsorption at Defect Sites
II	305 – 320°C	A.D. ↑	A.D. ↓	A.D. ↑	O_2 Adsorption to Saturation
III	> 320°C	A.D. –	A.D. –	A.D. ↓	Oxidation

Table 7.1: Temperature dependent oxidation stages for mono- and bilayer MoS_2. A.D. means all doses, H.D. means high doses, $\omega_{A'_1}$ is the position of the A'_1 peak, $\Gamma_{A'_1}$ is the width of the A'_1 peak, W is the work function.

7.3 Defining Temperature Stages in the MoS_2 Oxidation Model

In order to infer the maximum possible information about the effects of ion dose and temperature, it is important to compare the results of both the SEM cumulative heating experiment and the Raman spectroscopy experiment. To assist with this the data from both experiments is presented in a new way in heat maps as in figure 7.6. This allows the identification of several discrete stages separated by their approximate temperature range. The key characteristics of these stages are presented in table 7.1. **Stage 0**, where only irradiation has occurred with no heating step, is characterised at high doses by changes consistent with an increased defect density: an A'_1 peak of increased position and width and an increased work function at high doses.

The label of **Stage I** is applied to a heating range of < 305°C. It is characterised by the decoupling of position and width of the A'_1 peak. The narrowing of the A'_1 peak and the sharply increased work function are unequivocal in describing a sample of MoS_2 with an increasing influence of oxygen species. This is strongly suggestive of p-type doping by contrast to the increased defect density of Stage 0. In stage 1, *oxygen adsorption* is expected to dominate since oxygen can adsorb to the MoS_2 surface more readily at higher temperatures as previously discussed in chapter 4. The effect is most clear for the regions which received a higher He^+ dose since it has been established that He^+ creates S vacancies and that S vacancies lower the barrier

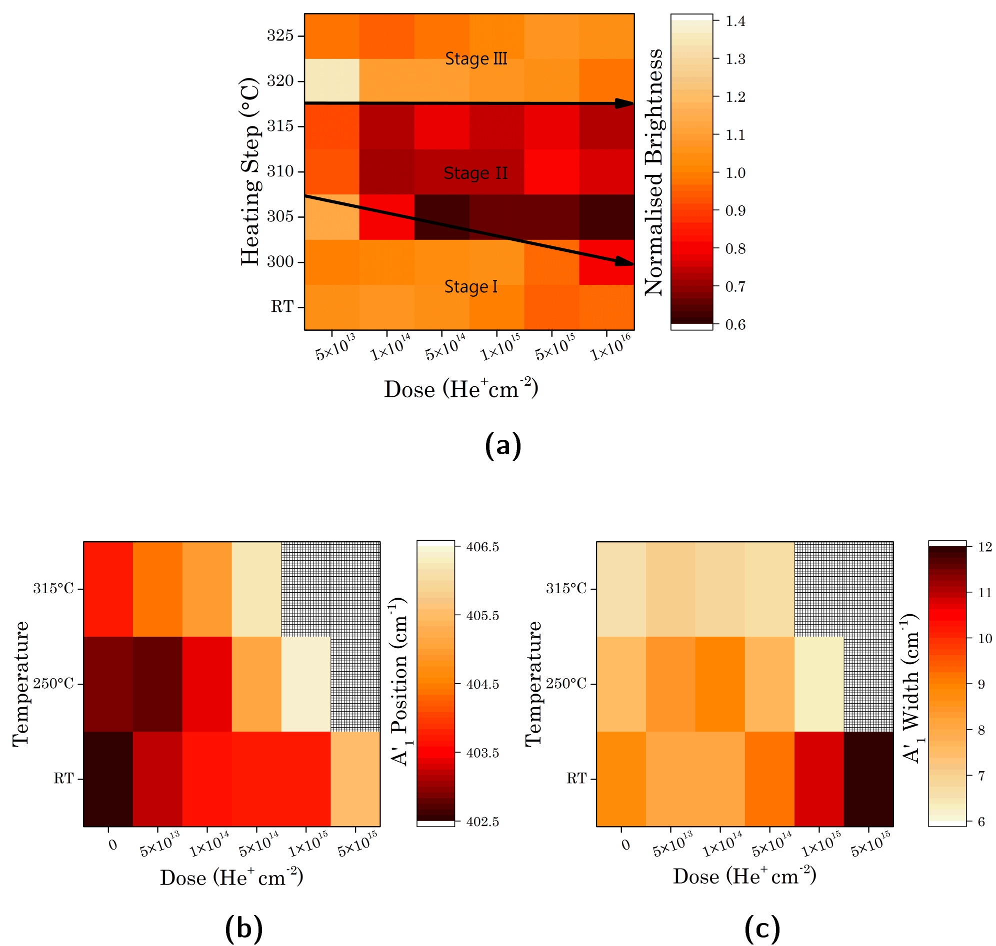

Figure 7.6: Heat maps of SEM brightness and A_1' peak position and width for bi-layer MoS_2. (a) shows normalised SEM brightness for regions corresponding to their heating step and irradiation dose. (b) and (c) show position and width of the A_1' peak respectively as a function of the heating temperature and ion dose.

for oxygen adsorption [37, 155].

Stage II is found to occur between the temperatures of 305°C and 320°C. It is notable that the A_1' peak of even non-irradiated and low dose MoS_2 is now strongly affected by this step. In addition, the change in work function is now much more intense. This is attributed here to a highly increased oxygen adsorption rate. It is suggested that Stage 1 may be dominated by adsorption of oxygen to highly defective regions/edges only. By contrast, stage II involves more widespread adsorption, perhaps approaching saturation for sufficient time/temperature.

Stage III occurs after the 320°C heating step. By this stage, it is observed in SEM that brightness is now very similar across almost all doses. It is also now very similar to the substrate[2]. In addition, no characteristic Raman spectra of MoS_2 or MoO_3 can be collected from here. This stage is therefore attributed to the near complete oxidation and sublimation of Mo species leaving behind only the SiO_2 substrate.

At some point above 315°C and below approximately 340°C, the distinction between irradiated and non-irradiated material begins to matter less as even non-irradiated MoS_2 begins to etch. This can be seen in the SEM image in figure 7.3(c). Here, curved lines of material near grain boundaries and many randomly positioned triangles at native defect sites are observed to have etched. This is also clear from Raman spectra results which show even the lowest doses having been fully etched after high temperature treatment. However, at the lower temperatures, the dose effect is crucial. It should be noted again that MoS_2 can hold 1.15×10^{15} adsorbed O atoms cm^{-2} and that it is largely doses within an order of magnitude or two of this that seem to really distinguish themselves from non-irradiated material in character at RT and lower heating steps.

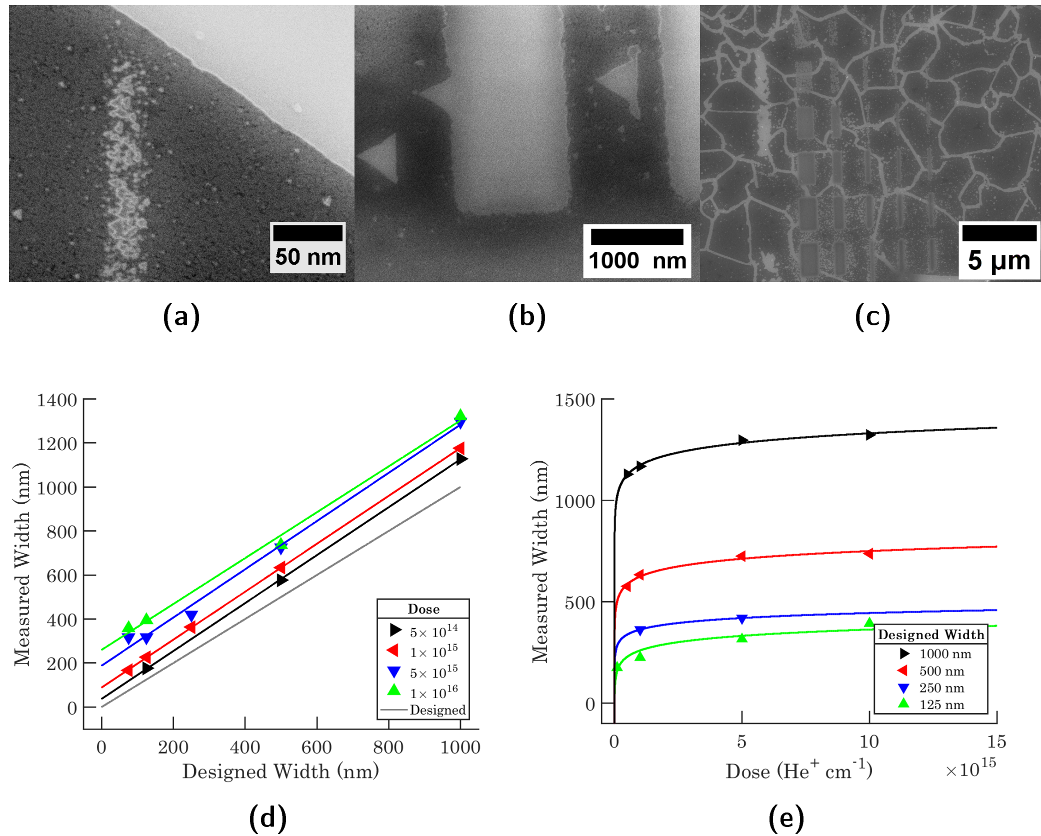

Figure 7.7: Edge roughness and etching range. The first three sub-figures were acquired using SEM. All show CVD-grown bilayer MoS_2 heated to 330°C for 50 minutes. (a) shows the top of a partially etched rectangle which was irradiated with 1×10^{16} He^{+} cm^{-2} in a 5 nm wide pattern. (b) shows more highly defined edges which were formed at the edge of a rectangle which was irradiated with 1×10^{16} He^{+} cm^{-2} in a 1000 nm pattern. (c) shows an irradiated array, the same as used in previous experiments. (d) is a graph of measured width against designed width for four different doses. The higher doses have created larger etched features. The grey line is the designed width. (e) is a graph of measured width against dose with a power law fit for a range of designed widths. It is constructed from measuring the width of the rectangles shown in (c).

7.4 Etching Range and Edge Definition

At this point, it is understood that etching is initiated at defect sites, whether native or introduced by the ion beam. However, as noted by Yamamoto et al., this only affects the density of etching sites and does not directly affect their size progression [148]. To use He^+ to moderate etching in a scalable fabrication process, the size of the etched features must be better understood. A dose-dependent discrepancy was observed between the size of the irradiated areas defined in the *ORION Nanofab* patterning software and the observed size of the etched regions in SEM and this was investigated further.

Figure 7.7(a) shows a partially etched region of width ~30 nm in spite of its designed width of 5 nm. This rectangle received a large dose of 1 $\times 10^{16}$ He^+ cm^{-2}. Rectangles of the same size irradiated with doses of the order 1 $\times 10^{14}$ He^+ cm^{-2} were not readily visible using SEM. Figure 7.7(b) shows the result of a pattern of the same dose but a much larger designed width, 1000 nm. The edges are observed to be very well defined. Its rectangular shape is only significantly disturbed by overlap with triangles etched at native defect sites. Triangles both overlapping and nearby can be seen in the image. The main array of irradiated/etched features used for analysis here is shown in figure 7.7(c). The irradiation parameters were the same as in the cumulative heating experiment although this array was only heated once to 330°C for 50 minutes. A SEM image of the etched array is shown in figure 7.7(c). Low doses and the narrowest widths resulted only in partial or non-detectable etching. The measured size of the rectangular irradiated regions which did etch were found to be dependent on both the dose and the designed width as shown in figure 7.7(e). The measured widths (W) seem to follow a power law in relation to the dose (D) of the form:

$$W = mln(D) + b \tag{7.1}$$

where m and b are fitting parameters. This assumes that other factors such as beam

[2] The region irradiated with the lowest dose after the 320°C step seems to be something of an outlier due to its high brightness. There are several possible explanations for this including that there may still be some residue of MoO_3/MoS_2 here which may be charging under the electron beam. In any case, it is removed fully by the 325°C step.

drift, beam width and scanning strategy factors such as dwell time and repeats are negligible as expected. The effect of increased dose was to widen the etched region, increase the visibility of the edges and to complete etching for narrower widths. The following model is suggested to explain the higher measured width. The helium ion irradiation introduces a low but chemically significant number of defects in the patterned region. To a lesser extent defects are also created beyond the defined area for two reasons: the beam spread effect over several nm discussed in chapter 6; and the excitement of secondary atoms in the substrate which spread over tens of nm. During the heating, reactions with available oxygen occur preferentially at defect sites. Given the distance range of the discrepancy, it is likely that the spread of excited secondary atoms is the most significant. Both effects could be reduced by using a lower ion dose as discussed in chapter 6. The exothermic nature of the oxidation reaction is also likely to lead to a higher local temperature near under-coordinated atoms. This is also a contributory factor to enhanced reaction rates in a range surrounding the etched/irradiated area. In any case the propagation of the edge into relatively non-damaged material causes a weakening of the local crystal structure meaning that larger than defined etched widths may to some extent be unavoidable if heating parameters to ensure the complete etching of the designed area are strictly required.

7.5 Summary

In this chapter, thermal etching observed in previous studies has been preferentially and overwhelmingly stimulated in selected discretionary regions thanks to a region-specific, low dose and high throughput irradiation with He^{+} at 30 keV. A range of other investigations were also performed. Ion irradiation has been successfully established as a high throughput tool for moderating the oxidation of FLM-MoS_2. At standard times and temperatures for the reaction in the literature, doses in order as low as 1×10^{14} He^{+} cm^{-2} showed a profound effect on oxidative etching rates. Previous methods have used oxidative etching for the doping and removal of MoS_2 but this is the first report of doing so while asserting spatial control. The oxidation model was considerably advanced including a breakdown of effects at different tem-

peratures using Raman spectroscopy and SEM. Strong evidence for p-type doping was provided, a much desired and elusive effect in MoS_2. Moreover, specific regions can be targeted for doping or removal at arbitrary locations while leaving other non-irradiated regions relatively untouched. This is a very high throughput process due to the low doses involved and it avoids the use of resists which are a leading source of contamination in 2D material based devices.

Chapter 8

Conclusion

In this thesis a range of gas ion beams have been used to precisely alter the geometry and properties of 2D materials. The beams of electrons or ions used can be focused to a nanometre scale and their combination of throughput, precision and resolution in nanofabrication is remarkable.

In this work, an electron beam was used to moderate the high resolution etching of graphene in a nitrogen environment. Nanopores were fabricated to a sub-5 nm scale quickly and precisely and the mechanism was studied extensively. Graphene defect-engineering was also performed over larger areas using a direct ion beam method in a GIM. He^+ and Ne^+ at 30 keV were both used for this, and their effects on defect density and size were studied using Raman spectroscopy models. A comparison of effects on supported and freestanding graphene by the ion beam yielded very important results for the future of ion-based device fabrication methods.

Defect-engineering methods were also expanded to include monolayer MoS_2, and the Raman spectra of several other layer numbers were also studied. This knowledge informed methods to efficiently fabricate nanostructures. The He^+ beam was thus used to create nanometre scale ribbons with 7 nm dimensions and pristine crystal structure. Modelling was used to map the milled, amorphous and pristine regions of sample surrounding the region selected for irradiation. Tuning of the stoichiometry of MoS_2 by ion beam due to the preferential sputtering of S atoms was also demonstrated. Tuning of the resistivity by ion dose was shown to be particularly interesting as a recovery in conductivity was demonstrated with the emergence of

metal-like conduction in a certain dose range.

The defect-engineering of MoS_2 using He^+ is well established in this work and it was subsequently used to investigate the effect of defects on chemical properties. Oxidation of MoS_2 has been demonstrated in the past to achieve much coveted p-type doping as well as thinning and etching. However, using ion irradiation methods this oxidation is now reported with unprecedented spatial control. The oxidation model has also been expanded upon with the behaviour of adsorbed oxygen species and molybdenum oxides clarified.

8.1 Future Work

The modification methods developed and expanded in this thesis could be expanded to a myriad of other materials. The use of energetic He^+ and Ne^+ irradiation for other materials to achieve similar modification of properties would be quite simple. On the other hand, the substitution of nitrogen in the electron beam-activated etching of graphene for oxygen would likely allow the same method to be applied to a range of TMDs including MoS_2.

The investigation of substrate and freestanding effects, both directly and on fabrication processes, should be expanded to non-monoatomic 2D materials. This could be performed simultaneously with a variation in layer number, and characterised by low frequency Raman spectroscopy to achieve the most information. The effects of ion irradiation and substrate on tribological properties are quite unexplored and worthy of further study, particularly given the promise of 2D material heterostructures.

The ion-moderated oxidation of MoS_2 could prove extremely useful if it can be used to create regions of p-type MoS_2 for the fabrication of devices. This remains uninvestigated by electrical measurement which should be pursued promptly.

Appendices

Appendix A

Identifying Suitable Samples in TMSEM

The flakes were imaged in a STEM mode in a *Zeiss Ultra* SEM. The TMSEM detector provides much more thickness contrast than any other SEM method (although it is not calibrated for layer differentiation), much better throughput than any TEM method and maintains high spatial resolution. Locations of interest were noted by taking images at a series of magnifications with respect to a reference point at the centre of the sample grid. This allowed the flakes to be located when transferred to the GIM and later the TEM.

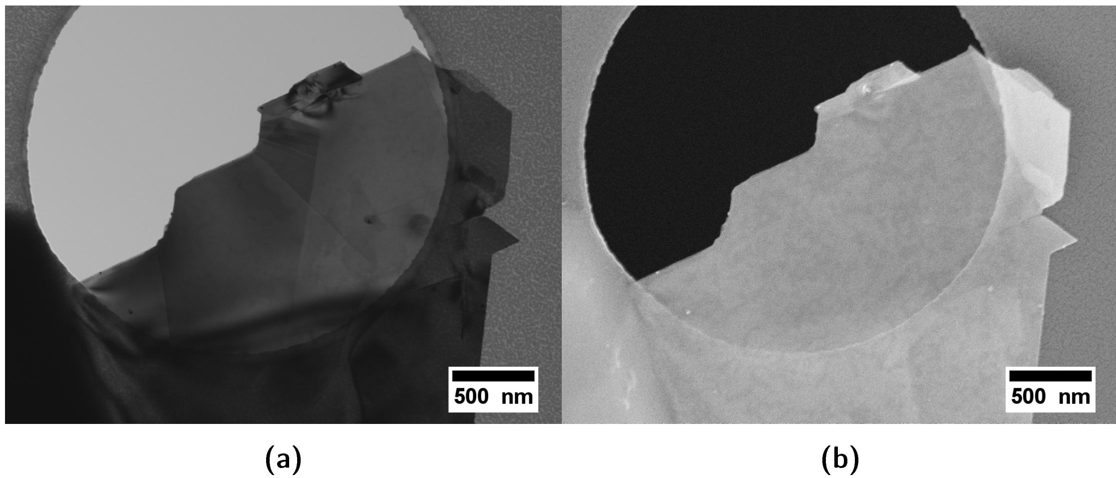

Figure A.1: Identifying suitable MoS_2 flakes for experiments in TMSEM. Images acquired in a *Zeiss Ultra* SEM at 20 kV. (a) shows an image acquired using the STEM detector. (b) shows an image acquired using the inLens or TTL detector.

Appendix B

Supplementary Information for Etching of Graphene by Nitrogen

The SEM images from which the data for figure 5.4 in the main manuscript were extracted are shown in figure B.1. Figure B.1(a) is the monolayer MoS_2 sample. Figure B.1(b) is the ten layer sample. The dwell times used to create each pore are shown above the pore. The scale of both images is the same (bars are 100 nm). The thickness of the samples used in figure 5.4 was confirmed by optical contrast. An Si wafer with 300 nm SiO_2 on the surface was used as the substrate. The optical image of the one and ten layer flakes is shown in figure B.2.

Temperature Effect

The effect of sample temperature on etching rate was investigated. Supplying thermal energy to the sample lowers the activation barrier for the etching reaction to occur, thereby increasing the rate of the reaction. Similarly if the sample were to be cooled the rate of the reaction would be slowed. A stage with a controllable temperature range from -25°C to +50°C was used to investigate the effect of temperature on the etching. The beam energy was set to 5 keV, the beam current was 150 pA, the nitrogen gas pressure was 380 mPa and the dwell time was 620 ns. The water cooled stage has more instability than a normal stage. The stage drifted quite significantly, at up to 80 nm/s. This drift rate prevented the use of a single point irradiation as

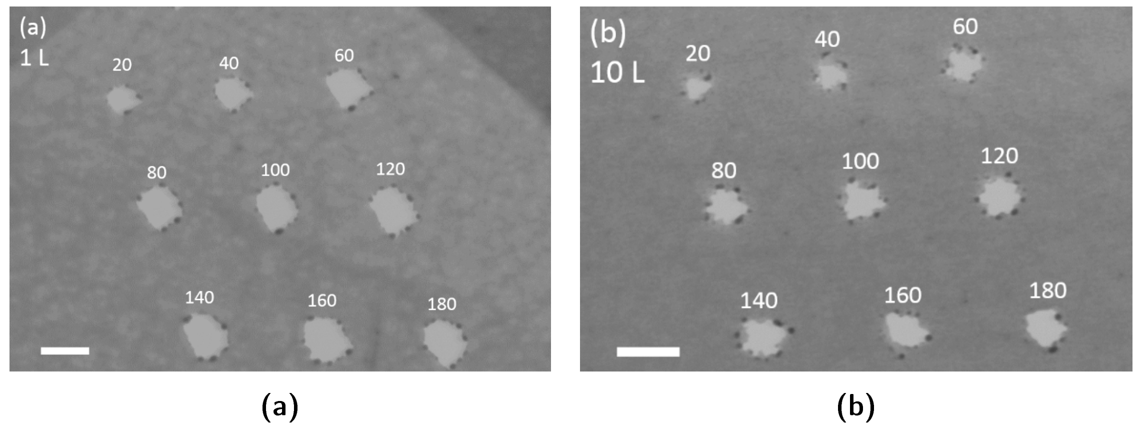

Figure B.1: (a) Monolayer graphene sample etched with nine different dwell times. (b) Ten layer graphene sample also etched with nine different dwell times. Scale bars are 100 nm.

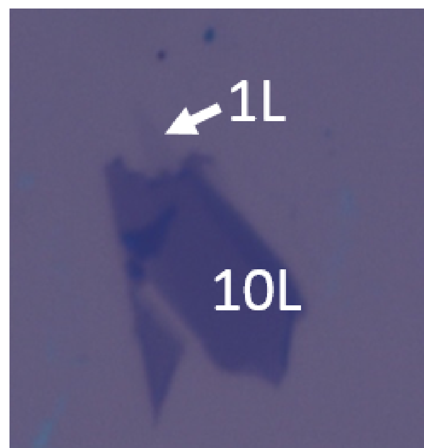

Figure B.2: Optical image of single and ten layer MoS_2 on a 300 nm SiO_2 layer on Si.

in the previous experiments. Instead an entire flake was irradiated in a raster scan for a total time of 10 min. One flake was irradiated at -25°C, another at +50°C. The total area irradiated in each experiment was 1.5×1.5 μm. The sample was then analysed using energy filtered TEM selecting the plasmon loss region (a 15 eV window centred at 25 eV). What we expected to observe were nanopores distributed across the surface, like those seen around the edges of figure 5.1(b) [191]. The flake irradiated at -25°C is shown before and after etching in figure B.3(a) and (b) respectively. The flake irradiated at +50°C is shown before and after etching in figure B.3(c) and (d) respectively. The before etching images in figure B.3(a) and (c) are SEM images. The after etching images in figure B.3(b) and (d) are plasmon energy filtered TEM images. It is clear from these images that the irradiation caused no observable etching effect.

The lack of etching observed can be attributed to the difference in the dose of electrons delivered to the sample. In a typical etching experiment a point on the sample with an area of ~80 nm^2 was irradiated. In this experiment the beam could not be confined to a point on the sample due to the drifting, resulting in an area of 2.25×10^6 nm^2 being irradiated by scanning the beam across the sample. Even with the 20 × increase in etching time used in this experiment the electron dose was still 1,430 times less than when a single point was irradiated. To deliver a dose which was observed to result in etching in the previous experiments to an area this size (using this beam current, beam energy and gas pressure) an irradiation time of ×10 days would be required. Dose rate may also play an important role, as has been established for Ga^+ FIB irradiation of materials [230]. Reduced drifting would allow the prolonged irradiation of a small area of material, thereby enabling a higher dose rate to be delivered to the region, as in our other experiments. A stage with a greater range of temperature control and more stability (to reduce drifting) would be required to further investigate the effect of temperature on the rate of etching.

Sizing Histogram

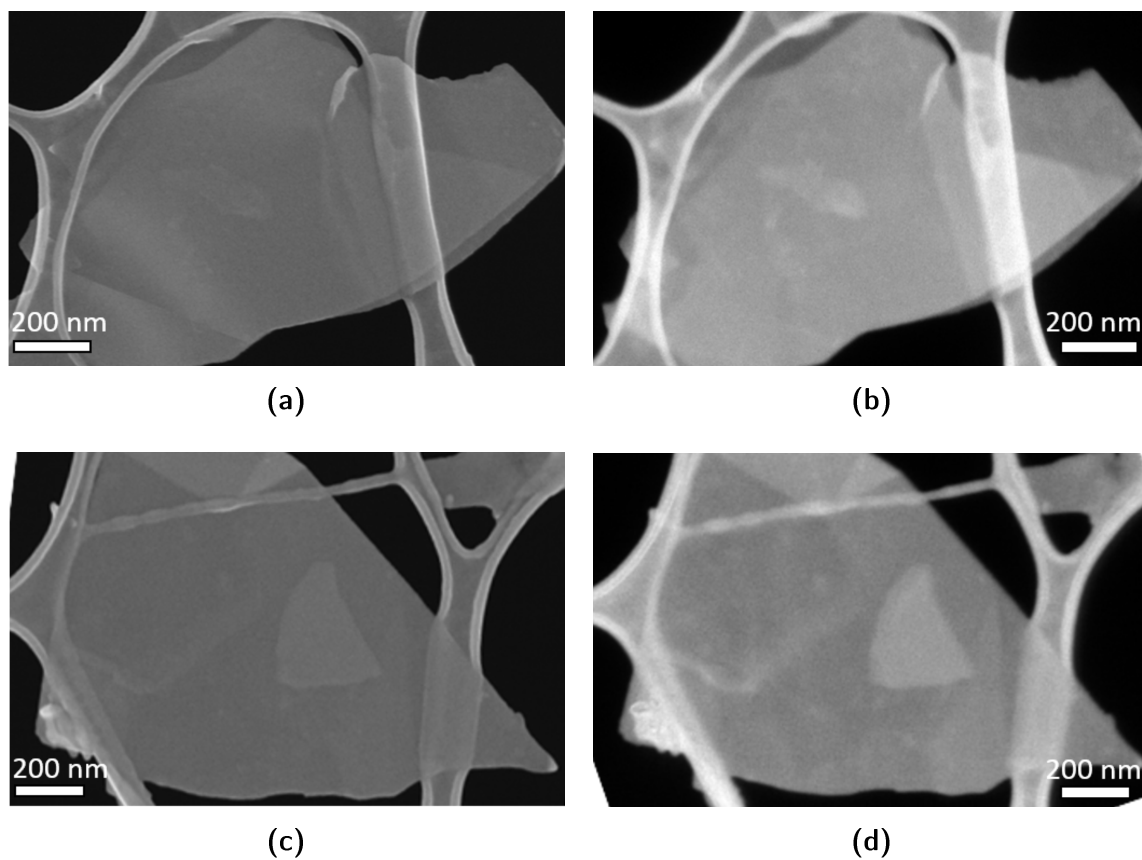

Figure B.3: Temperature effect of e-beam etching. (a) SEM image of a graphene flake. (b) The same flake imaged in plasmon energy filtered TEM after etching at -25°C. (c) SEM image of a graphene flake. (d) energy-filtered transmission electron microscopy (EFTEM) image of the same flake after etching at +50°C.

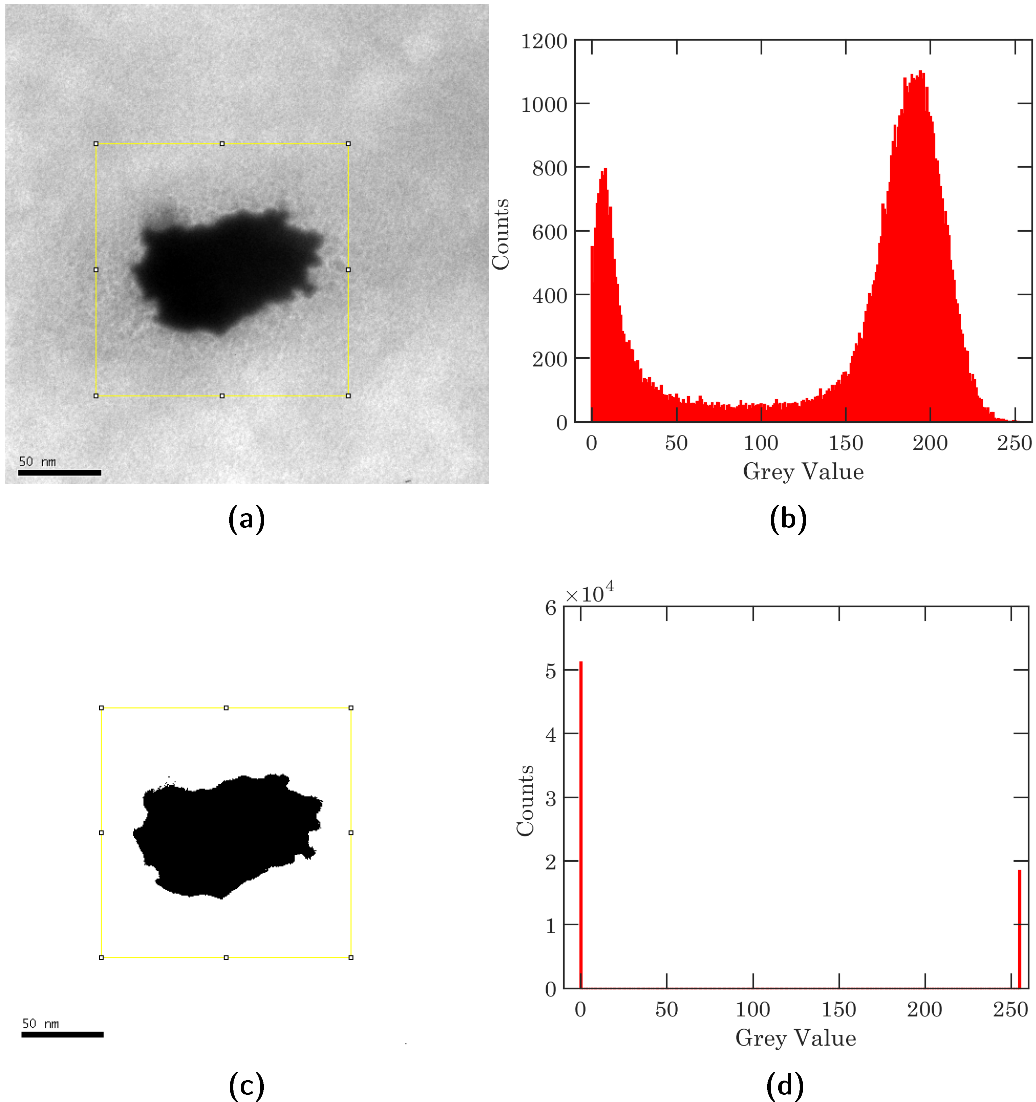

Figure B.4: Measuring nanopore sizes from TEM images with Imagej. (a) is a TEM image of a nanopore with a 150 nm × 150 nm box drawn around it in Imagej. (b) is a bimodal histogram of gray values extracted from the yellow box. (c) is (a) after applying a threshold in Imagej. (d) is the histogram of (c). The ratio of dark and bright counts allows the calculation of etched area.

Appendix C

Ion Beam Stability and Dose Uncertainty

This investigation was performed by Dr. Daniel Fox but is included here given its importance [37].

The beam current used for milling was adjusted to 1.0 pA by changing the spot size and the helium gas pressure. Precise values of beam current were recorded as "blanker current" in the saved .tiff file format of corresponding images and can be obtained by using the *Zeiss* software "*ALIS TIFF TAG Viewer*". An imaging sequence of 50 images in 10 minutes was acquired, which is larger than the time needed to pattern a nanostructure ($<$10 s). The measured beam current varied from 0.982 pA to 1.064 pA, with a most probable value of 1.02 ± 0.02 pA. The variation in current of the He^{+} beam is two orders smaller than its value, demonstrating its stability. The patterning dose can be precisely controlled with errors of about 2%.

Appendix D

Fitting the *LA(M)* Mode in Raman

The $LA(M)$ mode and surrounding peaks were fitted in similar fashion to that described by Mignuzzi et al. using Lorentzian distributions. Data in the approximate range of 120 to 270 cm^{-1} was included for fitting. An example is shown in figure D.1.

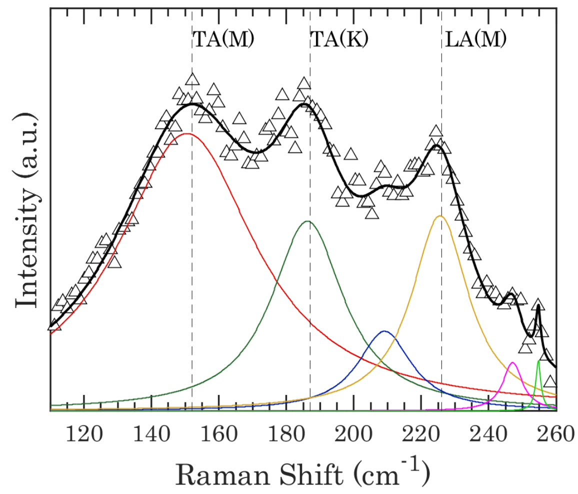

Figure D.1: Raman spectra of MoS_2 irradiated with 2.5×10^{15} He^{+} cm^{-2}. The range shown includes the *LA*(*M*) mode at ~ 226 cm^{-1} which is highlighted with the dashed vertical line. This region was fitted with Lorentzians as shown in a range of colours, the sum of which is shown in the thicker black line.

Appendix E

Probe Size Measurement in the GIM

In order to measure the probe size of an ion beam microscope, an image was acquired near but not of the sample region due to the large dose required to take a high quality image. Typically, the amorphous carbon on a TEM grid was used for this purpose. It was assumed that the feature being imaged had a perfectly sharp edge to allow for the measurement. The intensity from the area surrounding the feature was minimised by placing a carbon coated surface several millimetres below the sample. This coating has both a low secondary electron yield and a low backscattered ion yield. The intensity drop off over the edge of the flake in the image can thus be attributed entirely to the Gaussian distribution of the ions in the probe. The probe size could thus be measured from the acquired image using imagej software. The distance between 25% and 75% of the average intensity of the flake was taken as the probe size. This is equivalent to the full width at half maximum of the probe.

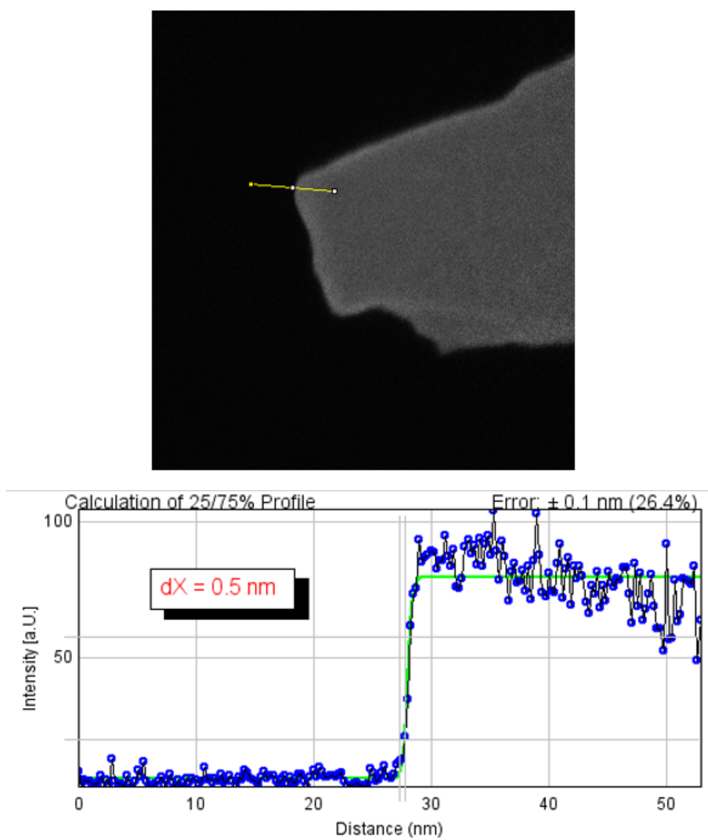

Figure E.1: Measuring probe size from a GIM image. Measuring probe size from a He^{+} image in *ImageJ*. [190]

Appendix F

Oxidative Etching Attempts with Mechanically Exfoliated MoS_2

Mechanical exfoliation was performed as in chapter 6 and the sample was positioned on a substrate of 300 nm of SiO_2 on Si. A relatively thick (5-10 L from OM) flake was selected for irradiation and heating as seen in figure F.1(a). Unexpectedly, the sample was not observed to etch as was the case for MoS_2 prepared by CVD. The reason seems to be an issue of surface cleanliness. Figure F.1(b) shows the irradiated regions at which there is a build up of ion beam-induced contamination material. Organic residue from the exfoliation process on the surface likely provided a ready source of carbon material which cross-linked and was deposited in locations where the ion beam dwelt. Since the penetration depth of the He^+ beam is of the order of hundreds of nanometres, the irradiated regions were still damaged. However, during the heating process it is likely that oxygen did not diffuse to the MoS_2 surface and thus could not be adsorbed. In the absence of readily available oxygen, the oxidation step could not occur.

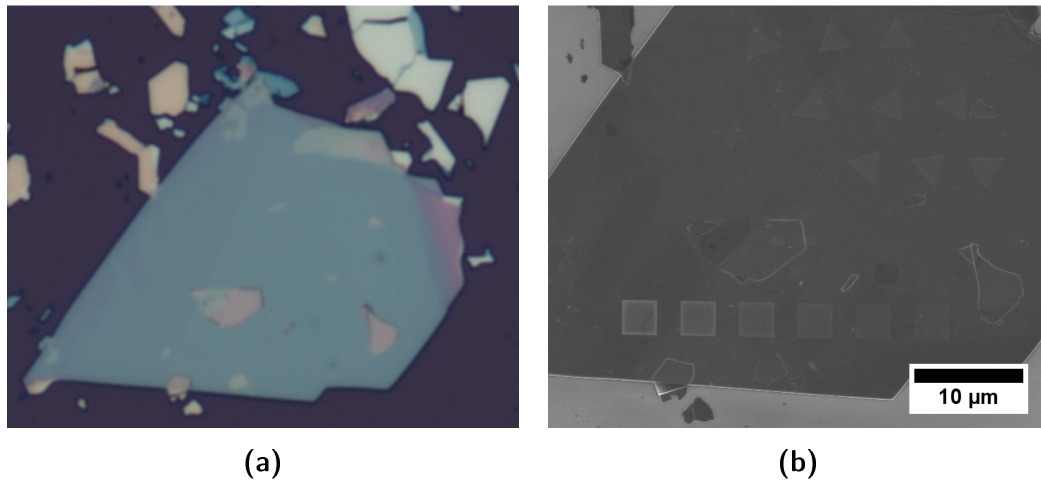

Figure F.1: Attempted etching of mechanically exfoliated MoS_2. (a) shows an optical image of the selected mechanically exfoliated flake. (b) shows an SEM image of the same flake at higher magnification and after heating to 330°C for 50 mins. Towards the top, the shape of irradiated (2×10^{14} He^{+} cm^{-2}) triangles at different angles can be seen. At the bottom, an array of 7 squares can be seen which were irradiated with progressively increasing doses from right to left.

Appendix G

Producing Meshes with Oxidation

Since etching is initiated at defect sites, whether native or ion-induced, with control of the heating parameters it is possible to create meshes of etched material as in this work and others [95]. A non-irradiated mesh, produced by heating to 320°C for 50 mins is shown in figure G.1(a). An edge detection algorithm was applied in *matlab* in order to highlight the shapes of the etched features. It is shown in figure G.1(b) and overlaid on the original image in figure G.1(c).

Figure G.1(d) shows an irradiated array of lines etched preferentially with dose decreasing from left to right. Of note is the increased width and integrity of the material between these lines as the dose decreases. In fact the edges of the remaining features charge and appear bright in the SEM images where electrically connected to the bulk of the MoS_2 flake while those which are not connected exhibit a much lower contrast as the edge. This is made somewhat clearer in figure G.1(e) which includes the edge detected overlay as in figure G.1(c).

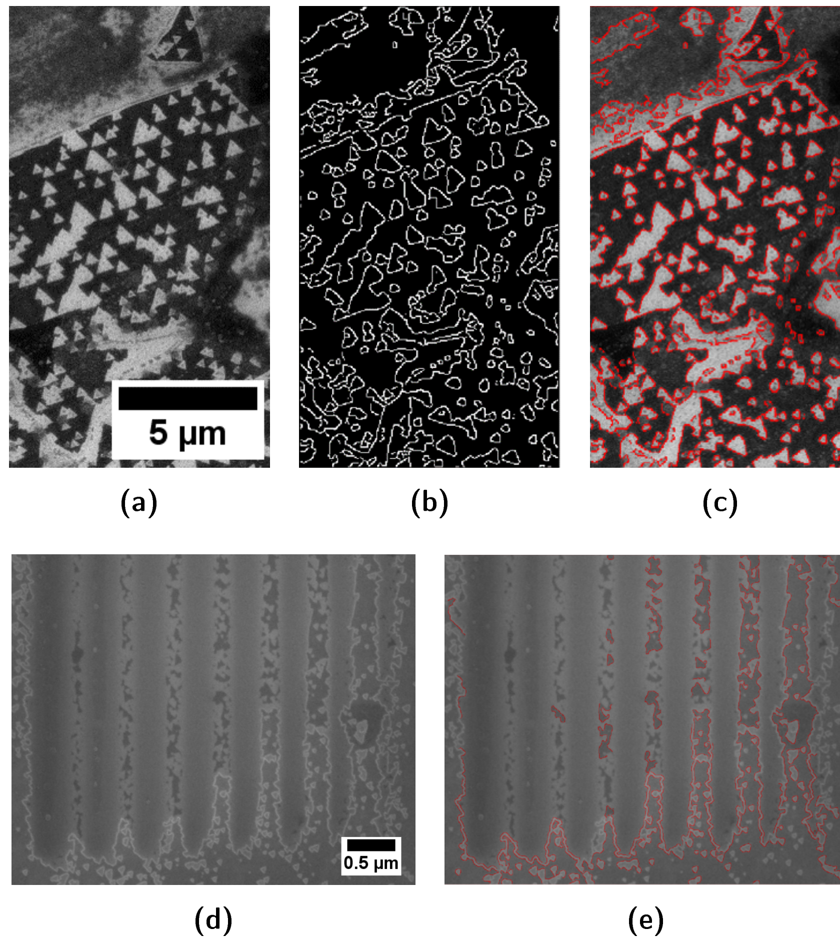

Figure G.1: Meshes of CVD-grown MoS_2 produced by oxidation. (a) SEM image (inLens, 10 keV) of MoS_2 etched at native defect sites. (b) The same image after passing through edge detection in *matlab*. (c) Overlay of the edge detection image (now in red) on the original image. (d) Another SEM image (inLens, 10 keV) of MoS_2 etched at ion-induced defect sites in an array of lines of progressively higher doses. (e) Same image repeated with edge detection.

Bibliography

[1] K. S. Novoselov, A. K. Geim, S. V. Morozov, D. Jiang, Y. Zhang, S. V. Dubonos, I. V. Grigorieva, and A. A. Firsov. Electric Field Effect in Atomically Thin Carbon Films. *Science*, 306(5696):666–669, oct 2004. ISSN 0036-8075. doi: 10.1126/science.1102896.

[2] P. R. Wallace. The Band Theory of Graphite. *Physical Review*, 71(9):622–634, 1947. ISSN 0031899X. doi: 10.1103/PhysRev.71.622.

[3] H. P. Boehm, R. Setton, and E. Stumpp. Nomenclature and Terminology of Graphite. *Pure and Applied Chemistry*, 66(9):1893–1901, 1994.

[4] Y. Hancock. The 2010 Nobel Prize in Physics - Ground-breaking Experiments on Graphene. *Journal of Physics D: Applied Physics*, 44(47), 2011. ISSN 00223727. doi: 10.1088/0022-3727/44/47/473001.

[5] R. Mas-Ballesté, C. Gómez-Navarro, J. Gómez-Herrero, and F. Zamora. 2D materials: to Graphene and Beyond. *Nanoscale*, 3(1):20–30, 2011. ISSN 2040-3372. doi: 10.1039/c0nr00323a.

[6] K. S. Novoselov, V. I. Fal'ko, L. Colombo, P. R. Gellert, M. G. Schwab, and K. Kim. A Roadmap for Graphene. *Nature*, 490(7419):192–200, oct 2012. ISSN 1476-4687. doi: 10.1038/nature11458.

[7] S. Z. Butler, S. M. Hollen, L. Cao, Y. Cui, J. A. Gupta, H. R. Gutiérrez, T. F. Heinz, S. S. Hong, J. Huang, A. F. Ismach, E. Johnston-Halperin, M. Kuno, V. V. Plashnitsa, R. D. Robinson, R. S. Ruoff, S. Salahuddin, J. Shan, L. Shi, M. G Spencer, M. Terrones, W. Windl, and J. E. Goldberger. Opportunities

in Two-Dimensional Materials Beyond Graphene. *ACS Nano*, 7(4):2898–2926, 2013.

[8] C. Backes, R. J. Smith, N. McEvoy, N. C. Berner, D. McCloskey, H. C. Nerl, A. O'Neill, P. J. King, T. Higgins, D. Hanlon, N. Scheuschner, J. Maultzsch, L. Houben, G. S. Duesberg, J. F. Donegan, V. Nicolosi, and J. N. Coleman. Edge and Confinement Effects Allow in situ Measurement of Size and Thickness of Liquid-Exfoliated Nanosheets. *Nature Communications*, 5:4576, 2014. ISSN 2041-1723. doi: 10.1038/ncomms5576.

[9] A. Splendiani, L. Sun, Y. Zhang, Ti. Li, J. Kim, C. Y. Chim, G. Galli, and F. Wang. Emerging Photoluminescence in Monolayer MoS_2. *Nano Letters*, 10 (4):1271–5, 2010. ISSN 1530-6992. doi: 10.1021/nl903868w.

[10] K. F. Mak, C. Lee, J. Hone, J. Shan, and T. F. Heinz. Atomically Thin MoS_2: A New Direct-Gap Semiconductor. *Physical Review Letters*, 105(136805), 2010. ISSN 0031-9007. doi: 10.1103/PhysRevLett.105.136805.

[11] C. Lee, H. Yan, L. E. Brus, T. F. Heinz, J. Hone, and S. Ryu. Anomalous Lattice Vibrations of Single and Few-Layer MoS_2. *ACS Nano*, 4(5):2695–2700, 2010.

[12] Y. Liu, H. Nan, X. Wu, W. Pan, W. Wang, J. Bai, W. Zhao, and L. Sun. Layer-by-Layer Thinning of MoS_2 by Plasma. *ACS Nano*, 7(5):4202–4209, 2013. ISSN 1936-0851. doi: 10.1021/nn400644t.

[13] M. Ye, D. Winslow, D. Zhang, R. Pandey, and Y. K. Yap. Recent Advancement on the Optical Properties of Two-Dimensional Molybdenum Disulfide (MoS_2) Thin Films. *Photonics*, 2:288–307, 2015. ISSN 2304-6732. doi: 10.3390/photonics2010288.

[14] Z. He and W. Que. Molybdenum Disulfide Nanomaterials: Structures, Properties, Synthesis and Recent Progress on Hydrogen Evolution Reaction. *Applied Materials Today*, 3:23–56, 2016. ISSN 23529407. doi: 10.1016/j.apmt.2016.02.001.

[15] M. Lundstrom. Moore's Law Forever? *Science*, 299(5604):210–211, 2003. ISSN 0036-8075. doi: 10.1126/science.1079567.

[16] E. W. Lee, L. Ma, D. N. Nath, C. H. Lee, A. Arehart, Y. Wu, and S. Rajan. Growth and Electrical Characterization of Two-Dimensional Layered MoS_2/SiC Heterojunctions. *Applied Physics Letters*, 105(20):203504, 2014.

[17] C. Ataca, H. Şahin, E. Aktürk, and S. Ciraci. Mechanical and Electronic Properties of MoS_2 Nanoribbons and their Defects. *The Journal of Physical Chemistry C*, 115(10):3934–3941, 2011. ISSN 1932-7447. doi: 10.1021/jp1115146.

[18] M. Ghorbani-Asl, A. N. Enyashin, A. Kuc, G. Seifert, and T. Heine. Defect-Induced Conductivity Anisotropy in MoS_2 Monolayers. *Physical Review B - Condensed Matter and Materials Physics*, 88(245440):1–7, 2013. ISSN 10980121. doi: 10.1103/PhysRevB.88.245440.

[19] Y. Zhou, Z. Liao, Y. Wang, G. S. Duesberg, J. Xu, Q. Fu, X. Wu, and D. Yu. Ion Irradiation Induced Structural and Electrical Transition in Graphene. *The Journal of Chemical Physics*, 133:234703, 2010. ISSN 1089-7690. doi: 10.1063/1.3518979.

[20] W. Zhou, X. Zou, S. Najmaei, Z. Liu, Y. Shi, J. Kong, J. Lou, P. M. Ajayan, B. I. Yakobson, and J. C. Idrobo. Intrinsic Structural Defects in Monolayer Molybdenum Disulfide. *Nano Letters*, 13:2615–2622, 2013. ISSN 15306984. doi: 10.1021/nl4007479.

[21] H. Q. Zhao, X. Mao, D. Zhou, S. Feng, X. Shi, Y. Ma, X. Wei, and Y. Mao. Bandgap Modulation of MoS_2 Monolayer by Thermal Annealing and Quick Cooling. *Nanoscale*, 7:7126–7131, 2016. ISSN 2040-3364. doi: 10.1039/C6NR05638E.

[22] A. R. Botello-Méndez, F. López-Urías, M. Terrones, and H. Terrones. Metallic and Ferromagnetic Edges in Molybdenum Disulfide Nanoribbons. *Nanotechnology*, 20(32):325703, 2009.

[23] M. Nastasi, J. W. Mayer, and J. K. Hirvonen. Cross-Section. In *Ion-Solid Interactions: Fundamentals and Applications*, pages 62–87. Cambridge University Press, 1st edition, 1996.

[24] S. Pezzagna, J. Meijer, and M. Goorsky (editor). High-Resolution Ion Implantation from keV to MeV, Ion Implantation. In *Ion Implantation*, pages 3–24. InTech, 2012. doi: 10.5772/34601.

[25] A. Nipane, D. Karmakar, N. Kaushik, S. Karande, and S. Lodha. Few-Layer MoS_2 p-Type Devices Enabled by Selective Doping Using Low Energy Phosphorus Implantation. *ACS Nano*, 10(2):2128–2137, 2016. ISSN 1936086X. doi: 10.1021/acsnano.5b06529.

[26] M. M. Lucchese, F. Stavale, E. H. Martins Ferreira, C. Vilani, M. V. O. Moutinho, R. B. Capaz, C. A. Achete, and A. Jorio. Quantifying Ion-Induced Defects and Raman Relaxation Length in Graphene. *Carbon*, 48(5):1592–1597, 2010. ISSN 00086223. doi: 10.1016/j.carbon.2009.12.057.

[27] L. G. Cançado, A. Jorio, E. H. Martins Ferreira, F. Stavale, C. A. Achete, R. B. Capaz, M. V. O. Moutinho, A. Lombardo, T. S. Kulmala, and A. C. Ferrari. Quantifying Defects in Graphene via Raman Spectroscopy at Different Excitation Energies. *Nano Letters*, 11(8):3190–3196, 2011. ISSN 15306984. doi: 10.1021/nl201432g.

[28] S. Mignuzzi, A. J. Pollard, N. Bonini, B. Brennan, I. S. Gilmore, M. A. Pimenta, D. Richards, and D. Roy. Effect of Disorder on Raman Scattering of Single-Layer MoS_2. *Physical Review B*, 91(195411):195411, 2015. ISSN 1550235X. doi: 10.1103/PhysRevB.91.195411.

[29] A. J. Pollard, B. Brennan, H. Stec, B. J. Tyler, M. P. Seah, I. S. Gilmore, and D. Roy. Quantitative Characterization of Defect Size in Graphene Using Raman Spectroscopy. *Applied Physics Letters*, 105(253107):253107, 2014. ISSN 00036951. doi: 10.1063/1.4905128.

[30] Q. Li, E. C. Walter, W. E. van der Veer, B. J. Murray, J. T. Newberg, E. W. Bohannan, J. A. Switzer, J. C. Hemminger, and R. M. Penner. Molybdenum

Disulfide Nanowires and Nanoribbons by Electrochemical/Chemical Synthesis. *The Journal of Physical Chemistry*, 109(8):3169–3182, 2005.

[31] S. K. Ghosh, C. Srivastava, S. Nath, and J. P. Celis. Simple Formation of Nanostructured Molybdenum Disulfide Thin Films by Electrodeposition. *International Journal of Electrochemistry*, page 7, 2013.

[32] J. Lin, O. Cretu, W. Zhou, K. Suenaga, D. Prasai, K. Bolotin, N. T. Cuong, M. Otani, S. Okada, A. R. Lupini, J. Idrobo, D. Caudel, A. Burger, N. Ghimire, J. Yan, D. Mandrus, S. Pennycook, and S. T. Pantelides. Flexible Metallic Nanowires with Self-Adaptive Contacts to Semiconducting Transition-Metal Dichalcogenide Monolayers. *Nature nanotechnology*, 9(6):436–442, 2014.

[33] X. Liu, T. Xu, X. Wu, Z. Zhang, J. Yu, H. Qiu, J. H. Hong, C. H. Jin, J. X. Li, X. R. Wang, L. T. Sun, and W. Guo. Top-Down Fabrication of Sub-Nanometre Semiconducting Nanoribbons Derived from Molybdenum Disulfide Sheets. *Nature Communications*, 4:1776, 2013. ISSN 2041-1723. doi: 10.1038/ncomms2803.

[34] J. Orloff, M. Utlaut, and L. Swanson. *High Resolution Focused Ion Beams: FIB and its Applications*. Kluwer/Plenum, New York, NY, 1st edition, 2003.

[35] D. C. Bell, M. C. Lemme, L. A. Stern, J. R. Williams, and C. M. Marcus. Precision Cutting and Patterning of Graphene with Helium Ions. *Nanotechnology*, 20:455301, 2009. ISSN 0957-4484. doi: 10.1088/0957-4484/20/45/455301.

[36] N. Kalhor, S. A. Boden, and H. Mizuta. Sub-10nm Patterning by Focused He-Ion Beam Milling for Fabrication of Downscaled Graphene Nano Devices. *Microelectronic Engineering*, 114:70–77, 2014. ISSN 01679317. doi: 10.1016/j.mee.2013.09.018.

[37] D. S. Fox, Y. Zhou, P. Maguire, A. O'Neill, C. O'Coileáin, R. Gatensby, A. M. Glushenkov, T. Tao, G. S. Duesberg, I. V. Shvets, M. Abid, M. Abid, H. C. Wu, Y. Chen, J. N. Coleman, J. F. Donegan, and H. Zhang. Nanopatterning and Electrical Tuning of MoS_2 Layers with a Subnanometer Helium

Ion Beam. *Nano Letters*, 15(8):5307–5313, 2015. ISSN 15306992. doi: 10.1021/acs.nanolett.5b01673.

[38] Y. Naitou, T. Iijima, and S. Ogawa. Direct Nano-Patterning of Graphene with Helium Ion Beams. *Applied Physics Letters*, 106(033103):033103, 2015. ISSN 00036951. doi: 10.1063/1.4906415.

[39] B. S. Archanjo, B. Fragneaud, L. G. Cançado, D. Winston, F. Miao, C. A. Achete, and G. Medeiros-Ribeiro. Graphene Nanoribbon Superlattices Fabricated via He Ion Lithography. *Applied Physics Letters*, 104(193114):193114, 2014. ISSN 0003-6951. doi: 10.1063/1.4878407.

[40] R. R. Nair, M. Sepioni, I. L. Tsai, O. Lehtinen, J. Keinonen, A. V. Krasheninnikov, T. Thomson, A. K. Geim, and I. V. Grigorieva. Spin-Half Paramagnetism in Graphene Induced by Point Defects. *Nature Physics*, 8:199–202, 2012. ISSN 1745-2473. doi: 10.1038/nphys2183.

[41] G. Nanda, S. Goswami, K. Watanabe, T. Taniguchi, and P. F. A. Alkemade. Defect Control and n-Doping of Encapsulated Graphene by Helium-Ion-Beam Irradiation. *Nano Letters*, 15:4006–4012, 2015. ISSN 1530-6984. doi: 10.1021/acs.nanolett.5b00939.

[42] D. S. Fox, P. Maguire, Y. Zhou, C. Rodenburg, A. O'Neill, J. N. Coleman, and H. Zhang. Sub-5nm Graphene Nanopore Fabrication by Nitrogen ion Etching Induced by a Low-Energy Electron Beam. *Nanotechnology*, 27(195302), 2016.

[43] P. Maguire, D. S. Fox, Y. Zhou, Q. Wang, M. O'Brien, J. Jadwiszczak, J. McManus, N. McEvoy, G. S. Duesberg, and H. Zhang. Defect Sizing, Distance and Substrate Effects in Ion-Irradiated Monolayer 2D Materials. *ArXiv*, pages 1–11, 2017.

[44] C. T. Pan, J. A. Hinks, Q. M. Ramasse, G. Greaves, U. Bangert, S. E. Donnelly, and S. J. Haigh. In-Situ Observation and Atomic Resolution Imaging of the Ion Irradiation Induced Amorphisation of Graphene. *Scientific Reports*, 4(i): 6334, 2014. ISSN 2045-2322. doi: 10.1038/srep06334.

[45] E. J. Heller, Y. Yang, L. Kocia, W. Chen, S. Fang, M. Borunda, and E. Kaxiras. Theory of Graphene Raman Scattering. *ACS Nano*, 10(2):2803–2818, 2016. ISSN 1936086X. doi: 10.1021/acsnano.5b07676.

[46] C. Lee, X. Wei, J. W. Kysar, and J. Hone. Measurement of the Elastic Properties and Intrinsic Strength of Monolayer Graphene. *Science*, 321:385–388, 2008. ISSN 0036-8075, 1095-9203. doi: 10.1126/science.1157996.

[47] S. V. Morozov, K. S. Novoselov, M. I. Katsnelson, F. Schedin, D. C. Elias, J. A. Jaszczak, and A. K. Geim. Giant Intrinsic Carrier Mobilities in Graphene and its Bilayer. *Physical Review Letters*, 100(016602):11–14, 2008. ISSN 00319007. doi: 10.1103/PhysRevLett.100.016602.

[48] J. Moser, A. Barreiro, and A. Bachtold. Current-Induced Cleaning of Graphene. *Applied Physics Letters*, 91(16):1–4, 2007. ISSN 00036951. doi: 10.1063/1.2789673.

[49] A. A. Balandin. Thermal Properties of Graphene and Nanostructured Carbon Materials. *Nature Materials*, 10(8):569–581, 2011. ISSN 14764660. doi: 10.1038/nmat3064.

[50] M. D. Stoller, S. Park, Y. Zhu, J. An, and R. S. Ruoff. Graphene-Based Ultracapacitors. *Nano letters*, 8(10):3498–3502, 2008.

[51] I. K. Moon, J. I. Kim, H. Lee, K. Hur, W. C. Kim, and H. Lee. 2D Graphene Oxide Nanosheets as an Adhesive Over-Coating Layer for Flexible Transparent Conductive Electrodes. *Scientific Reports*, 3(1):1112, 2013. ISSN 2045-2322. doi: 10.1038/srep01112.

[52] D. Lee, H. Lee, Y. Ahn, and Y. Lee. High-Performance Flexible Transparent Conductive Film Based on Graphene/AgNW/Graphene Sandwich Structure. *Carbon*, 81(1):439–446, 2015. ISSN 00086223. doi: 10.1016/j.carbon.2014.09.076.

[53] S. P. Surwade, S. N. Smirnov, I. V. Vlassiouk, R. R. Unocic, G. M. Veith, S. Dai, and S. M. Mahurin. Water Sesalination Using Nanoporous Single-Layer

Graphene. *Nature Nanotechnology*, 10(5):459–464, 2015. ISSN 1748-3387. doi: 10.1038/nnano.2015.37.

[54] S. J. Heerema and C. Dekker. Graphene Nanodevices for DNA Sequencing. *Nature Nanotechnology*, 11(2):127–136, 2016. ISSN 1748-3387. doi: 10.1038/nnano.2015.307.

[55] M. Lotya, Y. Hernandez, P. J. King, R. J Smith, V. Nicolosi, L. S. Karlsson, M. Blighe, S. De, Z. Wang, I. T. Mcgovern, G. S. Duesberg, J. N. Coleman, and F. M. Blighe. Liquid Phase Production of Graphene by Exfoliation of Graphite in Surfactant / Water Solutions Liquid Phase Production of Graphene by Exfoliation of Graphite in Surfactant / Water Solutions. *Journal of the American Chemical Society*, (11):3611–3620, 2009. doi: 10.1021/ja807449u.

[56] A. O'Neill, U. Khan, P. N. Nirmalraj, J. Boland, and J. N. Coleman. Graphene Dispersion and Exfoliation in Low Boiling Point Solvents. *Journal of Physical Chemistry C*, 115(13):5422–5428, 2011. ISSN 19327447. doi: 10.1021/jp110942e.

[57] A. N. Obraztsov. Making Graphene on a Large Scale. *Nature Nanotechnology*, 4:212–213, 2009. ISSN 1748-3395. doi: 10.1038/nnano.2009.67.

[58] S. Kumar, N. McEvoy, H. Y. Kim, K. Lee, N. Peltekis, E. Rezvani, H. Nolan, A. Weidlich, R. Daly, and G. S. Duesberg. CVD Growth and Processing of Graphene for Electronic Applications. *Physica Status Solidi (B)*, 248(11):2604–2608, 2011. ISSN 03701972. doi: 10.1002/pssb.201100179.

[59] T. Kobayashi, M. Bando, N. Kimura, K. Shimizu, K. Kadono, N. Umezu, K. Miyahara, S. Hayazaki, S. Nagai, Y. Mizuguchi, Y. Murakami, and D. Hobara. Production of a 100 m-Long High-Quality Graphene Transparent Conductive Film by Roll-to-Roll Chemical Vapor Deposition and Transfer Process. *Applied Physics Letters*, 102(2):1–5, 2013. ISSN 00036951. doi: 10.1063/1.4776707.

[60] F. Banhart, J. Kotakoski, and A. V. Krasheninnikov. Structural Defects in Graphene. *Acs Nano*, 5(1):26–41, 2011. ISSN 1936-0851. doi: 10.1021/nn102598m.

[61] C. Virojanadara, M. Syväjarvi, R. Yakimova, L. I. Johansson, A. A. Zakharov, and T. Balasubramanian. Homogeneous Large-Area Graphene Layer Growth on 6 H-SiC (0001). *Physical Review B*, 78(24):245403, 2008.

[62] M. Lazzeri, C. Attaccalite, L. Wirtz, and F. Mauri. Impact of the Electron-Electron Correlation on Phonon Dispersion: Failure of LDA and GGA DFT Functionals in Graphene and Graphite. *Physical Review B - Condensed Matter and Materials Physics*, 78(8):8–11, 2008. ISSN 10980121. doi: 10.1103/PhysRevB.78.081406.

[63] L. M. Malard, M. A. Pimenta, G. Dresselhaus, and M. S. Dresselhaus. Raman Spectroscopy in Graphene. *Physics Reports*, 473(5-6):51–87, 2009. ISSN 03701573. doi: 10.1016/j.physrep.2009.02.003.

[64] A. C. Ferrari, J. C. Meyer, V. Scardaci, C. Casiraghi, M. Lazzeri, F. Mauri, S. Piscanec, D. Jiang, K. S. Novoselov, S. Roth, and A. K. Geim. Raman Spectrum of Graphene and Graphene Layers. *Physical Review Letters*, 97(187401), 2006. ISSN 00319007. doi: 10.1103/PhysRevLett.97.187401.

[65] A. C. Ferrari. Raman Spectroscopy of Graphene and Graphite: Disorder, Electron-Phonon Coupling, Doping and Nonadiabatic Effects. *Solid State Communications*, 143(1-2):47–57, 2007. ISSN 00381098. doi: 10.1016/j.ssc.2007.03.052.

[66] A. C. Ferrari and D. M. Basko. Raman Spectroscopy as a Versatile Tool for Studying the Properties of Graphene. *Nature Nanotechnology*, 8(4):235–246, 2013. ISSN 1748-3395 (Electronic) 1748-3387 (Linking). doi: 10.1038/nnano.2013.46.

[67] F. Tuinstra, J. L. Koenig, and L.J. Koenig. Raman Spectrum of Graphite. *The Journal of Chemical Physics*, 53(3):1126–1130, 1970. ISSN 00219606. doi: 10.1063/1.1674108.

[68] M. S. Dresselhaus, G. Dresselhaus, R. Saito, and A. Jorio. Raman Spectroscopy of Carbon Nanotubes. *Physics reports*, 409(2):47–99, 2005.

[69] K. A. Wang, A. M. Rao, P. C. Eklund, M. S. Dresselhaus, and G. Dresselhaus. Observation of higher-order infrared modes in solid C60 films. *Physical Review B*, 48(15):11375–11380, 1993. ISSN 01631829. doi: 10.1103/PhysRevB.48.11375.

[70] R. Saito, G. Dresselhaus, and M.S. Dresselhaus. *Transport Properties of Carbon Nanotubes*, pages 137–162. 1998. doi: 10.1142/9781860943799_0008.

[71] R. Beams, L. G. Cançado, and L. Novotny. Low Temperature Raman Study of the Electron Coherence Length Near Graphene Edges. *Nano Letters*, 11:1177–1181, 2011. ISSN 15306984. doi: 10.1021/nl104134a.

[72] A. Eckmann, A. Felten, I. Verzhbitskiy, R. Davey, and C. Casiraghi. Raman Study on Defective Graphene: Effect of the Excitation Energy, Type, and Amount of Defects. *Physical Review B - Condensed Matter and Materials Physics*, 88(035426):1–11, 2013. ISSN 10980121. doi: 10.1103/PhysRevB.88.035426.

[73] L. G. Cançado, A. Jorio, and M. A. Pimenta. Measuring the absolute Raman cross section of nanographites as a function of laser energy and crystallite size. *Physical Review B - Condensed Matter and Materials Physics*, 76(6):1–7, 2007. ISSN 10980121. doi: 10.1103/PhysRevB.76.064304.

[74] S. Hang, Z. Moktadir, and H. Mizuta. Raman Study of Damage Extent in Graphene Nanostructures Carved by High Energy Helium Ion Beam. *Carbon*, 72:233–241, 2014. ISSN 00086223. doi: 10.1016/j.carbon.2014.01.071.

[75] D. Graf, F. Molitor, K. Ensslin, C. Stampfer, A. Jungen, C. Hierold, and L. Wirtz. Spatially Resolved Raman Spectroscopy of Single- and Few-Layer Graphene. *Nano Letters*, 7(2):238–242, 2007. ISSN 15306984. doi: 10.1021/nl061702a.

[76] R. Quhe, J. Zheng, G. Luo, Q. Liu, R. Qin, J. Zhou, D. Yu, S. Nagase, W. N. Mei, Z. Gao, and J. Lu. Tunable and Sizable Band Gap of Single-Layer Graphene Sandwiched between Hexagonal Boron Nitride. *NPG Asia Materials*, 4(4):e16, 2012. ISSN 1884-4057. doi: 10.1038/am.2012.29.

[77] J. Wang, R. Zhao, M. Yang, Z. Liu, and Z. Liu. Inverse Relationship between Carrier Mobility and Bandgap in Graphene. *Journal of Chemical Physics*, 138 (8), 2013. ISSN 00219606. doi: 10.1063/1.4792142.

[78] K. K. Kam and B. A. Parkinson. Detailed Photocurrent Spectroscopy. *J Phys Chem*, 86:463–467, 1982. ISSN 0022-3654. doi: 10.1021/j100393a010.

[79] O. Lopez-Sanchez, D. Lembke, M. Kayci, A. Radenovic, and A. Kis. Ultrasensitive Photodetectors Based on Monolayer MoS_2. *Nature Nanotechnology*, 8(7):497–501, 2013. ISSN 1748-3387. doi: 10.1038/nnano.2013.100.

[80] J. Zhang, S. Najmaei, H. Lin, and J. Lou. MoS_2 Atomic Layers with Artificial Active Edge Sites as Transparent Counter Electrodes for Improved Performance of Dye-Sensitized Solar Cells. *Nanoscale*, 6(10):5279–5283, 2014. ISSN 2040-3364. doi: 10.1039/C3NR05979K.

[81] J. Pu, Y. Yomogida, K. K. Liu, L. J. Li, Y. Iwasa, and T. Takenobu. Highly Flexible MoS_2 Thin-Film Transistors with Ion Gel Dielectrics. *Nano Letters*, 12(8):4013–4017, 2012.

[82] M. Buscema, G. A. Steele, H. S. J. van der Zant, and A. Castellanos-Gomez. The Effect of the Substrate on the Raman and Photoluminescence Emission of Single-Layer MoS_2. *Nano Research*, 7(4):1–11, 2014. ISSN 19980000. doi: 10.1007/s12274-014-0424-0.

[83] M. O'Brien, N. Scheuschner, J. Maultzsch, G. S. Duesberg, and N. McEvoy. Raman Spectroscopy of Suspended MoS_2. *Physica Status Solidi (B)*, 1700218, 2017. ISSN 03701972. doi: 10.1002/pssb.201700218.

[84] K. F. Mak, K. He, J. Shan, and T. F. Heinz. Control of Valley Polarization

in Monolayer MoS_2 by Optical Helicity. *Nature Nanotechnology*, 7(8):494–498, 2012. ISSN 1748-3387. doi: 10.1038/nnano.2012.96.

[85] F. Wu, F. Qu, and A. H. MacDonald. Exciton Band Structure of Monolayer MoS_2. *Physical Review B - Condensed Matter and Materials Physics*, 91 (075310):075310, 2015. ISSN 1550235X. doi: 10.1103/PhysRevB.91.075310.

[86] A. Castellanos-Gomez, H. S. J. van der Zant, and G. A. Steele. Folded MoS_2 Layers with Reduced Interlayer Coupling. *Nano Research*, 7(4):572–578, 2014. ISSN 19980000. doi: 10.1007/s12274-014-0425-z.

[87] N. Zibouche, A. Kuc, J. Musfeldt, and T. Heine. Transition-Metal Dichalcogenides for Spintronic Applications. *Annalen der Physik*, 526(9-10):395–401, 2014.

[88] S. X. Wang, H. H. Yu, and H. J. Zhang. Band-Gap Modulation of Two-Dimensional Saturable Absorbers for Solid-State Lasers. *Photonics Research*, 3(2):A10–A20, 2015. ISSN 23279125. doi: 10.1364/prj.3.000a10.

[89] I. Song, C. Park, and H. C. Choi. Synthesis and Properties of Molybdenum Disulphide: from Bulk to Atomic Layers. *RSC Adv.*, 5(10):7495–7514, 2015. ISSN 2046-2069. doi: 10.1039/C4RA11852A.

[90] W. Zhu, T. Low, Y. H. Lee, H. Wang, D. B. Farmer, J. Kong, F. Xia, and P. Avouris. Electronic Transport and Device Prospects of Monolayer Molybdenum Disulphide Grown by Chemical Vapour Deposition. *Nature Communications*, 5:3087, 2014. ISSN 2041-1723. doi: 10.1038/ncomms4087.

[91] H. Qiu, T. Xu, Z. Wang, W. Ren, H. Nan, Z. Ni, Q. Chen, S. Yuan, F. Miao, F. Song, G. Long, Y. Shi, L. Sun, J. Wang, and X. Wang. Hopping Transport through Defect-Induced Localized States in Molybdenum Disulphide. *Nature Communications*, 4:2642, 2013. ISSN 2041-1723. doi: 10.1038/ncomms3642.

[92] R. Fivaz and E. Mooser. Mobility of Charge Carriers in Semiconducting Layer Structures. *Physical Review*, 163(3):743–755, 1967. ISSN 0031899X. doi: 10.1103/PhysRev.163.743.

[93] S. Chuang, C. Battaglia, A. Azcatl, S. McDonnell, J. S. Kang, X. Yin, M. Tosun, R. Kapadia, H. Fang, R. M. Wallace, and A. Javey. MoS_2 P-type Transistors and Diodes Enabled by High Work Function MoO_x Contacts. *Nano Letters*, 14(3):1337–1342, 2014. ISSN 15306992. doi: 10.1021/nl4043505.

[94] S. McDonnell, A. Azcatl, R. Addou, C. Gong, S. Chuang, K. Cho, A. Javey, and R. M. Wallace. Hole Contacts on Transition Metal Dichalcogenides : Interface Chemistry and Band Alignments Hole Contacts on Transition Metal Dichalcogenides: Interface Chemistry and Band Alignments. *ACS Nano*, 8(6): 6265–6272, 2014. ISSN 1936-0851.

[95] J. Wu, H. H. Li, Z. Yin, H. H. Li, J. Liu, X. Cao, Q. Zhang, and H. Zhang. Layer Thinning and Etching of Mechanically Exfoliated MoS_2 Nanosheets by Thermal Annealing in Air. *Small*, 9(19):3314–3319, 2013. ISSN 16136810. doi: 10.1002/smll.201301542.

[96] A. Azcatl, S. McDonnell, K. C. Santosh, X. Peng, H. Dong, X. Qin, R. Addou, G. I. Mordi, N. Lu, J. Kim, M. J. Kim, K. Cho, and R. M. Wallace. MoS_2 Functionalization for Ultra-Thin Atomic Layer Deposited Dielectrics. *Applied Physics Letters*, 104(111601), 2014. ISSN 00036951. doi: 10.1063/1.4869149.

[97] J. A. Spirko, M. L. Neiman, A. M. Oelker, and K. Klier. Electronic Structure and Reactivity of Defect MoS_2. *Surface Science*, 542(3):192–204, 2003. ISSN 00396028. doi: 10.1016/S0039-6028(03)00957-9.

[98] T. J. Wieting and J. L. Verble. Infrared and Raman Studies of Long-Wavelength Optical Phonons in Hexagonal MoS_2. *Physical Review B*, 3(12): 4286–4292, 1971. ISSN 01631829. doi: 10.1103/PhysRevB.3.4286.

[99] J. M. Chen and C. S. Wang. Second Order Raman Spectrum of MoS_2. *Solid State Communications*, 14(9):857–860, 1974. ISSN 00381098. doi: 10.1016/0038-1098(74)90150-1.

[100] B. C. Windom, W. G. Sawyer, and D. W. Hahn. A Raman Spectroscopic Study of MoS_2 and MoO_3: Applications to Tribological Systems. *Tribology Letters*, 42(3):301–310, 2011. ISSN 10238883. doi: 10.1007/s11249-011-9774-x.

[101] T. Livneh and J. E. Spanier. A Comprehensive Multiphonon Spectral Analysis in MoS_2. *2D Materials*, 2:035003, 2015. ISSN 2053-1583. doi: 10.1088/2053-1583/2/3/035003.

[102] A. M. Stacy and D. T. Hodul. Raman Spectra of IVB and VIB Transition Metal Disulfides Using Laser Energies Near the Absorption Edges. *Journal of Physics and Chemistry of Solids*, 46(4):405–409, 1985. ISSN 00223697. doi: 10.1016/0022-3697(85)90103-9.

[103] G. L. Frey, R. Tenne, M. J. Matthews, M. S. Dresselhaus, and G. Dresselhaus. Raman and Resonance Raman Investigation of MoS_2 Nanoparticles. *Physical Review B*, 60(4):2883–2892, 1999. ISSN 0163-1829. doi: 10.1103/PhysRevB.60.2883.

[104] C. Rice, R. J. Young, R. Zan, U. Bangert, D. Wolverson, T. Georgiou, R. Jalil, and K. S. Novoselov. Raman-Scattering Measurements and First-Principles Calculations of Strain-Induced Phonon Shifts in Monolayer MoS_2. *Physical Review B*, 87(081307):081307, 2013. ISSN 10980121. doi: 10.1103/PhysRevB.87.081307.

[105] B. Chakraborty, A. Bera, D. V. S. Muthu, S. Bhowmick, U. V. Waghmare, and A. K. Sood. Symmetry-Dependent Phonon Renormalization in Monolayer MoS_2 Transistor. *Physical Review B*, 85(161403):161403, 2012. ISSN 10980121. doi: 10.1103/PhysRevB.85.161403.

[106] H. Li, Q. Zhang, C. C. R. Yap, B. K. Tay, T. H. T. Edwin, A. Olivier, and D. Baillargeat. From Bulk to Monolayer MoS_2: Evolution of Raman Scattering. *Advanced Functional Materials*, 22:1385–1390, 2012. ISSN 1616301X. doi: 10.1002/adfm.201102111.

[107] H. Li, Z. Yin, Q. He, H. Li, X. Huang, G. Lu, D. W. H. Fam, A. I. Y. Tok, Q. Zhang, and H. Zhang. Fabrication of Single- and Multilayer MoS_2 Film-Based Field-Effect Transistors for Sensing NO at Room Temperature. *Small*, 8(1):63–67, 2012. ISSN 16136810. doi: 10.1002/smll.201101016.

[108] Y. Zhao, X. Luo, H. Li, J. Zhang, P. T. Araujo, C. K. Gan, J. Wu, H. Zhang, S. Y. Quek, M. S. Dresselhaus, and Q. Xiong. Interlayer Breathing and Shear Modes in Few-Trilayer MoS_2 and WSe_2. *Nano Letters*, 13(3):1007–1015, 2013. ISSN 15306984. doi: 10.1021/nl304169w.

[109] A Molina-Sánchez and L Wirtz. Phonons in Single-Layer and Few-Layer MoS_2 and WS_2. *Phys. Rev. B*, 84(15):155413, 2011. doi: 10.1103/PhysRevB.84.155413. URL `https://link.aps.org/doi/10.1103/PhysRevB.84.155413`.

[110] X. Zhang, X. F. Qiao, W. Shi, J. B. Wu, D. S. Jiang, and P. H. Tan. Phonon and Raman Scattering of Two-Dimensional Transition Metal Dichalcogenides from Monolayer, Multilayer to Bulk Material. *Chem. Soc. Rev.*, 44(9):2757–2785, 2015. doi: 10.1039/C4CS00282B.

[111] X. Zhang, W. P. Han, J. B. Wu, S. Milana, Y. Lu, Q. Q. Li, A. C. Ferrari, and P. H. Tan. Raman Spectroscopy of Shear and Layer Breathing Modes in Multilayer MoS_2. *Physical Review B*, 87(115413), 2013. ISSN 10980121. doi: 10.1103/PhysRevB.87.115413.

[112] A. Castellanos-Gomez, M. Barkelid, A. M. Goossens, V. E. Calado, H. S. J. Van Der Zant, and G. A. Steele. Laser-Thinning of MoS_2: on Demand Generation of a Single-Layer semiconductor. *Nano Letters*, 12(6):3187–3192, 2012. ISSN 15306984. doi: 10.1021/nl301164v.

[113] D. Fox, Y. B. Zhou, A. O'Neill, S. Kumar, J.J. Wang, J. N. Coleman, G. S. Duesberg, J. F. Donegan, and H. Zhang. Helium Ion Microscopy of Graphene: Beam Damage, Image Quality and Edge Contrast. *Nanotechnology*, 24(335702), 2013. ISSN 1361-6528. doi: 10.1088/0957-4484/24/33/335702.

[114] Y. Shen and L. Sun. Setting up a Nanolab inside a Transmission Electron Microscope for Two-Dimensional Materials Research. *Journal of Materials Research*, 30(21):3153–3176, 2015. ISSN 0884-2914. doi: 10.1557/jmr.2015.304.

[115] H. P. Komsa, J. Kotakoski, S. Kurasch, O. Lehtinen, U. Kaiser, and A. V. Krasheninnikov. Two-Dimensional Transition Metal Dichalcogenides under

Electron Irradiation: Defect Production and Doping. *Physical Review Letters*, 109(035503):035503, 2012. ISSN 00319007. doi: 10.1103/PhysRevLett.109.035503.

[116] H. P. Komsa, S. Kurasch, O. Lehtinen, U. Kaiser, and A. V. Krasheninnikov. From Point to Extended Defects in Two-Dimensional MoS_2: Evolution of Atomic Structure under Electron Irradiation. *Physical Review B*, 88(035301): 035301, 2013. ISSN 10980121. doi: 10.1103/PhysRevB.88.035301.

[117] M. Ghorbani-Asl, N. Zibouche, M. Wahiduzzaman, A. F. Oliveira, A. Kuc, and T. Heine. Electromechanics in MoS_2 and WS_2: Nanotubes vs. Monolayers. *Scientific Reports*, 3:2961, 2013. ISSN 2045-2322. doi: 10.1038/srep02961.

[118] Y. Huang, J. Wu, X. Xu, Y. Ho, G. Ni, and Q. Zou. An Innovative Way of Etching MoS_2: Characterization and Mechanistic Investigation. *Nano Research*, 6 (3):200–207, 2013.

[119] I. S. Kim, V. K. Sangwan, D. Jariwala, J. D. Wood, S. Park, K. S. Chen, F. Shi, F. Ruiz-Zepeda, A. Ponce, M. Jose-Yacaman, V. P. Dravid, T. J. Marks, M. C. Hersam, and L. J. Lauhon. Influence of Stoichiometry on the Optical and Electrical Properties of Chemical Vapor Deposition Derived MoS_2. *ACS Nano*, 8(10):10551–10558, 2014. ISSN 1936-086X. doi: 10.1021/nn503988x.

[120] J. W. Jiang, X. Zhuang, and T. Rabczuk. Orientation Dependent Thermal Conductance in Single-Layer MoS_2. *Scientific Reports*, 3:2209, 2013. ISSN 2045-2322. doi: 10.1038/srep02209.

[121] Y. Li, Z. Zhou, S. Zhang, and Z. Chen. MoS_2 Nanoribbons: High Stability and Unusual Electronic and Magnetic Properties. *Journal of the American Chemical Society*, 130(49):16739–16744, 2008.

[122] T. Levente, D. Gergely, N. I. P, L. Phillipe, and B. P. László. Crystallographically Oriented High Resolution Lithography of Graphene Nanoribbons by STM Lithography. *physica status solidi (b)*, 247(4):896–902, 2010.

[123] T. Levente, D. Gergely, L. Phillipe, and B. P. László. Tailoring the Atomic Structure of Graphene Nanoribbons by Scanning Tunnelling Microscope Lithography. *Nature Nanotechnology*, 3:397 – 401, 2008.

[124] L. S. Weng, L. Y. Zhang, Y. P. Chen, and L. P. Rokhinson. Atomic Force Microscope Local Oxidation Nanolithography of Graphene. *Applied Physics Letters*, 93(9), 2008.

[125] J. Orloff, L. W. Swanson, and M. Utlaut. Fundamental Limits to Imaging Resolution for Focused Ion Beams. *J. Vac. Sci. Technol. B*, 14:3759, 1996.

[126] R. Hill, J. A. Notte, and L. Scipioni. Scanning Helium Ion Microscopy. In Peter W Hawkes, editor, *Advances in Imaging and Electron Physics Vol. 170*, volume 170, pages 65–148. Elsevier, 2012.

[127] G. Hlawacek, V. Veligura, R. van Gastel, and B. Poelsema. Helium Ion Microscopy. *Journal of Vacuum Science & Technology B: Microelectronics and Nanometer Structures*, 32(2):020801–1–020801–13, 2014. ISSN 2166-2746. doi: 10.1116/1.4863676.

[128] R. G. Forbes. Gas Field Ionisation Sources. In Jon Orloff, editor, *Handbook of Charged Particle Optics*, pages 87–128. CRC Press, 2nd edition, 2009.

[129] F. H. M. Rahman, S. McVey, L. Farkas, J. A. Notte, S. Tan, and R. H. Livengood. The Prospects of a Subnanometer Focused Neon Ion Beam. *Scanning*, 34:129–34, 2012. ISSN 1932-8745. doi: 10.1002/sca.20268.

[130] Y. Zhou, R. O'Connell, P. Maguire, and H. Zhang. High Throughput Secondary Electron Imaging of Organic Residues on a Graphene Surface. *Scientific Reports*, 7032(4):3–8, 2014. doi: 10.1038/srep07032.

[131] J. F. Ziegler, J. P. Biersack, and M. D. Ziegler. *Stopping and Range of Ions in Matter*. Chester, MD: SRIM Co., 5th edition, 2008. ISBN 978-0-9654207-1-6.

[132] J. J. Lopez, F. Greer, and J. R. Greer. Enhanced Resistance of Single-Layer Graphene to Ion Bombardment. *Journal of Applied Physics*, 107:104326, 2010.

[133] A. V. Krasheninnikov and F. Banhart. Engineering of Nanostructured Carbon Materials with Electron or Ion Beams. *Nature Materials*, 6(10):723–733, 2007.

[134] O. Lehtinen, J. Kotakoski, A. V. Krasheninnikov, A. Tolvanen, K. Nordlund, and J. Keinonen. Effects of Ion Bombardment on a Two-Dimensional Target: Atomistic Simulations of Graphene Irradiation. *Physical Review B*, 81(153401): 153401, 2010.

[135] A. McCreary, R. Ghosh, M. Amani, J. Wang, K. A. N. Duerloo, A. Sharma, K. Jarvis, E. J. Reed, A. M. Dongare, S. K. Banerjee, M. Terrones, R. R. Namburu, and M. Dubey. Effects of Uniaxial and Biaxial Strain on Few-Layered Terrace Structures of MoS_2 Grown by Vapor Transport. *ACS Nano*, 10:3186–3197, 2016. ISSN 1936086X. doi: 10.1021/acsnano.5b04550.

[136] S. Zhao, J. Xue, Y. Wang, and S. Yan. Effect of SiO_2 Substrate on the Irradiation-Assisted Manipulation of Supported Graphene: a Molecular Dynamics Study. *Nanotechnology*, 23:285703, 2012. ISSN 0957-4484. doi: 10.1088/0957-4484/23/28/285703.

[137] A. N. Abbas, G. Liu, B. Liu, L. Zhang, H. Liu, D. Ohlberg, W. Wu, and C. Zhou. Patterning, Characterization, and Chemical Sensing Applications of Graphene Nanoribbon Arrays Down to 5 nm Using Helium Ion Beam Lithography. *ACS Nano*, pages 1538–1546, 2014.

[138] V. Iberi, L. Liangbo, A. V. Ievlev, M. G. Stanford, M. W. Lin, X. Li, M. Mahjouri-Samani, S. Jesse, B. G. Sumpter, S. V. Kalinin, D. C. Joy, K. Xiao, A. Belianinov, and O. S. Ovchinnikova. Nanoforging Single Layer $MoSe_2$ Through Defect Engineering with Focused Helium Ion Beams. *Scientific Reports*, 6(30481), 2016. ISSN 2045-2322. doi: 10.1038/srep30481.

[139] A. G. Fedorov, S. Kim, M. Henry, D. Kulkarni, and V. V. Tsukruk. Focused-Electron-Beam-Induced Processing (FEBIP) for Emerging Applications in Carbon Nanoelectronics. *Applied Physics A: Materials Science and Processing*, 117 (4):1659–1674, 2014. ISSN 14320630. doi: 10.1007/s00339-014-8628-4.

[140] C. Thiele, A. Felten, T. J. Echtermeyer, A. C. Ferrari, C. Casiraghi, H. V. Löhneysen, and R. Krupke. Electron-Beam-Induced Direct Etching of Graphene. *Carbon*, 64:84–91, 2013. ISSN 00086223. doi: 10.1016/j.carbon.2013.07.038.

[141] J. A. Gardener and J. A. Golovchenko. Ice-Assisted Electron Beam Lithography of Graphene. *Nanotechnology*, 23(18), 2012. doi: 10.1088/0957-4484/23/18/185302.Ice-assisted.

[142] B. Sommer, J. Sonntag, A. Ganczarczyk, D. Braam, G. Prinz, A. Lorke, and M. Geller. Electron-Beam Induced Nano-Etching of Suspended Graphene. *Scientific Reports*, 5(1):7781, 2015. ISSN 2045-2322. doi: 10.1038/srep07781.

[143] D. S. Fox, A. O'Neill, D. Zhou, M. Boese, J. N. Coleman, and H. Zhang. Nitrogen Assisted Etching of Graphene Layers in a Scanning Electron Microscope. *Applied Physics Letters*, 98(24), 2011. ISSN 00036951. doi: 10.1063/1.3601467.

[144] S. Ross and A. Sussman. Surface Oxidation of Molybdenum Disulfide. *The Journal of Physical Chemistry*, 59(9):889–892, 1955. ISSN 0022-3654. doi: 10.1021/j150531a020.

[145] E. V. Ballou and S. Ross. The Adsorption of Benzene and Water Vapors by Molybdenum Disulfide. *The Journal of Physical Chemistry*, 57(7):653–657, 1953.

[146] A.R. Lansdown. *Molybdenum Disulphide Lubrication.* Elsevier B.V., 1999. ISBN 0-444-50032-4.

[147] H. S. Khare and D. L. Burris. The Effects of Environmental Water and Oxygen on the Temperature-Dependent Friction of Sputtered Molybdenum Disulfide. *Tribology Letters*, 52(3):485–493, 2013. ISSN 10238883. doi: 10.1007/s11249-013-0233-8.

[148] M. Yamamoto, T. L. Einstein, M. S. Fuhrer, and W. G. Cullen. Anisotropic Etching of Atomically Thin MoS_2. *The Journal of Physical Chemistry C*, 117(48):25643–25649, 2013. ISSN 1932-7447. doi: 10.1021/jp410893e.

[149] M. Yamamoto, W. Cullen, T. Einstein, and M. S. Fuhrer. Oxidation of Atomically Thin MoS_2 on SiO_2. In *APS March Meeting Abstracts*, volume 1, page 6004, 2013.

[150] H. Zhou, F. Yu, Y. Liu, X. Zou, C. Cong, C. Qiu, T. Yu, Z. Yan, X. Shen, L. Sun, B. I. Yakobson, and J. M. Tour. Thickness-Dependent Patterning of MoS_2 Sheets with Well-Oriented Triangular Pits by Heating in Air. *Nano Research*, 6(10):703–711, 2013. ISSN 19980124. doi: 10.1007/s12274-013-0346-2.

[151] R. Ionescu, A. George, I. Ruiz, Z. Favors, Z. Mutlu, C. Liu, K. Ahmed, R. Wu, J. S. Jeong, L. Zavala, K. A. Mkhoyan, M. Ozkan, and C. S. Ozkan. Oxygen Etching of Thick MoS_2 Films. *Chemical Communications*, 50(76):11226, 2014. ISSN 1359-7345. doi: 10.1039/C4CC03911D.

[152] J. Hu, S. Wu, Y. Ma, X. Yang, Z. Li, H. Liu, Q. Huo, J. Guan, and Q. Kan. Effect of the Particle Size of MoO_3 on the Catalytic Activity of Mo/ZSM-5 in Methane non-Oxidative Aromatization. *New J. Chem.*, 39(7):5459–5469, 2015. ISSN 1144-0546. doi: 10.1039/C5NJ00672D.

[153] J. Lince and P. Frantz. Anisotropic Oxidation of MoS_2 Crystallites Studied by Angle-Resolved X-ray Photoelectron Spectroscopy. *Tribology Letters*, 9(3-4), 2000. ISSN 16130073. doi: 10.1023/A.

[154] H. Zhu, X. Qin, L. Cheng, A. Azcatl, J. Kim, and R. M. Wallace. Remote Plasma Oxidation and Atomic Layer Etching of MoS_2. *ACS Applied Materials and Interfaces*, 8(29):19119–19126, 2016. ISSN 19448252. doi: 10.1021/acsami.6b04719.

[155] S. K. C., R. C. Longo, R. M. Wallace, and K. Cho. Surface Oxidation Energetics and Kinetics on MoS_2 Monolayer. *Journal of Applied Physics*, 117(13), 2015. ISSN 10897550. doi: 10.1063/1.4916536.

[156] Y. Shi, J. K. Huang, L. Jin, Y. T. Hsu, S. F. Yu, L. J. Li, and H. Y. Yang. Selective Decoration of Au Nanoparticles on Monolayer MoS_2 Single Crystals. *Scientific Reports*, 3:1839, 2013. ISSN 2045-2322. doi: 10.1038/srep01839.

[157] G. P. Neupane, K. P. Dhakal, H. Kim, J. Lee, M. S. Kim, G. Han, Y. H. Lee, and J. Kim. Formation of Nanosized Monolayer MoS_2 by Oxygen-Assisted Thinning of Multilayer MoS_2. *Journal of Applied Physics*, 120(5):1–6, 2016. ISSN 10897550. doi: 10.1063/1.4958939.

[158] R. Rao, A. E. Islam, P. M. Campbell, E. M. Vogel, and B. Maruyama. In Situ Thermal Oxidation Kinetics in Few Layer MoS_2. *2D Materials*, 4, 2017.

[159] T. F. Jaramillo, K. P. Jørgensen, J. Bonde, J. H. Nielsen, S. Horch, and I. Chorkendorff. Identification of Active Edge Sites for Electrochemical H_2 Evolution from MoS_2 Nanocatalysts. *Science (New York, N.Y.)*, 317:100–102, 2007. ISSN 0036-8075. doi: 10.1126/science.1141483.

[160] H. Schweiger, P. Raybaud, G. Kresse, and H. Toulhoat. Shape and Edge Sites Modifications of MoS_2 Catalytic Nanoparticles Induced by Working Conditions: A Theoretical Study. *Journal of Catalysis*, 207:76–87, 2002. ISSN 00219517. doi: 10.1006.

[161] L.Y. Gan, Y. Cheng, U. Schwingenschlögl, Y. Yao, Y. Zhao, X. X. Zhang, and W. Huang. Edge Structures and Properties of Triangular Antidots in Single-Layer MoS_2. *Applied Physics Letters*, 109(091603), 2016. ISSN 00036951. doi: 10.1063/1.4962132.

[162] W. Kiefer, A. P. Mazzolini, and P. R. Stoddart. Recent Advances in Linear and Nonlinear Raman Spectroscopy I. *Journal of Raman Spectroscopy*, 38: 1538–1553, 2007. ISSN 10974555. doi: 10.1002/jrs.

[163] D. Tuschel. Practical Group Theory and Raman Spectroscopy, Part II : Application of Polarization. *Spectroscopy*, 29(3):15–22, 2014. ISSN 08876703.

[164] E. C. Le Ru and E. P. G. Optical Spectroscopy of Molecules. In *Principles of Surface-Enhanced Raman Spectroscopy: and related plasmonic effects*, chapter 2.2 Optica. Elsevier Ltd, Amsterdam, 1st edition, 2009. ISBN 978-0-444-52779-0.

[165] T. W. Judson. *Abstract Algebra Theory and Applications*. 2014. ISBN 0989897540.

[166] M. S. Amer. *Raman Spectroscopy, Fullerenes and Nanotechnology*. Royal Society of Chemistry, 2010.

[167] J. Ribeiro-Soares, R. M. Almeida, E. B. Barros, P. T. Araujo, M. S. Dresselhaus, L. G. Cançado, and A. Jorio. Group Theory Analysis of Phonons in Two-Dimensional Transition Metal Dichalcogenides. *Physical Review B*, 90 (115438):115438, 2014. ISSN 1550235X. doi: 10.1103/PhysRevB.90.115438.

[168] M. O'Brien, N. McEvoy, D. Hanlon, J. N. Coleman, and G. S. Duesberg. Mapping of Low-Frequency Raman Modes in CVD-Grown Transition Metal Dichalcogenides: Layer Number, Stacking Orientation and Resonant Effects. *Scientific Reports*, 6:1–11, 2015. ISSN 20452322. doi: 10.1038/srep19476.

[169] Nanophoton Ltd. Raman-11 User Manual, 2015.

[170] Renishaw Corporation. Automatic Intelligent Background Removal, 2017. URL `http://www.renishaw.com/en/automatic-intelligent-background-removal--25934`.

[171] M. Bradley. Curve Fitting in Raman and IR Spectroscopy: Basic Theory of Line Shapes and Applications. 2007.

[172] M. Wojdyr. Fityk: A General-Purpose Peak Fitting Program. *Journal of Applied Crystallography*, 43:1126–1128, 2010. ISSN 00218898. doi: 10.1107/S0021889810030499.

[173] M. Delhaye and P. Dhamelincourt. Raman Microprobe and Microscope with Laser Excitation. *Journal of Raman Spectroscopy*, 3:33–43, 1975. ISSN 1097-4555. doi: 10.1002/jrs.1250030105.

[174] N. Scheuschner, R. Gillen, M. Staiger, and J. Maultzsch. Interlayer Resonant Raman Modes in Few-Layer MoS_2. *Physical Review B - Condensed Matter and Materials Physics*, 91(235409):235409, 2015. ISSN 1550235X. doi: 10.1103/PhysRevB.91.235409.

[175] Z. Lin, B. R. Carvalho, E. Kahn, R. Lv, R. Rao, H. Terrones, M. A. Pimenta, and M. Terrones. Defect Engineering of Two-Dimensional Transition Metal Dichalcogenides. *2D Materials*, 3(2):022002, 2016. ISSN 2053-1583. doi: 10.1088/2053-1583/3/2/022002.

[176] C. H. Lui, Z. Ye, C. Ji, K. C. Chiu, C. T. Chou, T. I. Andersen, C. Means-Shively, H. Anderson, J. M. Wu, T. Kidd, Y. H. Lee, and R. He. Observation of Interlayer Phonon Modes in van der Waals Heterostructures. *Physical Review B - Condensed Matter and Materials Physics*, 91(16):1–7, 2015. ISSN 1550235X. doi: 10.1103/PhysRevB.91.165403.

[177] Q. J. Song, Q. H. Tan, X. Zhang, J. B. Wu, B. W. Sheng, Y. Wan, X. Q. Wang, L. Dai, and P. H. Tan. Physical Origin of Davydov Splitting and Resonant Raman Spectroscopy of Davydov Components in Multilayer $MoTe_2$. *Physical Review B*, 93(115409):115409, 2016. ISSN 1550235X. doi: 10.1103/PhysRevB.93.115409.

[178] H. R. Gutiérrez, N. Perea-López, A. L. Elías, A. Berkdemir, B. Wang, R. Lv, F. López-Urías, V. H. Crespi, H. Terrones, and M. Terrones. Extraordinary Room-Temperature Photoluminescence in Triangular WS_2 Monolayers. *Nano Letters*, 13(8):3447–3454, 2013. ISSN 15306984. doi: 10.1021/nl3026357.

[179] A. B. Kaul. Two-Dimensional Layered Materials: Structure, Properties, and Prospects for Device Applications. *Journal of Materials Research*, 29(3):348–361, 2014. doi: 10.1557/jmr.2014.6.

[180] Rayleigh. On the Theory of Optical Images, with Special Reference to the Microscope. *Journal of the Royal Microscopical Society*, 23(4):447–473, 1903. ISSN 1365-2818. doi: 10.1111/j.1365-2818.1903.tb04830.x.

[181] Carl Zeiss Ltd. Manual for the SUPRA (VP) and ULTRA Scanning Electron Microscopes, 2005.

[182] R. Reichelt. Science of Microscopy. In P. W. Hawkes and J. C. H. Spence, editors, *Science of Microscopy*, chapter 3, pages 133–272. 1 edition, 2007.

[183] B. J. Griffin, D. C. Joy, and J. R. Michael. Characteristics of Secondary Electron Images from in-Lens and Conventional Everhart-Thornley Detectors - Evidence for the Energy-Based Differentiation of High Resolution SE1 and Delocalized SE2 Signals. *Microscopy and Microanalysis*, 15(Suppl 2):46–47, 2009. ISSN 1431-9276. doi: 10.1017/S14319276090973.

[184] B. C. Carter and D. B. Williams. *Transmission Electron Microscopy: A Textbook for Materials Science.* Springer Ltd., 2007.

[185] Y. Wang, Z. Ni, T. Yu, Z. X. Shen, H. Wang, Y. Wu, W. Chen, A. Thye, and S. Wee. Raman Studies of Monolayer Graphene: The Substrate Effect. *j. Phys. Chem. C*, 112(0001):10637–10640, 2008.

[186] A. D. Smith, F. Niklaus, A. Paussa, S. Vaziri, A. C. Fischer, M. Sterner, F. Forsberg, A. Delin, D. Esseni, P. Palestri, M. Östling, and M. C. Lemme. Electromechanical Piezoresistive Sensing in Suspended Graphene Membranes. *Nano Letters*, 13(7):3237–3242, 2013. ISSN 15306984. doi: 10.1021/nl401352k.

[187] A. O'Neill, U. Khan, and J. N. Coleman. Preparation of High Concentration Dispersions of Exfoliated MoS_2 with Increased Flake Size. *Chemistry of Materials*, 24(12):2414–2421, 2012. ISSN 08974756. doi: 10.1021/cm301515z.

[188] P. Blake, E. W. Hill, A. H. Castro Neto, K. S. Novoselov, D. Jiang, R. Yang, T. J. Booth, and A. K. Geim. Making Graphene Visible. *Applied Physics Letters*, 91(063124):063124, 2007. ISSN 00036951. doi: 10.1063/1.2768624.

[189] Y. Q. Bie, Y. Zhou, Z. Liao, K. Yan, S. Liu, Q. Zhao, S. Kumar, H. C. Wu, G. S. Duesberg, G. L. W. Cross, J. Xu, H. Peng, Z. Liu, and D. Yu. Site-Specific Transfer-Printing of Individual Graphene Microscale Patterns to Arbitrary Surfaces. *Advanced Materials*, 23(34):3938–43, 2011. ISSN 1521-4095. doi: 10.1002/adma.201102122.

[190] ImageJ Homepage. URL `https://imagej.nih.gov/ij/`.

[191] S. Liu, Q. Zhao, J. Xu, K. Yan, H. Peng, F. Yang, L. You, and D. Yu. Fast and Controllable Fabrication of Suspended Graphene Nanopore Devices. *Nan-*

otechnology, 23(8):085301, 2012. ISSN 0957-4484. doi: 10.1088/0957-4484/23/8/085301.

[192] N. Lu, J. Wang, H. C. Floresca, and M. J. Kim. In Situ Studies on the Shrinkage and Expansion of Graphene Nanopores under Electron Beam Irradiation at Temperatures in the Range of 400-1200 °C. *Carbon*, 50(8):2961–2965, 2012. ISSN 00086223. doi: 10.1016/j.carbon.2012.02.078.

[193] L. Yan, Y. B. Zheng, F. Zhao, S. Li, X. Gao, B. Xu, P. S. Weiss, and Y. Zhao. Chemistry and Physics of a Single Atomic Layer: Strategies and Challenges for Functionalization of Graphene and Graphene-Based Materials. *Chem. Soc. Rev.*, 41(1):97–114, 2012. doi: 10.1039/C1CS15193B.

[194] L. Liu, S. Ryu, M. R. Tomasik, E. Stolyarova, N. Jung, M. S. Hybertsen, M. L. Steigerwald, L. E. Brus, and G. W. Flynn. Graphene Oxidation: Thickness-Dependent Etching and Strong Chemical Doping. *Nano Letters*, 8(7):1965–1970, 2008. ISSN 15306984. doi: 10.1021/nl0808684.

[195] M. Wojdyr. Curve Fitting: Nonlinear Optimization, 2016.

[196] O. Lehtinen, J. Kotakoski, A. V. Krasheninnikov, and J. Keinonen. Cutting and Controlled Modification of Graphene with Ion Beams. *Nanotechnology*, 22:175306, 2011. ISSN 0957-4484. doi: 10.1088/0957-4484/22/17/175306.

[197] J. F. Ziegler, M. D. Ziegler, and J. P. Biersack. SRIM-The stopping and range of ions in matter (2010). *Nuclear Instruments and Methods in Physics Research Section B: Beam Interactions with Materials and Atoms*, 268(11):1818–1823, 2010.

[198] J. Buchheim, R. M. Wyss, I. Shorubalko, and H. G. Park. Understanding the Interaction Between Energetic Ions and Freestanding Graphene Towards Practical 2D Perforation. *Nanoscale*, 8:8345–8354, 2016. ISSN 2040-3364. doi: 10.1039/C6NR00154H.

[199] G. Gawlik, P. Ciepielewski, J. Jagielski, and J. Baranowski. Modification of Graphene by Ion Beam. *Nuclear Instruments and Methods in Physics Research,*

Section B: Beam Interactions with Materials and Atoms, 406:683–688, 2017. ISSN 0168583X. doi: 10.1016/j.nimb.2017.04.054.

[200] E. H. Ahlgren, J. Kotakoski, O. Lehtinen, and A. V. Krasheninnikov. Ion Irradiation Tolerance of Graphene as Studied by Atomistic Simulations. *Applied Physics Letters*, 100(233108):233108, 2012. ISSN 00036951. doi: 10.1063/1.4726053.

[201] A. Zandiatashbar, G. H. Lee, S. J. An, S. Lee, N. Mathew, M. Terrones, T. Hayashi, C. R. Picu, J. Hone, and N. Koratkar. Effect of Defects on the Intrinsic Strength and Stiffness of Graphene. *Nature Communications*, 5:3186, 2014. ISSN 2041-1723. doi: 10.1038/ncomms4186.

[202] S. Mathew, T. K. Chan, D. Zhan, K. Gopinadhan, A. R. Barman, M. B. H. Breese, S. Dhar, Z. X. Shen, T. Venkatesan, and J. T. L. Thong. The Effect of Layer Number and Substrate on the Stability of Graphene Under MeV Proton Beam Irradiation. *Carbon*, 49(5):1720–1726, 2011. ISSN 00086223. doi: 10.1016/j.carbon.2010.12.057.

[203] A. Merrill, C. D. Cress, J. E. Rossi, N. D. Cox, and B. J. Landi. Threshold Displacement Energies in Graphene and Single-Walled Carbon Nanotubes. *Physical Review B*, 92(075404):075404, 2015. ISSN 1550235X. doi: 10.1103/PhysRevB.92.075404.

[204] J. C. Meyer, F. Eder, S. Kurasch, V. Skakalova, J. Kotakoski, H. J. Park, S. Roth, A. Chuvilin, S. Eyhusen, G. Benner, A. V. Krasheninnikov, and U. Kaiser. Accurate Measurement of Electron Beam Induced Displacement Cross Sections for Single-Layer Graphene. *Physical Review Letters*, 108(196102):196102, 2012. ISSN 0031-9007. doi: 10.1103/PhysRevLett.108.196102.

[205] A. Dimiev, D. V. Kosynkin, A. Sinitskii, A. Slesarev, Z. Sun, and J. M. Tour. Layer-by-Layer Removal of Graphene for Device Patterning. *Science*, 331(6021):1168–1172, 2011. ISSN 0036-8075. doi: 10.1126/science.1199183.

[206] T. C. Nguyen, M. Otani, and S. Okada. Semiconducting Electronic Property of Graphene Adsorbed on (0001) Surfaces of SiO_2. *Physical Review Letters*, 106 (106801):106801, 2011. ISSN 00319007. doi: 10.1103/PhysRevLett.106.106801.

[207] M. O'Brien, N. McEvoy, T. Hallam, H. Y. Kim, N. C. Berner, D. Hanlon, K. Lee, J. N. Coleman, and G. S. Duesberg. Transition Metal Dichalcogenide Growth via Close Proximity Precursor Supply. *Scientific Reports*, 4:7374, 2014. ISSN 2045-2322. doi: 10.1038/srep07374.

[208] J. P. Hirvonen, J. Koskinen, J. R. Jervis, and M. Nastasi. Present Progress in the Development of Low Friction Coatings. *Surface and Coatings Technology*, 80(1-2):139–150, 1996. ISSN 02578972. doi: 10.1016/0257-8972(95)02701-7.

[209] N. Scheuschner, O. Ochedowski, A. M. Kaulitz, R. Gillen, M. Schleberger, and J. Maultzsch. Photoluminescence of Freestanding Single- and Few-Layer MoS_2. *Physical Review B - Condensed Matter and Materials Physics*, 89(125406): 125406, 2014. ISSN 1550235X. doi: 10.1103/PhysRevB.89.125406.

[210] S. Tongay, J. Suh, C. Ataca, W. Fan, A. Luce, J. S. Kang, J. Liu, C. Ko, R. Raghunathanan, J. Zhou, F. Ogletree, J. Li, J. C. Grossman, and J. Wu. Defects Activated Photoluminescence in Two-Dimensional Semiconductors: Interplay between Bound, Charged, and Free Excitons. *Scientific reports*, 3:2657, 2013. ISSN 2045-2322. doi: 10.1038/srep02657.

[211] P. K. Chow, R. B. Jacobs-Gedrim, J. Gao, T. M. Lu, B. Yu, H. Terrones, and N. Koratkar. Defect-Induced Photoluminescence in Monolayer Semiconducting Transition Metal Dichalcogenides. *ACS Nano*, 9(2):1520–1527, 2015. ISSN 1936-0851. doi: 10.1021/nn5073495.

[212] C. V. Ramana, U. Becker, V. Shutthanandan, and C. M. Julien. Oxidation and Metal-Insertion in Molybdenite Surfaces: Evaluation of Charge-Transfer Mechanisms and Dynamics. *Geochemical Transactions*, 9:8, 2008. ISSN 1467-4866. doi: 10.1186/1467-4866-9-8.

[213] M. Baker, R. Gilmore, C. Lenardi, and W. Gissler. XPS Investigation of Preferential Sputtering of S from MoS_2 and Determination of MoS_x Stoichiometry

from Mo and S Peak Positions. *Applied Surface Science*, 150:255–262, 1999. ISSN 01694332. doi: 10.1016/S0169-4332(99)00253-6.

[214] M. Nastasi, J. W. Mayer, and J. K. Hirvonen. Ion-Solid Simulations and Diffusion. In *Ion-Solid Interactions: Fundamentals and Applications*, pages 209–216. Cambridge University Press, 1st edition, 1996.

[215] M. B. Vellinga, R. de Jonge, and C. Haas. Semiconductor to Metal Transition in $MoTe_2$. *Journal of Solid State Chemistry*, 2(299-302), 1970. ISSN 1095726X. doi: 10.1016/0022-4596(70)90085-X.

[216] I. Nishida. Study of Semiconductor-to-Metal Transition in Mn-Doped $FeSi_2$. *Physical Review B*, 7(6):2710–2713, 1973. ISSN 01631829. doi: 10.1103/PhysRevB.7.2710.

[217] N. Kodama, T. Hasegawa, Y. Okawa, T. Tsuruoka, C. Joachim, and M. Aono. Electronic States of Sulfur Vacancies Formed on a MoS_2 Surface. *Japanese Journal of Applied Physics*, 49(08LB01), 2010. ISSN 00214922. doi: 10.1143/JJAP.49.08LB01.

[218] B. H. Kim, M. Park, M. Lee, S. J. Baek, H. Y. Jeong, M. Choi, S. J. Chang, W. G. Hong, T. K. Kim, H. R. Moon, Y. W. Park, N. Park, and Y. Jun. Effect of Sulphur Vacancy on Geometric and Electronic Structure of MoS_2 Induced by Molecular Hydrogen Treatment at Room Temperature. *RSC Advances*, 3 (40):18424, 2013. ISSN 2046-2069. doi: 10.1039/c3ra42072h.

[219] M. R. Islam, N. Kang, U. Bhanu, H. P. Paudel, M. Erementchouk, L. Tetard, M. N. Leuenberger, and S. I. Khondaker. Tuning the Electrical Property via Defect Engineering of Single Layer MoS_2 by Oxygen Plasma. *Nanoscale*, 6: 10033, 2014. ISSN 2040-3364. doi: 10.1039/C4NR02142H.

[220] T. Y. Kim, K. Cho, W. Park, J. Park, Y. Song, S. Hong, W. K. Hong, and T. Lee. Irradiation Effects of High-Energy Proton Beams on MoS_2 Field Effect Transistors. *ACS Nano*, 8(3):2774–2781, 2014. ISSN 1936086X. doi: 10.1021/nn4064924.

[221] J. N. Coleman, M. Lotya, A. O'Neill, S. D. Bergin, P. J. King, U. Khan, K. Young, A. Gaucher, S. De, R. J. Smith, I. V. Shvets, S. K. Arora, G. Stanton, H. Y. Kim, K. Lee, G. T. Kim, G. S. Duesberg, T. Hallam, J. J. Boland, J. J. Wang, J. F. Donegan, J. C. Grunlan, G. Moriarty, A. Shmeliov, R. J. Nicholls, J. M. Perkins, E. M. Grieveson, K. Theuwissen, D. W. McComb, P. D. Nellist, and V. Nicolosi. Two-Dimensional Nanosheets Produced by Liquid Exfoliation of Layered Materials. *Science*, 331(6017):568–571, 2011. ISSN 0036-8075. doi: 10.1126/science.1194975.

[222] S. Y. Lee, U. J. Kim, J. Chung, H. Nam, H. Y. Jeong, G. H. Han, H. H. Kim, H. M. Oh, H. Lee, H. H. Kim, Y. G. Roh, J. Kim, S. W. Hwang, Y. Park, and Y. H. Lee. Large Work Function Modulation of Monolayer MoS_2 by Ambient Gases. *ACS Nano*, 10(6):6100–6107, 2016. ISSN 1936086X. doi: 10.1021/acsnano.6b01742.

[223] J. M. Bernhard. Work Function Study of Iridium Oxide and Molybdenum Using UPS and Simultaneous Fowler-Norheim I-V Plots with Field Emission Energy Distributions. *University of North Texas, PhD Thesis*, page 140, 1999.

[224] J. Moosburger-Will, J. Kündel, M. Klemm, S. Horn, P. Hofmann, U. Schwingenschlögl, and V. Eyert. Fermi Surface of MoO_2 Studied by Angle-Resolved Photoemission Spectroscopy, de Haas-van Alphen Measurements, and Electronic Structure Calculations. *Physical Review B*, 79(115113):115113, 2009. ISSN 10980121. doi: 10.1103/PhysRevB.79.115113.

[225] Y. Guo and J. Robertson. Origin of the High Work Function and High Conductivity of MoO_3. *Applied Physics Letters*, 105(222110):222110, 2014. ISSN 00036951. doi: 10.1063/1.4903538.

[226] M. Diskus, O. Nilsen, H. Fjellvag, S. Diplas, P. Beato, C. Harvey, E. van Schrojenstein Lantman, and B. M. Weckhuysen. Combination of Characterization Techniques for Atomic Layer Deposition MoO_3 Coatings: From the Amorphous to the Orthorhombic α-MoO_3 Crystalline Phase. *Journal of Vacuum Science & Technology A Vacuum Surfaces and Films*, 30, 2012.

[227] I. E. Wachs and C. A. Roberts. Monitoring Surface Metal Oxide Catalytic Active Sites with Raman Spectroscopy. *Chemical Society Reviews*, 39(12): 5002, 2010. ISSN 0306-0012. doi: 10.1039/c0cs00145g.

[228] L. Yang, L. Liu, Y. Zhu, X. Wang, and Y. Wu. Preparation of Carbon Coated MoO_2 Nanobelts and their High Performance as Anode Materials for Lithium Ion Batteries. *Journal of Materials Chemistry*, 22:13148–13152, 2012. ISSN 0959-9428. doi: 10.1039/c2jm31364b.

[229] B. Lafuente, R. T. Downs, H. Yang, and N. Stone. *The Power of Databases: The RRUFF Project*. 2015. ISBN 9783110417104. doi: 10.1515/9783110417104-003.

[230] S. Kim, M. J. Park, N. P. Balsara, G. Liu, and A. M. Minor. Ultramicroscopy Minimization of Focused Ion Beam Damage in Nanostructured Polymer Thin Films. *Ultramicroscopy*, 111(3):191–199, 2011. ISSN 0304-3991. doi: 10.1016/j.ultramic.2010.11.027.